Imperial College
London

The Imperial College of Science, Technology and Medicine
Department of Physics

Motional Sideband Spectra and Coulomb Crystals in a Penning Trap

Sandeep Mavadia

Submitted in part fulfilment of the requirements for the degree of
Doctor of Philosophy in Physics of Imperial College London,
09/04/2013

Abstract

Laser cooled ions in a Penning trap can be isolated from the environment by placing them in vacuum and only interacting with them through optical and RF fields. The number of trapped particles can be varied from a single ion up to thousands. Confinement is provided by a static homogeneous magnetic field and a quadrupole electric potential. In the natural frame of the ions, this appears as a 3D simple harmonic potential. Therefore three dimensional structures can be formed in the absence of any additional RF field which may lead to heating as is the case with RF traps. There are $3N$ different motional modes for N particles. I present an analysis of the motion of a single particle showing that the energy levels for all three modes are equally spaced. I also describe the interaction between a trapped two level atom and an optical field.

During my time in the lab the laser and computer control of the experiment has been significantly improved. In addition, an existing trap was modified to provide greater optical access and fluorescence collection. This allowed the vibrational levels superimposed on the internal states of a single $^{40}\mathrm{Ca}^+$ ion to be resolved via a narrow linewidth, electric quadrupole transition. This is the first observation of magnetron and modified cyclotron sidebands on an optical transition.

When more than one calcium ion is laser cooled, and their temperature reduced below 5 mK, they form a Coulomb crystal. The locations of the ions minimise the total potential energy which is comprised of the Coulomb repulsion and trap potential. The fluorescence collection optics have been arranged to resolve individual ions in these crystals. Information about the motion of the ions is deduced by comparing photos from the experiment to numerical simulations. Previously, only two ions have ever been aligned along the magnetic field in a Penning trap. I present strings of up to 29 particles and suggest the only limitation, apart from the electrode structure, is the overlap of the laser beams with the ions.

Acknowledgements

Thanks goes to all the people I have worked with during my time in the Lab: Dan, Sean, Shailen, Graham and Joe without whom none of the work presented here would have been possible. Special thanks to Dan, not just for his talents useful across the whole lab and incredible ability to just make things work but also for his enthusiasm and drive to try new ideas. Thanks especially to Sean for his companionship during the time when we were in both working in the lab.

Thanks also goes to my supervisors. Richard for always making time for me and explaining theory when I invariably became stuck. And to Danny for a constant supply of optimism when I had occasionally run out.

I gratefully thank Brian for his work in the mechanical workshop; for those jobs where absolute precision was required. And also Bandu whose technical knowledge seemed endless.

A thank you to everyone in the CCM for the good friendship for the past few years, it was great to feel part of a larger group.

Declaration

I declare that this thesis is my own work. Where I have used the work of others the sources are appropriately referenced and acknowledged.

Contents

1 **Introduction** **8**

1.1 Description of thesis 10

2 **Ion Traps** **12**

2.1 Penning Traps 13

2.1.1 Classical Motion 13

2.1.2 Quantum motion 19

3 **Ion-Light Interaction** **21**

3.1 Interaction with internal states 22

3.1.1 Geometry 28

3.1.2 Radiation emission patterns 29

3.1.3 Polarisation coefficients 31

3.1.4 Optimum Polarisation 31

3.2 Interaction with external states 32

3.3 Broadening Mechanisms 37

3.3.1 Doppler Broadening 37

3.3.2 Laser linewidth 38

3.4 Laser cooling 38

3.4.1 Doppler Cooling 39

3.4.2 Resolved sideband cooling 47

4 Experimental Setup **52**

4.1 Calcium II level structure 52

4.1.1 J quantum number magnetic mixing 52

4.2 Diode Lasers 54

4.3 Laser Locking 55

4.3.1 Pound-Drever-Hall lock theory 56

4.3.2 Dither lock 59

4.3.3 Doppler cooling lasers dither lock 60

4.3.4 Doppler cooling lasers transfer cavity lock 61

4.4 Repumping lasers 64

4.4.1 Multiple transition repumping 64

4.4.2 Repumping lasers transfer cavity lock 66

4.5 Stabilised 729 nm Laser 67

4.5.1 ULE high finesse cavity 68

4.5.2 Laser & Locking electronics 69

4.6 Optical setup 73

4.7 Trap configuration 75

4.8 Loading Ions 79

4.9 FPGA and computer control 80

4.9.1 Computer front-end 82

4.9.2 FPGA memory interface 82

4.9.3 Mains Trigger 85

4.9.4 RF electronics 85

5 Coulomb Crystals **87**

5.1 Centre of Mass Oscillations 90

5.2 Magnetron mode instability 90

5.3 Motion in a Rotating Frame 92

5.3.1 Laser beam torque 93

5.4 Linear Ion Chains 94

5.5 Higher dimensional Coulomb crystals 95

5.6 Larger Crystals 101

5.6.1 Effect of quantum J-state mixing in Coulomb crystals 102

6 Motional Sideband Spectroscopy 105

6.1 Pulse sequence 106

6.1.1 Mains triggering 107

6.1.2 Doppler Cooling 108

6.1.3 State preparation 108

6.1.4 729 nm pulse 109

6.1.5 State detection 109

6.2 Magnetic field components of the 729 nm transition 112

6.3 Cavity Drift 113

6.4 Axial Spectrum 115

6.5 Radial spectrum 122

7 Discussion 127

A Clebsch-Gordon Coefficients 130

B Polarisation Coefficients 134

B.1 Dipole transitions 135

B.2 Quadrupole transitions 137

Bibliography 141

Chapter 1

Introduction

Charged particles are easily trapped using either a high-frequency oscillating electrical potential (RF trap) or an homogeneous magnetic field and a static quadratic electric potential (Penning trap). If these particles are confined in vacuum, they can be stored for many hours, even months in some cases.

In atomic physics, usually singly charged ions are used for experiments. A few elements in this state have a simple enough valence electron energy level structure to allow closed cycle interactions with lasers and RF fields. These species can be laser cooled to a temperature which is not possible by any other means. When the temperature of the ions is reduced sufficiently, quantum mechanics must be used to describe the motion of the ions rather than classical mechanics. Using lasers it is possible to engineer and exploit quantum entanglement between the internal electronic state of the valence electron and motional state of the ion.

At low temperatures the particles form stable structures. They find equilibrium positions where the potential energy associated with the Coulomb repulsion from all the other trapped particles and the confining potential is minimised. The ratio of the Coulomb repulsion between these particles to their thermal energy can be made high enough so that the ions occupy fixed equilibrium positions forming so called Coulomb crystal. Plasma physics and astro-physics researchers also use this idea. They use charged dust or micro-particles to study conditions that are expected to exist in outer space. Their particles are much heavier than individual ions and the oscillation frequencies are in a regime where they need only consider classical physics.

Ion traps are used for many different purposes; one of the most common is for high resolution measurements in frequency metrology and mass spectrometry. In these types of experiments it is often beneficial to isolate the particles from the background. By reducing the number of trapped particles, collisional effects which might obscure the results are decreased. In fact, individual ions are routinely trapped for mass spectroscopy or optical frequency standard measurements. To achieve the highest precision in these experiments, the motion of the ions is reduced so that they occupy only a small volume. Where laser cooling is available, this can even be the quantum mechanical harmonic oscillator ground state. The techniques initially designed for this field have been adapted for use in quantum information processing since the initial proposal by Cirac and Zoller in 1995 [1]. Much progress has been made in this field. For example, a string of ions can be cooled to the ground state of motion and entangled [2] or used in quantum gates [3]. However, in many groups it has been accepted that any trapped ion system designed to perform quantum algorithms will need to have the ability to move ions around and be adaptable to different operations. A list of the key requirements are laid out in the DiVincenzo criteria [4].

In 1982, Richard Feynman suggested designing one quantum system to simulate another quantum system [5]. He showed that a classical computer would find it exponentially more difficult to calculate the state of a quantum system as the number of particles increased. More recently, there has been interest in using arrays of trapped ions to simulate other quantum systems which are harder to access and control [6, 7].

Only a single ion, or linear strings of ions, can be cooled to the quantum ground state across all the motional modes in an RF trap; away from the RF null ions are susceptible to RF heating. Penning traps do not suffer from this limitation, and more interesting two and three dimensional structures could, potentially, be cooled to the ground state. Proposals where a large number of particles need to be coupled together or where the experiment requires a two or three dimensional potential surface are more suited to Penning traps. However, there are technical challenges which make some aspects of performing experiments in Penning traps less attractive than using an RF trap. Also, the benefits outlined above are only useful in certain circumstances. Therefore, until very recently, there were only two research groups[1] working on laser cooled ions in Penning traps compared to tens of groups using RF traps. A lot of the work described in this thesis will show that in principle, much of the work performed in one dimension in a RF trap is feasible in two or three dimensions in a Penning trap.

I will show that we can form and manipulate Coulomb crystals in a Penning trap. The work in this thesis will also demonstrate the first steps towards ground state cooling these ions. Specifically, we observe motional sidebands on an optical transition. These are worthwhile aims in themselves merely because they have not been demonstrated previously. However, after these goals have been achieved, experiments that require controlled coherent interactions between larger numbers of particles than is possible in a RF trap may also be

---

[1] The *other* group is headed by John Bollinger and is based at NIST in Boulder, Colorado.

performed.

1.1 Description of thesis

The motion of an ion in a Penning trap can be calculated without any approximations. In chapter 2, the equations of motion are solved and show that the trap potential is simply a three-dimensional harmonic oscillator. By forming the appropriate ladder operators, these oscillators can be quantised in the standard way. These energy levels are superimposed on to the internal states of the ion.

A single ion with the appropriate atomic energy level structure can be approximated as a two level system. The interactions between light and a free two level atom and also between light and a trapped ion are analysed in chapter 3. The dependence of the relevant matrix element on geometric factors i.e. angle of incidence and polarisation relative to the quantisation axis are thoroughly explained. This information is useful to see which transitions are can be stimulated with our limited optical access.

Doppler laser cooling in a Penning trap is more complicated than in an RF trap because the potential energy in the plane perpendicular to magnetic field decreases as the magnitude of the orbit increases. Here, simply using a laser beam detuned to a lower frequency than the atomic resonance would lead to unstable motion. Instead, in chapter 3, a method for reducing the amplitude of motion for all three modes using a laser beam intensity gradient is described.

The vast majority of the time during my degree has been spent building, and improving, the equipment used to trap and laser cool $^{40}\text{Ca}^+$ ions to Coulomb crystals of tens or hundreds of ions. A concise description of the apparatus is given in chapter 4. This includes the laser locking techniques, and the optical layout. Daniel Crick, Sean Donnellan and I designed a method for economically repumping eight magnetic field split metastable levels which remove $^{40}\text{Ca}^+$ ions from the cooling cycle; the details of this are also included. During my time in the lab we also implemented several improvements to the general apparatus including a computerised control system and optical modulators for repetitive high speed pulsed spectroscopy; an optical fibre connection to a reliable wavemeter in an adjacent lab; a photoionisation loading scheme using a high power, pulsed, frequency doubled, Nd:YAG laser and a method for atomic species and isotope purification inside the trap. In addition, I modified a trap originally built by Shailen Bharadia to allow greater optical access. The imaging system and opto-mechanics around the trap were entirely replaced, this produced a completely fibre coupled trap which could be wheeled around while still observing atomic fluorescence when operated as a RF trap. One key aspect of the experiment, built exclusively by Daniel Crick, was a narrow linewidth diode laser. Nonetheless, I have described its operation and provide an overview of its locking system. This laser was essential to perform the spectroscopy described in chapter 6.

When the temperature of ions is reduced below 5 mK they form well ordered Coulomb crystals. In chapter 5 the shapes of these crystals are analysed to determine information about the trap parameters, including the frequency of rotation. By comparing a photo of a string of ions to their theoretically predicted position, it can also be shown that the trapping potential is well approximated by a quadratic function over at least several hundred micrometres. Photos show that single ions in Coulomb crystals are clearly resolved. Even for large crystals, where the number of ions cannot be directly counted, which is otherwise done by aligning them in a string along the magnetic field; we can still extract information about the ratio of the trap frequencies and the number of ions by comparison to a computer simulation. This shows significant progress compared to previous experiments. Coulomb crystals in a Penning trap have previously been formed of thousands or hundreds of ions in two or three dimensional structures [8] with the exception of a single experiment where a two ion crystal was imaged [9]. The results in this thesis fill the middle ground; with the observation of Coulomb crystals from a few ions up to several hundred ions.

In chapter 6, the pulse sequence used to stimulate and measure the shelving probability of a single ion via a narrow linewidth quadrupole transition is described. At the end of this chapter I show preliminary data of sideband spectroscopy of the vibrational modes of a single ion. Finally, I discuss the results presented in this this thesis and give a brief outlook for the future.

Chapter 2

Ion Traps

Ion traps can be used to almost perfectly isolate charged particles from the environment while still allowing controlled external interactions via narrowband laser light or microwaves. Ideally we can produce an harmonic trapping potential for the ions. The two common methods, described briefly below, both have the same ideal electrode geometry, as shown in figure 2.1. These electrodes should be formed of hyperboloids of revolution where **z** is the symmetry axis denoted as the axial direction in this thesis. The other two dimensions are degenerate and henceforth collectively described as the radial direction.

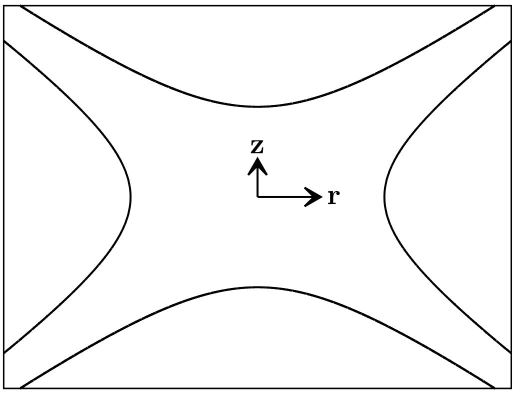

Figure 2.1: Cross section of the ideally shaped trap electrodes. The axes in the **z** and **r** directions have equal scaling. The electrodes are formed of hyperboloids of revolution. The electrodes on the top and bottom of the figure are called endcaps and the single electrode in the centre of the figure is normally called the ring.

There are two commonly used methods for trapping.

1. RF Trap - by quickly alternating the polarity of the electric field applied to electrodes

a time averaged harmonic potential can be created in the centre of the trap where an RF null is formed. In a variation of this type of trap, called a linear RF trap, the RF null is extended to a 1D line.

2. Penning Trap - a homogeneous magnetic field is imposed along the trap axis producing a cyclotron orbit in the plane perpendicular to the field. The ion is trapped along the trap axis using a static quadrupole electric potential generated by applying a DC potential to the electrodes.

In this thesis I shall only describe experiments in a Penning trap. There are many good references for information on RF traps including from one of the inventors, Wolfgang Paul [10].

2.1 Penning Traps

2.1.1 Classical Motion

In a Penning trap the confinement in the radial plane is provided by a homogeneous magnetic field. In this plane the particle travels in cyclotron loops. To provide trapping in the remaining, axial, dimension a DC harmonic potential is imposed. However, to satisfy Laplace's equation the electric field produces an anti-trapping potential in the radial plane which partially counteracts the confinement from the magnetic field. This makes the effective radial potential from the magnetic field shallower and reduces the cyclotron frequency, to what is now called the modified cyclotron frequency. Secondly, the combination of these two fields leads to a third mode, called the magnetron mode, arising from the $\mathbf{E} \times \mathbf{B}$ drift. This should be obvious when considering that crossed electric and magnetic fields are often used as velocity filters for charged particles.

The physical effect of this force can be seen by first considering the motion of a charged particle in a constant electric field perpendicular to a constant magnetic field. Figure 2.2 shows that there is a differential velocity for a particle on one side of the orbit relative to the other side leading to a drift in the $\mathbf{E} \times \mathbf{B}$ direction. Extending this to a radial electric field, shown in figure 2.3, the $\mathbf{E} \times \mathbf{B}$ drift precesses around the magnetic field in the same direction as the cyclotron motion.

The explanation of the motion of an ion in this section is based on the description given in [11] and [12]. It is easier when solving a problem dependent on magnetic and electrostatic fields to consider a generalised potential including both a scalar potential, ϕ and vector potential, $\boldsymbol{A}$. The potential of a constant magnetic field, $\mathbf{B} = \mathrm{B}\boldsymbol{z}$, can be written as $\phi = 0$, $\boldsymbol{A} = (\mathbf{B} \times \boldsymbol{r})/2 = (-yB, xB, 0)/2$ and an electrostatic potential as $\phi = \phi$, $\boldsymbol{A} = 0$.

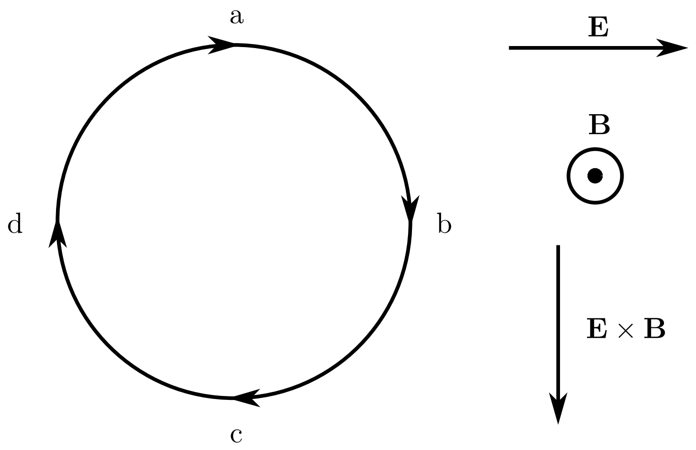

Figure 2.2: A positively charged particle travels in cyclotron loops in a magnetic field. When a perpendicular uniform electric field is added, the particle has a higher speed at point b rather than point d. The net effect is a drift in the $\mathbf{E} \times \mathbf{B}$ direction. In this case the cyclotron motion no longer from closed loops.

In a Penning trap $\phi = \left(k/4\right) \times \left(2z^2 - x^2 - y^2\right)$, where k is a constant dependent on the applied potential and the electrode geometry. In an ideal Penning trap the electrodes are made up of hyperboloids of revolution as shown in figure 2.1, which follow the equations

$$\frac{r^2}{r_0^2} - \frac{z^2}{z_0^2} = \pm 1. \tag{2.1}$$

In equation 2.1 the positive sign relates to the central ring electrode and the negative sign to the two endcaps; r_0 and z_0 are the closest approaches of the electrodes to the centre of the trap in the radial and axial dimensions respectively. In this case $k = 4U/\left(2z_0^2 + r_0^2\right)$ where U is the applied potential. To trap positively charged ions, the potential applied to the endcaps should be positive relative to the ring voltage.

The generalised electromagnetic potential $V = q\left(\phi - \dot{\boldsymbol{r}} \cdot \boldsymbol{A}\right)$, written in Cartesian coordinates, is

$$V = \frac{1}{4}qk\left(2z^2 - x^2 - y^2\right) - \frac{q}{2}B\left(\dot{y}x - \dot{x}y\right). \tag{2.2}$$

Writing down the Lagrangian for this system

$$L = \frac{m}{2}\left(\dot{x}^2 + \dot{y}^2 + \dot{z}^2\right) - \frac{1}{4}qk\left(2z^2 - x^2 - y^2\right) + \frac{q}{2}B\left(\dot{y}x - \dot{x}y\right), \tag{2.3}$$

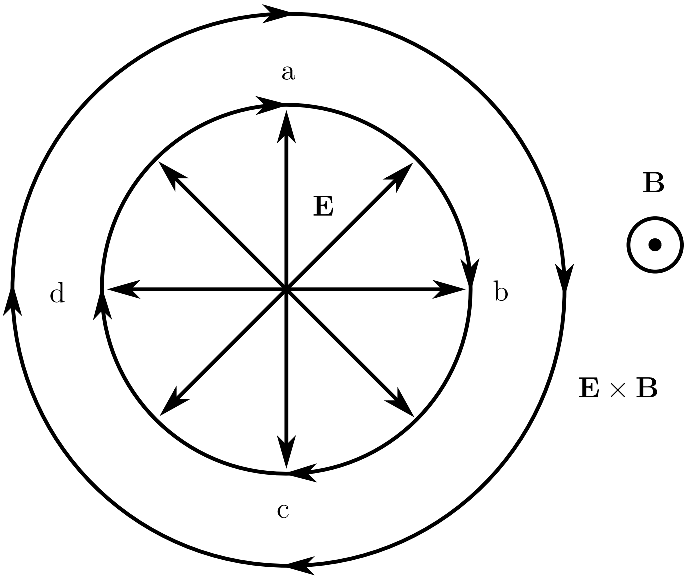

Figure 2.3: Electric field points out from the centre of the trap which leads to an **E** × **B** drift which rotates around the magnetic field in the same direction as the cyclotron motion.

and solving Lagrange's equations we find that

$$m\ddot{x} = \frac{1}{2}qkx + qB\dot{y}, \tag{2.4a}$$

$$m\ddot{y} = \frac{1}{2}qky - qB\dot{x}, \tag{2.4b}$$

$$m\ddot{z} = -qkz. \tag{2.4c}$$

The motion in the z-direction is obviously just simple harmonic motion. Solving this in the standard way the motion can be described by

$$z\left(t\right) = Z\cos\left(\omega_z t + \delta_z\right), \tag{2.5}$$

where the axial frequency is

$$\omega_z = \sqrt{qk/m}. \tag{2.6}$$

The phase, δ_z, and amplitude of the oscillation, Z, depend on the initial conditions.

Solving the radial motion is made easier by substituting the complex variable $s = x + \imath y$ into the two coupled equations for x and y, and reducing them to the single equation

$$\ddot{s} = \frac{qk}{2m}s - \imath\frac{qB}{m}\dot{s}. \tag{2.7}$$

Equation 2.7 has two solutions with frequencies,

$$\omega_\pm = \frac{1}{2}\left[\frac{qB}{m} \pm \sqrt{\left(\frac{qB}{m}\right)^2 - 2\frac{qk}{m}}\right], \tag{2.8}$$

which can be found by substituting the trial solution $s = e^{-\imath\omega t}$. Defining the cyclotron frequency

$$\omega_c = \frac{qB}{m}, \tag{2.9}$$

the oscillation frequency without the imposition of an external electric field, and using the axial frequency from equation 2.6 we can write equation 2.8 more succinctly as

$$\omega_\pm = \frac{1}{2}\left(\omega_c \pm \sqrt{\omega_c^2 - 2\omega_z^2}\right). \tag{2.10}$$

These frequencies are the modified cyclotron frequency, ω_+, and the magnetron frequency, ω_-. We can also define the frequency

$$\omega_1 = \sqrt{\omega_c^2 - 2\omega_z^2}/2, \tag{2.11}$$

which will be useful in subsequent chapters of this thesis. In normal operation $\omega_c \approx \omega_+ \gg \omega_z \gg \omega_-$.

The discriminant in equation 2.8 must remain positive so that the oscillation frequencies are real. This is the condition for stable trapping. In anharmonic traps where the frequency of motion is not constant with distance from the trap centre the entire volume which the ion samples must obey this criterion rather than just the trap centre. This is especially difficult for planar Penning traps which are anharmonic in the extreme, see reference [13] for a discussion on maximising trap depth in such situations.

Having calculated the oscillation frequencies in the radial plane we can write down the general solution to equation 2.7

$$s = R_+ e^{-\imath(\omega_+ t + \delta_+)} + R_- e^{-\imath(\omega_- t + \delta_-)} \tag{2.12}$$

where the radii of the modified cyclotron and magnetron motions, R_+ and R_-, and the phases, δ_+ and δ_-, of the two motions depend on the initial conditions.

Converting this complex co-ordinate back to a Cartesian system we find

$$x = R_+ \cos\left(-\omega_+ t + \delta_+\right) + R_- \cos\left(-\omega_- t + \delta_-\right) \tag{2.13a}$$

$$y = R_+ \sin\left(-\omega_+ t + \delta_+\right) + R_- \sin\left(-\omega_- t + \delta_-\right). \tag{2.13b}$$

Figure 2.4 shows an example of the motion of a single ion in a Penning trap by plotting equations 2.5 and 2.13. Squaring and adding these equations gives the amplitude of the motion in the radial plane.

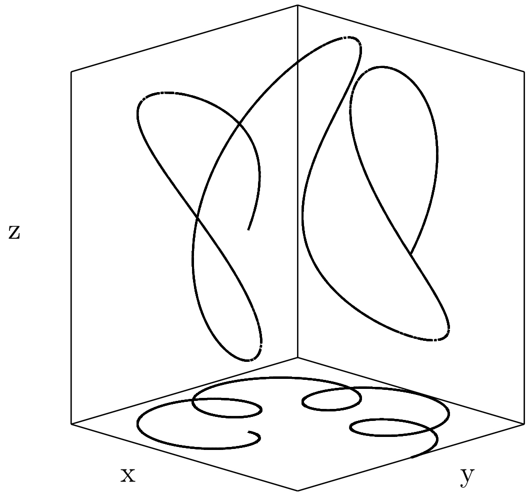

Figure 2.4: Example of the motion of a single ion in a Penning trap ($\omega_z = \omega_c/2$). Motion in three dimensions is above a projection of the radial motion. The amplitudes and initial phases of the three modes are chosen arbitrarily for clarity ($Z = 2R_-$, $R_- = 2R_+$, $\delta_z = \delta_- = \delta_+ = 0$).

$$r^2 = x^2 + y^2 = R_+^2 + R_-^2 + 2R_+R_- \cos\left[\left(\omega_- - \omega_+\right)t + \left(\delta_- - \delta_+\right)\right], \tag{2.14}$$

hence $|R_+ - R_-| < r < |R_+ + R_-|$. We can also separate the total kinetic and potential energy so that

$$\begin{aligned} E_{\text{Kin}} =& \frac{mv^2}{2} = \frac{m}{2}\Big[R_-^2\omega_-^2 + R_+^2\omega_+^2 \\ & +2R_-R_+\omega_-\omega_+\cos\left(\omega_-t - \omega_+t + \delta_- - \delta_+\right) + Z^2\omega_z^2\sin^2\left(\omega_z t + \delta_a\right)\Big], \qquad (2.15\text{a}) \\ E_{\text{Pot}} =& qV = \frac{m\omega_z^2}{2}\Big[-\left(R_-^2 + R_+^2\right)/2 - R_-R_+\cos\left(\omega_-t - \omega_+t + \delta_- + \delta_+\right) \\ & +Z^2\cos^2\left(\omega_z t + \delta_z\right)\Big], \qquad (2.15\text{b}) \end{aligned}$$

noting that $\omega_z^2 = 2\omega_+\omega_-$, and summing these two terms we can find the total energy,

$$E_{\text{Tot}} = E_{\text{Kin}} + E_{\text{Pot}} = \frac{m}{2}\left[Z^2\omega_z^2 + \left(\omega_+ - \omega_-\right)\left(\omega_+R_+^2 - \omega_-R_-^2\right)\right]. \tag{2.16}$$

In chapter 6 it will be shown that by probing the motion using narrow linewidth spectroscopy we can directly measure the time averaged kinetic energy of the particle, given by

$$\left\langle E_{\mathrm{Kin},z}\right\rangle = mZ^2\omega_z^2/4, \tag{2.17a}$$

$$\left\langle E_{\mathrm{Kin},+}\right\rangle = mR_-^2\omega_-^2/2, \tag{2.17b}$$

$$\left\langle E_{\mathrm{Kin},-}\right\rangle = mR_+^2\omega_+^2/2. \tag{2.17c}$$

The motion in the axial direction is oscillatory whereas the modified cyclotron and magnetron motions are orbits with fixed amplitudes. Therefore the average kinetic energy in the axial direction is half of its maximum value whereas the kinetic energy in the radial modes is constant.

To separate the total energy associated with each mode of motion it is necessary to solve the Hamiltonian for a charged particle in an electromagnetic field,

$$H\left(\boldsymbol{r},\boldsymbol{p},t\right) = \frac{\left(\boldsymbol{p}-q\boldsymbol{A}\right)^2}{2m} + q\phi\left(\boldsymbol{r},t\right) \tag{2.18}$$

$$= \frac{\boldsymbol{p}^2}{2m} - \frac{\omega_c}{2}\left(p_y x - p_x y\right) + \frac{m}{8}\left(x^2+y^2\right)\omega_1^2 + \frac{m}{2}z^2\omega_z^2. \tag{2.19}$$

The Hamiltonian includes coupled terms in the radial plane because Cartesian coordinates are not natural to the system. To decouple equation 2.19 we can make the canonical transformation

$$q_\pm = \frac{1}{\sqrt{2}}\left(Cx \mp \frac{p_y}{C}\right), \tag{2.20a}$$

$$p_\pm = \frac{1}{\sqrt{2}}\left(\pm Cy + \frac{p_x}{C}\right), \tag{2.20b}$$

where $C = \sqrt{m\omega_1/2}$. The axial motion is already decoupled from the motion in the radial plane but to keep its form similar to that in equations 2.20 we can scale the axial coordinates with the parameters

$$q_z = z\sqrt{m\omega_z} \tag{2.21a}$$

$$p_z = \frac{p_z'}{\sqrt{m\omega_z}}. \tag{2.21b}$$

Substituting these transformations into equation 2.19 leads to an uncoupled Hamiltonian

$$2H = \omega_+\left(q_+^2+p_+^2\right) - \omega_-\left(q_-^2+p_-^2\right) + \omega_z\left(q_z^2+p_z^2\right). \tag{2.22}$$

The negative sign before the second term shows that the magnetron motion is unstable. However, the frequency associated with the magnetron motion is low enough that the decay period, via synchrotron radiation, is theoretically in the order of years [14].

2.1.2 Quantum motion

The Hamiltonian in equation 2.22 has the form of three harmonic oscillators where the variables q_i & p_i, $(i = +, -, z)$, are now variables for which we can construct standard quantum mechanical raising and lowering ladder operators. Our Hamiltonian in equation 2.22 has already been simplified by removing mass and other constants. The arguments in this section are similar to those given in reference [11]. Using the commutation relation $[q_i, p_i] = \imath\hbar$, the appropriate ladder operators can be written as

$$\hat{a}_i = \frac{\hat{q}_i}{\sqrt{2\hbar}} + \frac{\imath\hat{p}_i}{\sqrt{2\hbar}}, \tag{2.23a}$$

$$\hat{a}_i^\dagger = \frac{\hat{q}_i}{\sqrt{2\hbar}} - \frac{\imath\hat{p}_i}{\sqrt{2\hbar}} \tag{2.23b}$$

where $\hat{a}_i$ and $\hat{a}_i^\dagger$ are the standard lowering and raising operators for an harmonic oscillator. Now we can write the Hamiltonian using just ladder operators instead of conjugate position and momentum operators,

$$\hat{H} = \hbar\omega_+ \left(\hat{a}_+^\dagger \hat{a}_+ + \frac{1}{2}\right) - \hbar\omega_- \left(\hat{a}_-^\dagger \hat{a}_- + \frac{1}{2}\right) + \hbar\omega_z \left(\hat{a}_z^\dagger \hat{a}_z + \frac{1}{2}\right). \tag{2.24}$$

This is analogous to the classical case in equation 2.22 with the quantum corrections for zero point energy and discretised energy levels. If we label energy eigenstates with the notation $|n_+, n_-, n_z\rangle$ for the three different motions, Schrödinger's equation can be written as

$$\hat{H} |n_+, n_-, n_z\rangle = (E_+ - E_- + E_z) |n_+, n_-, n_z\rangle, \tag{2.25}$$

where $E_i = \big(n_i + 1/2\big)\hbar\omega_i$. The raising and lowering operators can also be used to transform the eigenstates as well as calculate the energy of the system. For example, applying them to the axial motion would have the effect

$$\hat{a}_z |n_+, n_-, n_z\rangle = \sqrt{n_z}\, |n_+, n_-, n_z - 1\rangle, \tag{2.26a}$$

$$\hat{a}_z^\dagger |n_+, n_-, n_z\rangle = \sqrt{n_z + 1}\, |n_+, n_-, n_z + 1\rangle, \tag{2.26b}$$

with the caveat that there is no lower state than $|0, 0, 0\rangle$. The ground state wavefunction in Cartesian co-ordinates is

$$|0, 0, 0\rangle = \frac{\exp\left[-\dfrac{z^2}{2Z_0^2} - \dfrac{x^2 + y^2}{2R_0^2}\right]}{R_0\sqrt{Z_0}\,\left(2\pi^3\right)^{1/4}}, \tag{2.27}$$

where $Z_0 = \sqrt{\hbar/(2m\omega_z)}$ and $R_0 = \sqrt{2\hbar/[m(\omega_+ - \omega_-)]}$ [15]. Operating on the states with the raising and lowering operators increases and lowers the energy eigenstate by $\hbar\omega_i$ for the different modes of motion e.g.

$$\hat{H}\hat{a}_z \left|n_+, n_-, n_z\right\rangle = \left(E_+ - E_- + E_z - \hbar\omega_z\right)\sqrt{n_z}\left|n_+, n_-, n_z - 1\right\rangle . \tag{2.28}$$

By comparing, equations 2.16 and 2.24 we can find a simple relation between quantum occupation numbers and classical amplitudes of motion

$$\frac{1}{4}\left(\frac{Z}{Z_0}\right)^2 \approx \left(n_z + \frac{1}{2}\right), \tag{2.29a}$$

$$\left(\frac{R_-}{R_0}\right)^2 \approx \left(n_- + \frac{1}{2}\right), \tag{2.29b}$$

$$\left(\frac{R_+}{R_0}\right)^2 \approx \left(n_+ + \frac{1}{2}\right). \tag{2.29c}$$

Figure 2.5 shows the energy levels of a trapped particle in a Penning trap including the ladder of states imposed by motion. The energy levels discussed so far are only those imposed by motion in the trap. These are convolved with all the internal electronic states of the particle.

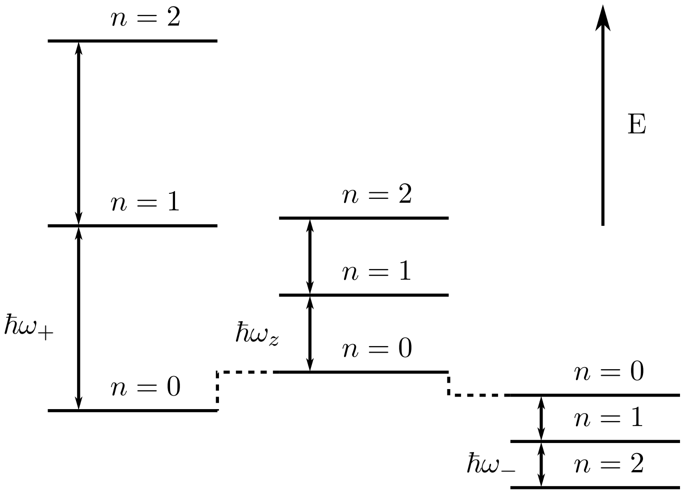

Figure 2.5: Energy level diagram showing the relative energy spacing of the different modes of motion for a single ion (not to scale).

Chapter 3

Ion-Light Interaction

The Hamiltonian for the ion-light interaction is different depending on which type of transition is being stimulated e.g. electric dipole, magnetic quadrupole, etc. Here I will only describe the interaction for electric dipole and electric quadrupole transitions for $^{40}\mathrm{Ca}^{+}$ ions.

The majority of theoretical implementations of trapped ion quantum gates work via coupling the motional states of an ion to their internal levels. In these approaches, the ion usually must start off in a well known quantum state. This is normally done by first laser cooling with a high bandwidth transition, conventionally an electric dipole transition with a scattering rate of the order of 10 MHz. After this, a second stage of cooling can be undertaken where individual quanta of energy can be removed from the trapped particle by selectively stimulating transitions between motional states. This requires a transition which has a scattering rate less than the motional frequency. Normally an electric quadrupole [16] or an off-resonant Raman two-photon process [17] is used for this step. See section 3.4 for more details.

It is advantageous to use long-lived states to store quantum information as spontaneous decay destroys any coherent operation that may have been performed. However, while using a narrower linewidth transition may be better from the point of view of decoherence, maintaining phase lock between an atom and a laser for more than 1 sec is very difficult. Individual ion addressing is also a very powerful tool which has been shown to change the state of a single ion, in a group of ions cooled to a stable linear configuration. This requires a highly focusable source which is possible with optical wavelengths [18] or near field microwaves [19]. Alternatively, a magnetic field gradient can be applied to a Coulomb crystal to allow single ion addressing without a focused electromagnetic field [20].

In this chapter the interaction between light and an atom in the low intensity regime and then a method for cooling an ion in a Penning trap to the ground state of motion is described.

3.1 Interaction with internal states

Atoms have multi-level electronic structures which complicates their spectra. In this section only two electronic levels are considered labelled by j the total angular momentum quantum number and m the magnetic angular momentum quantum number, $|1\rangle = |jm\rangle$ and $|2\rangle = |j'm'\rangle$. The derivation given in the first part of this section is based on references [21–23].

Using Schrödinger's equation

$$\imath\hbar\frac{\partial\Psi}{\partial t} = \left(H_0 + H_{\mathrm{I}}\right)\Psi, \tag{3.1}$$

where H_0 is the atomic part of the Hamiltonian and H_{I} is the interaction with the light field, the evolution of the population in different states coupled by the electromagnetic field can be calculated. The wavefunction can be written as a superposition of the two different eigenstates

$$\Psi = c_1\Psi_1 + c_2\Psi_2 \tag{3.2}$$

where c_1 & c_2 are time dependent coefficients. By substituting equation 3.2 into equation 3.1 and cancelling the part due to the atomic Hamiltonian on both sides we are left with

$$H_{\mathrm{I}}\left(c_1\Psi_1 + c_2\Psi_2\right) = \imath\hbar\left(\Psi_1\frac{\partial c_1}{\partial t} + \Psi_2\frac{\partial c_2}{\partial t}\right). \tag{3.3}$$

Each wavefunction has a time dependence, $\Psi_1 = \psi_1 e^{-\imath E_1 t/\hbar}$ and $\Psi_2 = \psi_2 e^{-\imath E_2 t/\hbar}$, where E_1 and E_2 are the energies of states ψ_1 and ψ_2 relative to the ground state. In a two level system the unperturbed solutions to equation 3.1 are

$$H_0\psi_1 = E_1\psi_1, \tag{3.4a}$$

$$H_0\psi_2 = E_2\psi_2. \tag{3.4b}$$

Multiplying equation 3.3 from the left by Ψ_1^* and Ψ_2^* and integrating, two coupled equations relating the populations in each of the eigenstates can be written as

$$c_1\langle 1|H_{\mathrm{I}}|1\rangle + c_2\langle 1|H_{\mathrm{I}}|2\rangle e^{-\imath(E_2-E_1)t/\hbar} = \imath\hbar\frac{\partial c_1}{\partial t} \tag{3.5a}$$

$$c_2\langle 2|H_{\mathrm{I}}|2\rangle + c_1\langle 2|H_{\mathrm{I}}|1\rangle e^{\imath(E_2-E_1)t/\hbar} = \imath\hbar\frac{\partial c_2}{\partial t} \tag{3.5b}$$

where $|1\rangle = \psi_1$ and $|2\rangle = \psi_2$. Here we are concerned with electric dipole and electric quadrupole transitions where the final state labelled with quantum numbers j' and m' are not the same as the initial quantum numbers, hence by definition $\langle 1|H_{\mathrm{I}}|1\rangle = \langle 2|H_{\mathrm{I}}|2\rangle = 0$.

Defining the energy difference between states $|1\rangle$ and $|2\rangle$, $E_2 - E_1 = \hbar\omega_0$, equations 3.5 can be written as

$$c_2\langle 2|H_{\mathrm{I}}|1\rangle e^{-\imath\omega_0 t} = \imath\hbar\frac{\partial c_1}{\partial t}, \tag{3.6a}$$

$$c_1\langle 1|H_{\mathrm{I}}|2\rangle e^{\imath\omega_0 t} = \imath\hbar\frac{\partial c_2}{\partial t}. \tag{3.6b}$$

To find the matrix element between two states the form of the interaction Hamiltonian must be calculated. Expanding out equation 2.18, the Hamiltonian for an electron in an electromagnetic potential can be written as

$$\hat{H} = \frac{\hat{\boldsymbol{p}}^2}{2m} + q\phi\left(\boldsymbol{r},t\right) + \frac{q}{2m}\big(\hat{\boldsymbol{p}}\cdot\boldsymbol{A}\left(\boldsymbol{r},t\right) + \boldsymbol{A}\left(\boldsymbol{r},t\right)\cdot\hat{\boldsymbol{p}}\big) + \frac{q^2\boldsymbol{A}^2\left(\boldsymbol{r},t\right)}{2m}. \tag{3.7}$$

The Hamiltonian can be separated into three parts, the unperturbed energy, $\hat{H}_0$, the low intensity interaction with the electromagnetic field, $\hat{H}_{\mathrm{I}}$, and the nonlinear interactions, $\hat{H}_{\mathrm{NL}}$:

$$\hat{H}_0 = \frac{\hat{\boldsymbol{p}}^2}{2m} + q\phi\left(\boldsymbol{r},t\right) \tag{3.8a}$$

$$\hat{H}_{\mathrm{I}} = \frac{q}{2m}\big(\hat{\boldsymbol{p}}\cdot\boldsymbol{A}\left(\boldsymbol{r},t\right) + \boldsymbol{A}\left(\boldsymbol{r},t\right)\cdot\boldsymbol{p}\big) \tag{3.8b}$$

$$\hat{H}_{\mathrm{NL}} = \frac{q^2\boldsymbol{A}^2\left(\boldsymbol{r},t\right)}{2m}. \tag{3.8c}$$

From now on $\hat{H}_{\mathrm{NL}}$ is neglected as it is only relevant at high intensities [21]. Replacing the momentum operator with $\hat{\boldsymbol{p}} = -\imath\hbar\nabla$ and using the product rule we can see that the first term of $\hat{H}_{\mathrm{I}}$ operating on any scalar function, f, can be written as

$$\frac{q}{2m}\big(\hat{\boldsymbol{p}}\cdot(\boldsymbol{A}f)\big) = \frac{q\hbar}{\imath 2m}\left(\boldsymbol{A}\cdot\nabla f + f\nabla\cdot\boldsymbol{A}\right). \tag{3.9}$$

However, in the Coulomb gauge

$$\nabla\cdot\boldsymbol{A} = 0. \tag{3.10}$$

Substituting equations 3.9 and 3.10 into equation 3.8b the interaction Hamiltonian can be written as

$$\hat{H}_{\mathrm{I}} = \frac{q\hbar}{\imath m}\boldsymbol{A}\left(\boldsymbol{r},t\right)\cdot\nabla \tag{3.11}$$

$$= \frac{q}{m}\boldsymbol{A}\left(\boldsymbol{r},t\right)\cdot\hat{\boldsymbol{p}}. \tag{3.12}$$

Using Ehrenfest's theorem

$$\hat{\boldsymbol{p}} = \frac{m}{\imath\hbar}\left[\boldsymbol{r}, H_0\right], \tag{3.13}$$

the interaction Hamiltonian can be simplified to

$$\hat{H}_\mathrm{I} = \frac{q}{\imath\hbar}\boldsymbol{A}\cdot[\boldsymbol{r}, H_0]\,. \tag{3.14}$$

The vector potential for a plane wave can be written as

$$\boldsymbol{A} = \frac{A_0}{2}\hat{\boldsymbol{\epsilon}}\cdot\left(e^{\imath(\boldsymbol{k}\cdot\boldsymbol{r}-\omega_\mathrm{L}t)} + e^{-\imath(\boldsymbol{k}\cdot\boldsymbol{r}-\omega_\mathrm{L}t)}\right) \tag{3.15}$$

where $\hat{\boldsymbol{\epsilon}}$ is the unit vector describing the polarisation and ω_L is the laser frequency. We can write the Hamiltonian as two parts $\langle 2|H_\mathrm{I}|1\rangle = \langle 2|H_\mathrm{I}^+|1\rangle + \langle 2|H_\mathrm{I}^-|1\rangle$, where

$$H_\mathrm{I}^+ = \frac{qA_0}{2\imath\hbar}\hat{\boldsymbol{\epsilon}}\cdot[r, H_0]\,e^{-\imath(\boldsymbol{k}\cdot\boldsymbol{r}-\omega_\mathrm{L}t)} \tag{3.16a}$$

$$H_\mathrm{I}^- = \frac{qA_0}{2\imath\hbar}\hat{\boldsymbol{\epsilon}}\cdot[r, H_0]\,e^{\imath(\boldsymbol{k}\cdot\boldsymbol{r}-\omega_\mathrm{L}t)}. \tag{3.16b}$$

Substituting equation 3.16a into the matrix element above we find that

$$\langle 2|H_\mathrm{I}^+|1\rangle = \frac{qA_0}{2\imath\hbar}\hat{\boldsymbol{\epsilon}}\cdot\langle 2|\,[\boldsymbol{r}, H_0]\,e^{-\imath\boldsymbol{k}\cdot\boldsymbol{r}}|1\rangle e^{\imath\omega_\mathrm{L}t}. \tag{3.17}$$

Usually, the size of a wavefunction is much smaller than the wavelength of any incident light (except for x-rays). In this case the amplitude of the electromagnetic field can be written as a Taylor expansion. To the lowest order, $e^{\imath\boldsymbol{k}\cdot\boldsymbol{r}} \approx e^{-\imath\boldsymbol{k}\cdot\boldsymbol{r}} \approx 1$. This is called the dipole approximation and is only relevant for electric dipole (E1) transitions. Using this approximation in equation 3.17 we find

$$\langle 2|H_\mathrm{I}^+|1\rangle_\mathrm{E1} = \frac{qA_0}{2\imath\hbar}\hat{\boldsymbol{\epsilon}}\cdot\big(\langle 2|\boldsymbol{r}H_0|1\rangle - \langle 2|H_0\boldsymbol{r}|1\rangle\big)\,e^{\imath\omega_\mathrm{L}t} \tag{3.18a}$$

$$= \frac{qA_0}{2\imath\hbar}\hat{\boldsymbol{\epsilon}}\cdot\big(E_1\langle 2|\boldsymbol{r}|1\rangle - E_2\langle 2|\boldsymbol{r}|1\rangle\big)\,e^{\imath\omega_\mathrm{L}t} \tag{3.18b}$$

$$= \frac{\imath qA_0\omega_0}{2}\hat{\boldsymbol{\epsilon}}\cdot\langle 2|\boldsymbol{r}|1\rangle e^{\imath\omega_\mathrm{L}t}. \tag{3.18c}$$

Similarly for the other electric dipole matrix elements

$$\langle 2|H_\mathrm{I}^-|1\rangle_\mathrm{E1} = \frac{\imath qA_0\omega_0}{2}\hat{\boldsymbol{\epsilon}}\cdot\langle 2|\boldsymbol{r}|1\rangle e^{-\imath\omega_\mathrm{L}t}, \tag{3.19}$$

$$\langle 1|H_\mathrm{I}^+|2\rangle_\mathrm{E1} = -\frac{\imath qA_0\omega_0}{2}\hat{\boldsymbol{\epsilon}}\cdot\langle 1|\boldsymbol{r}|2\rangle e^{\imath\omega_\mathrm{L}t}, \tag{3.20}$$

$$\langle 1|H_\mathrm{I}^-|2\rangle_\mathrm{E1} = -\frac{\imath qA_0\omega_0}{2}\hat{\boldsymbol{\epsilon}}\cdot\langle 1|\boldsymbol{r}|2\rangle e^{-\imath\omega_\mathrm{L}t}. \tag{3.21}$$

Including the next term in the expansion of the field $e^{\imath\boldsymbol{k}\cdot\boldsymbol{r}} \approx 1 + \boldsymbol{i}\boldsymbol{k}\cdot\boldsymbol{r}$ and $e^{-\imath\boldsymbol{k}\cdot\boldsymbol{r}} \approx 1 - \boldsymbol{i}\boldsymbol{k}\cdot\boldsymbol{r}$

and inserting the second term into equations 3.16, we find

$$\begin{aligned}
\langle 2|H_{\mathrm{I}}^{+}|1\rangle &= \langle 2|H_{\mathrm{I}}^{+}|1\rangle_{\mathrm{E1}} + \frac{qA_0}{2m}e^{\imath\omega_{\mathrm{L}}t}\langle 2|\imath\left(\hat{\boldsymbol{\epsilon}}\cdot\boldsymbol{p}\right)\left(\boldsymbol{k}\cdot\boldsymbol{r}\right)|1\rangle \qquad (3.22\mathrm{a})\\
&= \langle 2|H_{\mathrm{I}}^{+}|1\rangle_{\mathrm{E1}} + \frac{qA_0}{2m}e^{\imath\omega_{\mathrm{L}}t}\left(\frac{\imath}{2}\hat{\boldsymbol{\epsilon}}\cdot\langle 2|\left(\boldsymbol{pr}-\boldsymbol{rp}\right)\cdot\boldsymbol{k}|1\rangle\right.\\
&\qquad\qquad\left.+\,\frac{\imath}{2}\hat{\boldsymbol{\epsilon}}\cdot\langle 2|\left(\boldsymbol{pr}+\boldsymbol{rp}\right)\cdot\boldsymbol{k}|1\rangle\right). \qquad (3.22\mathrm{b})
\end{aligned}$$

This expansion has been split into two parts, the asymmetric part refers to magnetic dipole transitions and the symmetric term refers to electric quadrupole transitions. Information about calculating the matrix element for magnetic dipole transitions can be found in reference [21]. Using equation 3.13 the matrix element for electric quadrupole transitions can be written as

$$\begin{aligned}
\langle 2|H_{\mathrm{I}}^{+}|1\rangle_{\mathrm{E2}} &= -\frac{qA_0}{2m}\frac{\imath}{2}\hat{\boldsymbol{\epsilon}}\cdot\langle 2|\boldsymbol{pr}+\boldsymbol{rp}|1\rangle\cdot\boldsymbol{k}e^{\imath\omega_{\mathrm{L}}t} \qquad (3.23\mathrm{a})\\
&= -\frac{qA_0}{2\hbar}\frac{1}{2}\hat{\boldsymbol{\epsilon}}\cdot\left(\langle 2|\left[\boldsymbol{r},H_0\right]\boldsymbol{r}|1\rangle+\langle 2|\boldsymbol{r}\left[\boldsymbol{r},H_0\right]|1\rangle\right)\cdot\boldsymbol{k}e^{\imath\omega_{\mathrm{L}}t} \qquad (3.23\mathrm{b})\\
&= -\frac{qA_0}{2\hbar}\frac{1}{2}\hat{\boldsymbol{\epsilon}}\cdot\left(\langle 2|\boldsymbol{rr}H_0|1\rangle-\langle 2|H_0\boldsymbol{rr}|1\rangle\right)\cdot\boldsymbol{k}e^{\imath\omega_{\mathrm{L}}t} \qquad (3.23\mathrm{c})\\
&= \frac{qA_0\omega_0}{4}\hat{\boldsymbol{\epsilon}}\cdot\langle 2|\boldsymbol{rr}|1\rangle\cdot\boldsymbol{k}e^{\imath\omega_{\mathrm{L}}t} \qquad (3.23\mathrm{d})\\
&= \frac{qA_0\omega_0\omega_{\mathrm{L}}}{4c}\hat{\boldsymbol{n}}\hat{\boldsymbol{\epsilon}}\cdot\langle 2|\boldsymbol{rr}|1\rangle e^{\imath\omega_{\mathrm{L}}t}, \qquad (3.23\mathrm{e})
\end{aligned}$$

where $\boldsymbol{k}=\omega\hat{\boldsymbol{n}}/c$. Similarly for the other electric quadrupole matrix elements

$$\begin{aligned}
\langle 2|H_{\mathrm{I}}^{-}|1\rangle_{\mathrm{E2}} &= -\frac{qA_0\omega_0\omega_{\mathrm{L}}}{4c}\hat{\boldsymbol{n}}\hat{\boldsymbol{\epsilon}}\cdot\langle 2|\boldsymbol{rr}|1\rangle e^{-\imath\omega t}, \qquad (3.24\mathrm{a})\\
\langle 1|H_{\mathrm{I}}^{+}|2\rangle_{\mathrm{E2}} &= -\frac{qA_0\omega_0\omega_{\mathrm{L}}}{4c}\hat{\boldsymbol{n}}\hat{\boldsymbol{\epsilon}}\cdot\langle 1|\boldsymbol{rr}|2\rangle e^{\imath\omega t}, \qquad (3.24\mathrm{b})\\
\langle 1|H_{\mathrm{I}}^{-}|2\rangle_{\mathrm{E2}} &= \frac{qA_0\omega_0\omega_{\mathrm{L}}}{4c}\hat{\boldsymbol{n}}\hat{\boldsymbol{\epsilon}}\cdot\langle 1|\boldsymbol{rr}|2\rangle e^{-\imath\omega t}. \qquad (3.24\mathrm{c})
\end{aligned}$$

Equations 3.6 can be rewritten by substituting the matrix elements above and neglecting terms which oscillate at frequency $\omega_0+\omega_{\mathrm{L}}$, we find

$$\begin{aligned}
\frac{dc_1}{dt} &= \frac{c_2}{2}\Omega_{\mathrm{E1,\ E2}}e^{\imath(\omega_{\mathrm{L}}-\omega_0)t}, \qquad (3.25\mathrm{a})\\
\frac{dc_2}{dt} &= \frac{c_1}{2}\Omega_{\mathrm{E1,\ E2}}e^{-\imath(\omega_{\mathrm{L}}-\omega_0)t}, \qquad (3.25\mathrm{b})
\end{aligned}$$

where

$$\Omega_{\mathrm{E1}} = \frac{qA_0\omega_0}{\hbar}\hat{\boldsymbol{\epsilon}} \cdot \langle 1|\boldsymbol{r}|2\rangle, \tag{3.26a}$$

$$\Omega_{\mathrm{E2}} = \frac{qA_0\omega_0\omega_{\mathrm{L}}}{2\hbar c}\hat{\boldsymbol{n}}\hat{\boldsymbol{\epsilon}} \cdot \langle 1|\boldsymbol{r}\boldsymbol{r}|2\rangle, \tag{3.26b}$$

are called Rabi frequencies for electric dipole and electric quadrupole transitions. Differentiating equation 3.25, the decoupled second order equations describing the two level system are

$$\frac{d^2c_1}{dt^2} - \imath\left(\omega_{\mathrm{L}} - \omega_0\right)\frac{dc_1}{dt} + \left|\frac{\Omega_{\mathrm{E1,\ E2}}}{2}\right|^2 c_1 = 0, \tag{3.27a}$$

$$\frac{d^2c_2}{dt^2} + \imath\left(\omega_{\mathrm{L}} - \omega_0\right)\frac{dc_2}{dt} + \left|\frac{\Omega_{\mathrm{E1,\ E2}}}{2}\right|^2 c_2 = 0. \tag{3.27b}$$

Using the trial solution $c_2 = \beta e^{pt}$, the general solution to equation 3.27b is

$$c_2 = \exp\left[-\frac{\imath\left(\omega_L - \omega_0\right)t}{2}\right]\left\{\beta_1\exp\left[\frac{\imath\delta t}{2}\right] + \beta_2\exp\left[-\frac{\imath\delta t}{2}\right]\right\}, \tag{3.28}$$

where $\delta = \sqrt{\left(\omega_{\mathrm{L}} - \omega_0\right)^2 + |\Omega_{\mathrm{E1,\ E2}}|^2}$. Using the initial condition $c_2\left(t = 0\right) = 0$, equation 3.28 reduces to

$$c_2 = \beta\exp\left[-\frac{\imath\left(\omega_{\mathrm{L}} - \omega_0\right)t}{2}\right]\sin\left(\frac{\delta t}{2}\right). \tag{3.29}$$

Substituting equation 3.29 into equation 3.25a and using the initial condition $c_1\left(t = 0\right) = 1$ we find $\beta = \Omega_{\mathrm{E1,\ E2}}/\delta$ and the amplitudes of the quantum states can be written as

$$c_1 = \exp\left[\frac{\left(\omega_{\mathrm{L}} - \omega_0\right)t}{2}\right]\left[\cos\left(\frac{\delta t}{2}\right) - \frac{\imath\left(\omega_{\mathrm{L}} - \omega_0\right)}{\delta}\sin\left(\frac{\delta t}{2}\right)\right], \tag{3.30a}$$

$$c_2 = \frac{\Omega_{\mathrm{E1,\ E2}}}{\delta}\exp\left[-\frac{\imath\left(\omega_{\mathrm{L}} - \omega_0\right)t}{2}\right]\sin\left(\frac{\delta t}{2}\right). \tag{3.30b}$$

Hence the probabilities of finding the system in states ψ_1 and ψ_2 are

$$|c_1|^2 = \cos^2\left(\frac{\delta t}{2}\right) + \frac{\left(\omega_{\mathrm{L}} - \omega_0\right)^2}{\delta^2}\sin^2\left(\frac{\delta t}{2}\right), \tag{3.31a}$$

$$|c_2|^2 = \frac{\Omega^2}{\delta^2}\sin^2\left(\frac{\delta t}{2}\right). \tag{3.31b}$$

These well known results assume only coherent population transfer from one state to another. Spontaneous decay is not included, and becomes important when the laser intensity is around or below the saturation intensity. In practice, electric dipole and quadrupole transitions are used for different purposes. Electric dipole transitions are used for Doppler cooling where spontaneous decay is useful and quadrupole transitions are used for coherent manipulation or sideband cooling.

To calculate the Rabi frequencies in equations 3.26

$$|\Omega_{\mathrm{E1}}| = \left|\frac{qA_0\omega_{21}}{2\hbar}\left\langle 1\left|\hat{r}_i\right|2\right\rangle \boldsymbol{\epsilon}_i\right|, \tag{3.32}$$

$$|\Omega_{\mathrm{E2}}| = \left|\frac{qA_0\omega_{21}\omega_{\mathrm{L}}}{4\hbar c}\left\langle 1\left|\hat{r}_i\hat{r}_j\right|2\right\rangle \boldsymbol{\epsilon}_i n_j\right|, \tag{3.33}$$

where $\hat{r}_i$ and $\hat{r}_j$ are summed over repeated indices i and j where $i, j = x, y, z$.

Transforming from Cartesian tensors to irreducible tensors, the matrix element is split between transitions which couple different changes in magnetic quantum number m,

$$\left\langle 1\left|\hat{r}_i\right|2\right\rangle \boldsymbol{\epsilon}_i = \sum_{q=-1}^{1}\left\langle 1\left|rC_q^{(1)}\right|2\right\rangle c_i^{(q)}\boldsymbol{\epsilon}_i \tag{3.34}$$

$$\left\langle 1\left|\hat{r}_i\hat{r}_j\right|2\right\rangle \boldsymbol{\epsilon}_i n_j = \sum_{q=-2}^{2}\left\langle 1\left|r^2C_q^{(2)}\right|2\right\rangle c_{ij}^{(q)}\boldsymbol{\epsilon}_i n_j \tag{3.35}$$

where $C_q^k = Y_{kq}\sqrt{4\pi/(2k+1)}$, are the renormalised spherical harmonics and $c_i^{(q)}$ are normalised spherical basis vectors. The second order tensors for quadrupole transitions can be calculated by using the following relation

$$c_{ij}^q = \sqrt{\frac{10}{3}}(-1)^q \sum_{m_1,m_2=-1}^{1}\begin{pmatrix} 1 & 1 & 2 \\ m_1 & m_2 & -q \end{pmatrix} c_i^{(m_1)}c_j^{(m_2)}. \tag{3.36}$$

As with all matrices, the first index (i) refers to columns and the second (j) to rows. These tensors are listed explicitly in the appendix of reference [24].

Using the Wigner-Eckart theorem any dependence on angular momentum and magnetic quantum numbers can be removed from the matrix element and placed in a 3-j symbol (or Clebsch-Gordan coefficient).

$$\left\langle 1\left|\hat{r}_i\right|2\right\rangle \boldsymbol{\epsilon}_i = \left\langle 1\left\|rC_q^{(1)}\right\|2\right\rangle \sum_{q=-1}^{1}\begin{pmatrix} j & 1 & j' \\ -m_j & q & m_j' \end{pmatrix} c_i^{(q)}\boldsymbol{\epsilon}_i \tag{3.37}$$

$$\left\langle 1\left|\hat{r}_i\hat{r}_j\right|2\right\rangle \boldsymbol{\epsilon}_i n_j = \left\langle 1\left\|r^2C_q^{(2)}\right\|2\right\rangle \sum_{q=-2}^{2}\begin{pmatrix} j & 2 & j' \\ -m_j & q & m_j' \end{pmatrix} c_{ij}^{(q)}\boldsymbol{\epsilon}_i n_j. \tag{3.38}$$

One of the rules for 3-j symbols is that $(-m_j) + m_j' + q = 0$. This can be used to produce table 3.1. The Clebsch-Gordan coefficients for the transitions relevant to Ca^+ ions are

Transition	q
π	0
σ^+	-1
σ^-	1
δ^+	-2
δ^-	2

Table 3.1: q values for different transitions.

listed in appendix A. The relation between Clebsch-Gordan coefficients and 3-j symbols is given by

$$\begin{pmatrix} j_1 & j_2 & j \\ m_1 & m_2 & m \end{pmatrix} \equiv \frac{(-1)^{j_1-j_2-m}}{\sqrt{2j+1}} \langle j_1 j_2 m_1 m_2 | j_1 j_2 j m \rangle \text{ [25].} \tag{3.39}$$

3.1.1 Geometry

Optical access in a Penning trap is highly restricted by the presence of the magnet. This section shows how the interaction between light and atoms depends on the geometry of the situation; the angle of incidence between the laser light and quantisation axis of the atom and also the polarisation of that light field.

The polarisation of a laser beam can be described exactly by a point on the surface of a Poincaré sphere as shown in figure 3.1(a). For a laser beam travelling in the positive z-direction, vectors describing the laser unit vector and polarisation are given by

$$\hat{\boldsymbol{k}} = \begin{pmatrix} 0 \\ 0 \\ 1 \end{pmatrix}, \tag{3.40}$$

$$\hat{\boldsymbol{\epsilon}} = \begin{pmatrix} \cos(\beta) \\ e^{i\gamma}\sin(\beta) \\ 0 \end{pmatrix}. \tag{3.41}$$

For linear polarisation, β is the angle between the polarisation and the magnetic field, which has the bounds $0 \leq \beta \leq \pi/2$ and is multiplied by 2 to find a position on the Poincaré sphere. The ellipticity of the polarisation is a function of γ. When the laser beam is rotated around the axis coming out of the page, the y-axis (see figure 3.1(b)), the vectors in equations 3.40 and 3.41 are also rotated. This gives vectors for the laser angle and

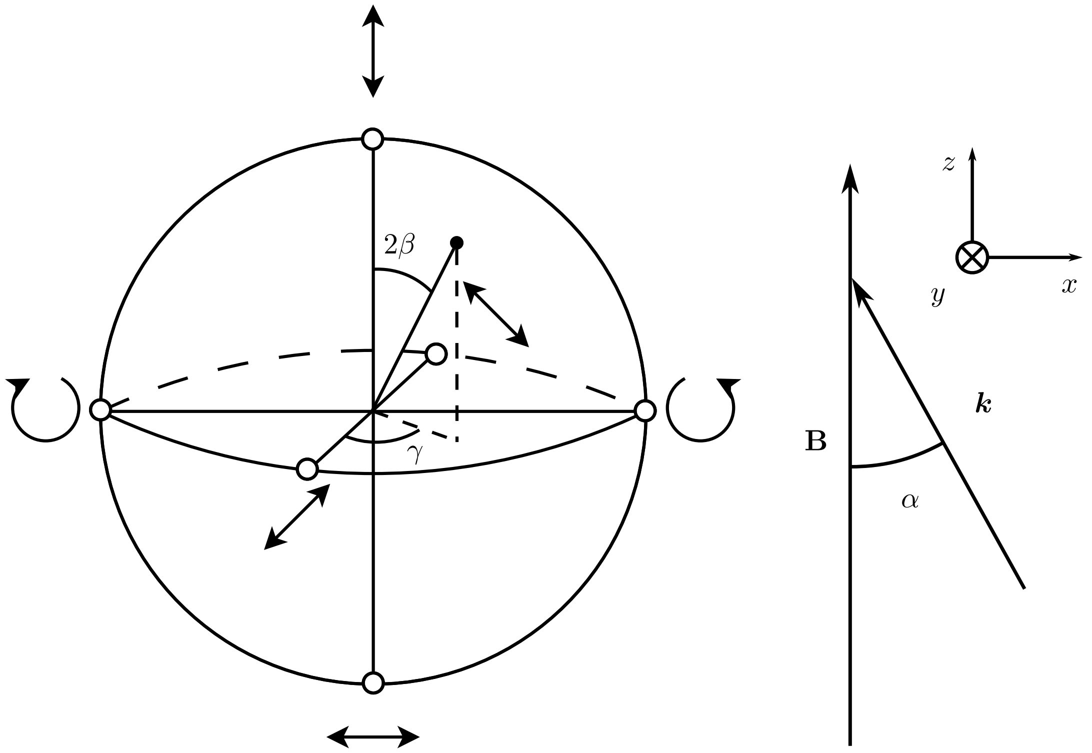

(a) (b)

Figure 3.1: The three angles α, β and γ describe the direction and polarisation of the laser beam, where α gives the angle between the laser wavevector and the magnetic field.

polarisation of the light at arbitrary angles of incidence

$$\hat{\boldsymbol{k}}' = \underline{\underline{R_y}} \cdot \hat{\boldsymbol{k}} = \begin{pmatrix} \cos(\alpha) & 0 & -\sin(\alpha) \\ 0 & 1 & 0 \\ \sin(\alpha) & 0 & \cos(\alpha) \end{pmatrix} \cdot \begin{pmatrix} 0 \\ 0 \\ 1 \end{pmatrix} = \begin{pmatrix} -\sin(\alpha) \\ 0 \\ \cos(\alpha) \end{pmatrix}, \tag{3.42}$$

$$\hat{\boldsymbol{\epsilon}}' = \underline{\underline{R_y}} \cdot \hat{\boldsymbol{\epsilon}} = \begin{pmatrix} \cos(\alpha) & 0 & -\sin(\alpha) \\ 0 & 1 & 0 \\ \sin(\alpha) & 0 & \cos(\alpha) \end{pmatrix} \cdot \begin{pmatrix} \cos(\beta) \\ e^{i\gamma}\sin(\beta) \\ 0 \end{pmatrix} = \begin{pmatrix} \cos(\alpha)\cos(\beta) \\ e^{i\gamma}\sin(\beta) \\ \sin(\alpha)\cos(\beta) \end{pmatrix}. \tag{3.43}$$

3.1.2 Radiation emission patterns

We can determine the angular distributions of emitted radiation. These are exactly the same as for a classical oscillating dipole or quadrupole and are simply listed in table 3.2, plotted in figure 3.2 and are rigorously derived in reference [26].

The normalisation condition means that the sum of emission patterns for the 3 dipole or the 5 quadrupole transitions are spherically symmetric.

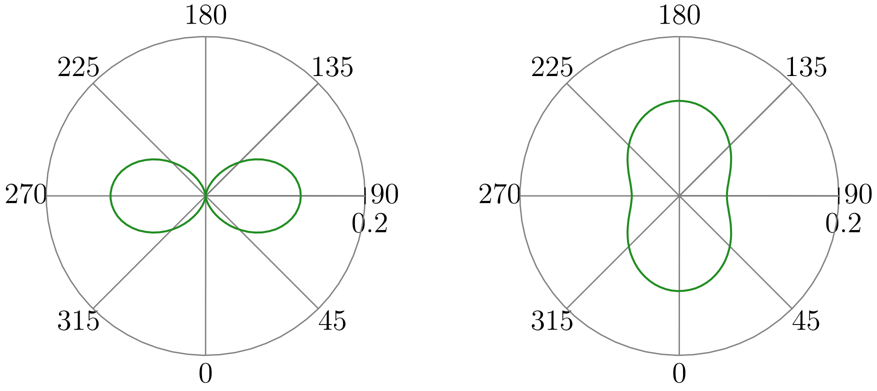

(a) Dipole $\Delta m = 0$

(b) Dipole $\Delta m = \pm 1$

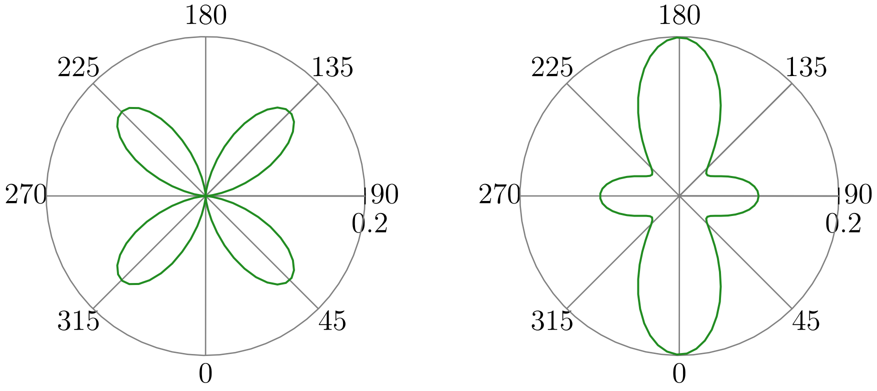

(c) Quadrupole $\Delta m = 0$

(d) Quadrupole $\Delta m = \pm 1$

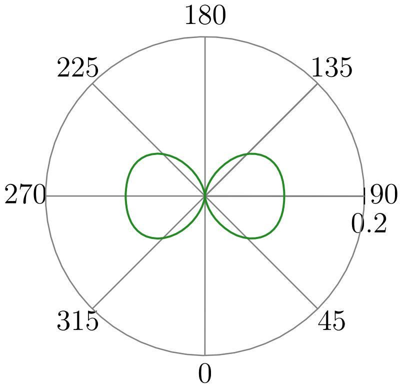

(e) Quadrupole $\Delta m = \pm 2$

Figure 3.2: Radiation emission patterns for dipole and quadrupole transitions as a function of angle relative to the quantisation axis for different values of Δm. The quantisation axis is set vertically.

Multipole	$\lvert\Delta m\rvert$ 0	1	2
Dipole	$\frac{3}{8\pi}\sin^2\alpha$	$\frac{3}{16\pi}\left(1+\cos^2\alpha\right)$	
Quadrupole	$\frac{15}{8\pi}\sin^2\alpha\cos^2\alpha$	$\frac{5}{16\pi}\left(1-3\cos^2\alpha+4\cos^4\alpha\right)$	$\frac{5}{16\pi}\left(1-\cos^4\alpha\right)$

Table 3.2: List of radiation emission patterns for different transitions.

3.1.3 Polarisation coefficients

The last two or three terms in equations 3.37 and 3.38 respectively require summing after matrix multiplication. The moduli of these expressions

$$\left|f^{(q)}\right| = \left|c_i^{(q)}\boldsymbol{\epsilon}_i\right| = \sqrt{\left(c_i^{(q)}\boldsymbol{\epsilon}_i\right)\left(c_i^{(q)}\boldsymbol{\epsilon}_i\right)^*}, \tag{3.44a}$$

$$\left|g^{(q)}\right| = \left|c_{ij}^{(q)}\boldsymbol{\epsilon}_i\boldsymbol{n}_j\right| = \sqrt{\left(c_{ij}^{(q)}\boldsymbol{\epsilon}_i\boldsymbol{n}_j\right)\left(c_{ij}^{(q)}\boldsymbol{\epsilon}_i\boldsymbol{n}_j\right)^*}, \tag{3.44b}$$

are then substituted into equations 3.32 and 3.33. A list of these functions for the 3 dipole transitions and 5 quadrupole transitions are shown in appendix B.

3.1.4 Optimum Polarisation

The optimum polarisation to stimulate a transition at any given angle, α, is identical to the polarisation of light emitted through spontaneous decay from those transitions. This quantity would be useful to identify because the laser propagation angle is often constrained by trap and magnet geometry which restricts optical access. The emitted polarisation pattern can be calculated from classical electromagnetic theory. They are also listed explicitly in reference [27], unfortunately in a different co-ordinate system. In reference [27] polarisation is described in non-normalised spherical polar co-ordinates, $\boldsymbol{r}$, $\boldsymbol{\theta}$ & $\boldsymbol{\phi}$ with unit vectors $\boldsymbol{r_0}$, $\boldsymbol{\theta_0}$ & $\boldsymbol{\phi_0}$. These coordinates are based in real space using imaginary numbers to represent phase difference between the components, rather than using a Poincaré sphere which gives a normalised description of the polarisation using only real numbers, but which cannot be directly mapped on to real space.

It is possible to convert between the two representations using the equations

$$\beta = \operatorname{atan}\left(\frac{|\boldsymbol{\phi}|}{|\boldsymbol{\theta}|}\right),$$

$$\gamma = 90^\circ \text{ iff } \Im\{\boldsymbol{\phi}\}\times\boldsymbol{\theta} > 0,$$

$$\gamma = 270^\circ \text{ iff } \Im\{\boldsymbol{\phi}\}\times\boldsymbol{\theta} < 0.$$

The optimum polarisations in both coordinate systems are listed in table 3.3.

Transition	Polar coordinates	β	$\gamma = 90°$	$\gamma = 270°$
		Dipole & Quadrupole		
π	$\boldsymbol{\theta_0}$	0°	N/A	N/A
		Dipole		
σ^+	$\cos(\alpha)\,\boldsymbol{\theta_0} + i\boldsymbol{\phi_0}$	$\arctan\left(\frac{1}{\lvert\cos(\alpha)\rvert}\right)$	$0 < \alpha < \pi/2$	$\pi/2 < \alpha < \pi$
σ^-	$\cos(\alpha)\,\boldsymbol{\theta_0} - i\boldsymbol{\phi_0}$		$\pi/2 < \alpha < \pi$	$0 < \alpha < \pi/2$
		Quadrupole		
σ^+	$\cos(2\alpha)\,\boldsymbol{\theta_0} + i\cos(\alpha)\,\boldsymbol{\phi_0}$	$\arctan\left(\frac{\lvert\cos(\alpha)\rvert}{\lvert\cos(2\alpha)\rvert}\right)$	$0 < \alpha < \pi/4$ $\pi/2 < \alpha < 3\pi/4$	$\pi/4 < \alpha < \pi/2$ $3\pi/4 < \alpha < \pi$
σ^-	$\cos(2\alpha)\,\boldsymbol{\theta_0} - i\cos(\alpha)\,\boldsymbol{\phi_0}$		$\pi/4 < \alpha < \pi/2$ $3\pi/4 < \alpha < \pi$	$0 < \alpha < \pi/4$ $\pi/2 < \alpha < 3\pi/4$
δ^+	$\cos(\alpha)\,\boldsymbol{\theta_0} + i\boldsymbol{\phi_0}$	$\arctan\left(\frac{1}{\lvert\cos(\alpha)\rvert}\right)$	$0 < \alpha < \pi/2$	$\pi/2 < \alpha < \pi$
δ^-	$\cos(\alpha)\,\boldsymbol{\theta_0} - i\boldsymbol{\phi_0}$		$\pi/2 < \alpha < \pi$	$0 < \alpha < \pi/2$

Table 3.3: The optimal laser polarisation for stimulating an atomic transition at a specific angle is the same as the polarisation for

3.2 Interaction with external states

Up until this point we have only considered a free atom, now we shall consider an ion trapped in a harmonic potential with angular oscillation frequency, ω. In this treatment only one set of harmonic oscillator levels will be considered. This situation can be realised, for example, if the laser beam is aligned parallel to the axial motion. A similar argument can be made for the radial direction with the modified cyclotron and magnetron motion but in this case two different eigenmodes must be considered simultaneously. When the ion oscillates in the trap, its transition frequency is modulated in the laboratory frame, producing sidebands, just as classical phase modulation can produce sidebands on RF and laser light. However, in this case, the motion of the ion must be treated quantum mechanically.

The Hamiltonian with the trapping potential can be written as

$$H_0 = \frac{1}{2}\left[\frac{p^2}{m} + m\omega^2 x^2 + \hbar\omega_0\sigma_z\right], \tag{3.45}$$

$$H_{\mathrm{I}} = \frac{\hbar\Omega}{2}\left[e^{\imath(kx-\omega_{\mathrm{L}}t+\phi)}\sigma^+ + e^{-\imath(kx-\omega_{\mathrm{L}}t)}\sigma^-\right], \tag{3.46}$$

where $\sigma_z = |e\rangle\langle e| - |g\rangle\langle g|\,, \sigma_+ = |e\rangle\langle g|$ and $\sigma_- = |g\rangle\langle e|$ ($|g\rangle$ and $|e\rangle$ are the ground and excited electronic states respectively). Using equations 2.23 in the $\hat{x}$ and $\hat{p}$ basis

$$\hat{x} = \sqrt{\frac{\hbar}{2\omega m}}\left(\hat{a} + \hat{a}^\dagger\right), \tag{3.47a}$$

$$\hat{p} = \imath\sqrt{\frac{\hbar m\omega}{2}}\left(\hat{a}^\dagger - \hat{a}\right). \tag{3.47b}$$

We can rewrite the Hamiltonian using the commutation relation $[a, a^\dagger] = 1$ so that

$$H_0 = \hbar\omega\left(\hat{a}^\dagger\hat{a} + \frac{1}{2}\right), \tag{3.48}$$

$$H_{\mathrm{I}} = \frac{\hbar\Omega}{2}\left\{e^{\imath\left[\eta\left(\hat{a}+\hat{a}^\dagger\right)-\omega_{\mathrm{I}}t\right]}\sigma^+ + e^{-\imath\left[\eta\left(\hat{a}+\hat{a}^\dagger\right)-\omega_{\mathrm{I}}t\right]}\sigma^-\right\}, \tag{3.49}$$

where the Lamb-Dicke parameter, $\eta = k\sqrt{\frac{\hbar}{2\omega m}}$, is proportional to the ratio of the photon recoil to the trap oscillation frequency. Now we can transform into the interaction picture where part of the time dependence is taken into the operators so that $\underset{\sim}{\hat{a}} = \hat{a}e^{-\imath\omega t}$ and $\underset{\sim}{\hat{a}}^\dagger = \hat{a}^\dagger e^{\imath\omega t}$. The Hamiltonian in this case can be written as $\underset{\sim}{H}_I = e^{\frac{\imath H_0 t}{2}} H_I e^{-\frac{\imath H_0 t}{2}}$. Expanding this out, we find that

$$H_{\mathrm{I}} = \frac{\hbar\Omega}{2}\left[\sigma^+ e^{\imath\eta\left(\underset{\sim}{a}+\underset{\sim}{a}^\dagger\right)}e^{-\imath\Delta t} + \sigma^- e^{-\imath\eta\left(\underset{\sim}{a}+\underset{\sim}{a}^\dagger\right)}e^{\imath\Delta t}\right], \tag{3.50}$$

where $\Delta = \omega_{\mathrm{L}} - \omega_0$. In the case where the detuning is zero, the carrier transition is stimulated but when $\Delta = \delta n \times \omega$ where δn is an integer, a motional sideband will be excited instead. To maintain energy conservation the ion will either gain or lose δn phonons in the process. Applying Schroedinger's equation, to the coherent superposition $\Psi = \sum_n \left(c_n\left|S, n\right\rangle + d_n\left|D, n\right\rangle\right)$, where S and D are internal states and n labels the occupation of external states, the two coupled equations describing the evolution of the system can be written as

$$\dot{c}_n = -\imath^{1-|\delta n|}e^{\imath(\omega_0-\delta n\omega)t}\frac{\Omega_{n',n}}{2}d_{n'}, \tag{3.51a}$$

$$\dot{d}_{n'} = -\imath^{1+|\delta n|}e^{\imath(\omega_0-\delta n\omega)t}\frac{\Omega_{n',n}}{2}c_n, \tag{3.51b}$$

where the modified Rabi frequency between motional states is

$$\Omega_{n',n} = \Omega\left\langle n'\right| e^{\imath\eta\left(a+a^\dagger\right)}\left|n\right\rangle. \tag{3.52}$$

Solving equations 3.51 in a similar way to equations 3.25 we once again find an oscillation of amplitude between the two states at the modified Rabi frequency. This kind of interaction allows the ladder of states described in section 2.1.2 to be convolved with the electronic transitions in section 3.1. Coupling the internal and external states in this way has been crucial for many implementations of trapped ion quantum information processing [1] and is essential for sideband cooling [28]. The solution to the matrix element in equation 3.52 is

$$\Omega_{n',n} = \Omega \left[\frac{n_<!}{n_>!}\right]^{1/2} \eta^{|\delta n|} e^{-\eta^2/2} L_{n_<}^{|\delta n|}\left(\eta^2\right), \tag{3.53}$$

where $n_<$ ($n_>$) is the lesser (greater) of n and n' and $L_{n_<}^{|\delta n|}\left(\eta^2\right)$ is an associated Laguerre polynomial [29]. In the Lamb-Dicke regime, $\eta\,(2n+1) \ll 1$, a simpler expression can be obtained by taking a Taylor expansion of the exponential in equation 3.52. After Doppler cooling which is explained in more detail in section 3.4.1 the ion is left in a thermal state. Decomposing this into Fock or number states the normalised population distribution is given by

$$P(n) = \frac{\bar{n}^n}{(\bar{n}+1)^{n+1}}, \tag{3.54}$$

where $\bar{n}$ is the mean vibrational quantum number. All the experiments in this thesis were done in this situation. To calculate the predicted Rabi oscillation, the thermal state probability must be multiplied by equation 3.31b at zero detuning and summed over all number states using

$$P_e\,(t) = \frac{1}{\bar{n}+1} \sum_{\substack{n=0 \\ n'=0}}^{\infty} \left(\frac{\bar{n}}{\bar{n}+1}\right)^n \sin^2\left(\frac{\Omega_{n',n}t}{2}\right). \tag{3.55}$$

We can simulate how the motional sideband spectrum should appear as a function of time. This is most easily done for the axial spectrum because the laser can be orientated to only interact with the motion parallel to the magnetic field. We assume that the ion has been cooled to the Doppler limit in a Penning trap, $\bar{n} = \gamma/4\omega_z$ [15]. The population distributions are shown in figure 3.3 and Rabi oscillation induced on the carrier and first order sidebands are shown in figure 3.4 for two different trap parameters. The experiments carried out in this thesis were done in a 1.85 T magnetic field at a range of axial frequencies from 30–200 kHz. It is clear that even when the trap frequency is set at 200 kHz, more than the first sidebands will be visible (for $^{40}\mathrm{Ca}^+$ ions in a 200 kHz trap stimulated on a 729 nm transition $\eta = 0.22$). By calculating the Rabi oscillations for higher order sidebands and plotting the excitation probability at different times we can see how the spectrum should evolve. We are in the high temperature limit and some features of the spectrum can be described classically. This is simply an illustration of the correspondence principle. The sidebands should be resolved because the ion is oscillating at a fixed frequency, however, the amplitude of individual sidebands is dependent on the thermal state distribution. This population distribution and the value of η which determines the coupling strength to

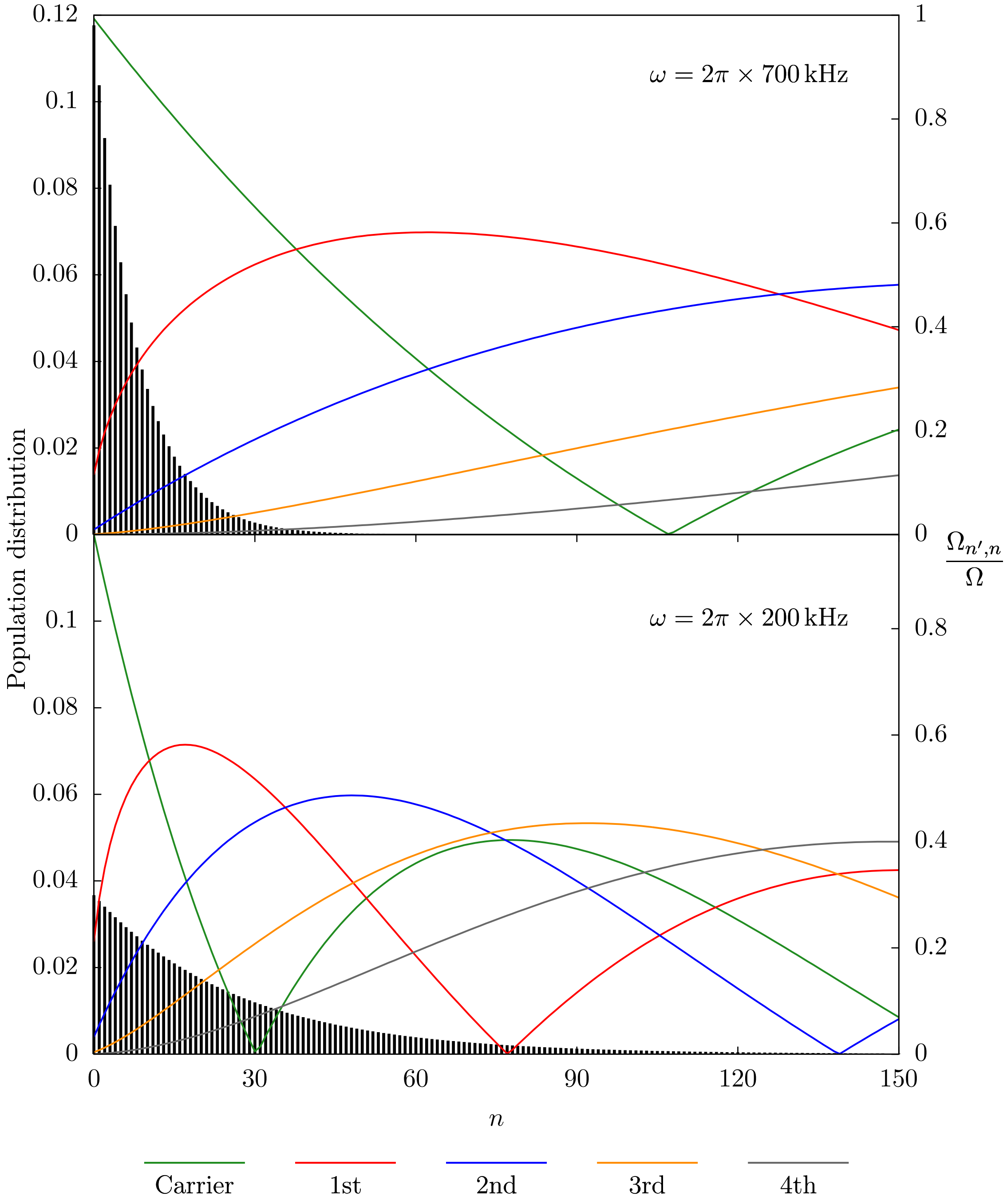

Figure 3.3: The population distributions in a trap decomposed into number states with a 700 kHz (200 kHz) axial frequency in the top (bottom) plot cooled to $\bar{n} = \gamma/(4\omega_z)$ (black lines). The continuous lines are the coupling strengths on the carrier and 1st to 4th blue sideband transitions. The red sidebands are not shown for clarity only.

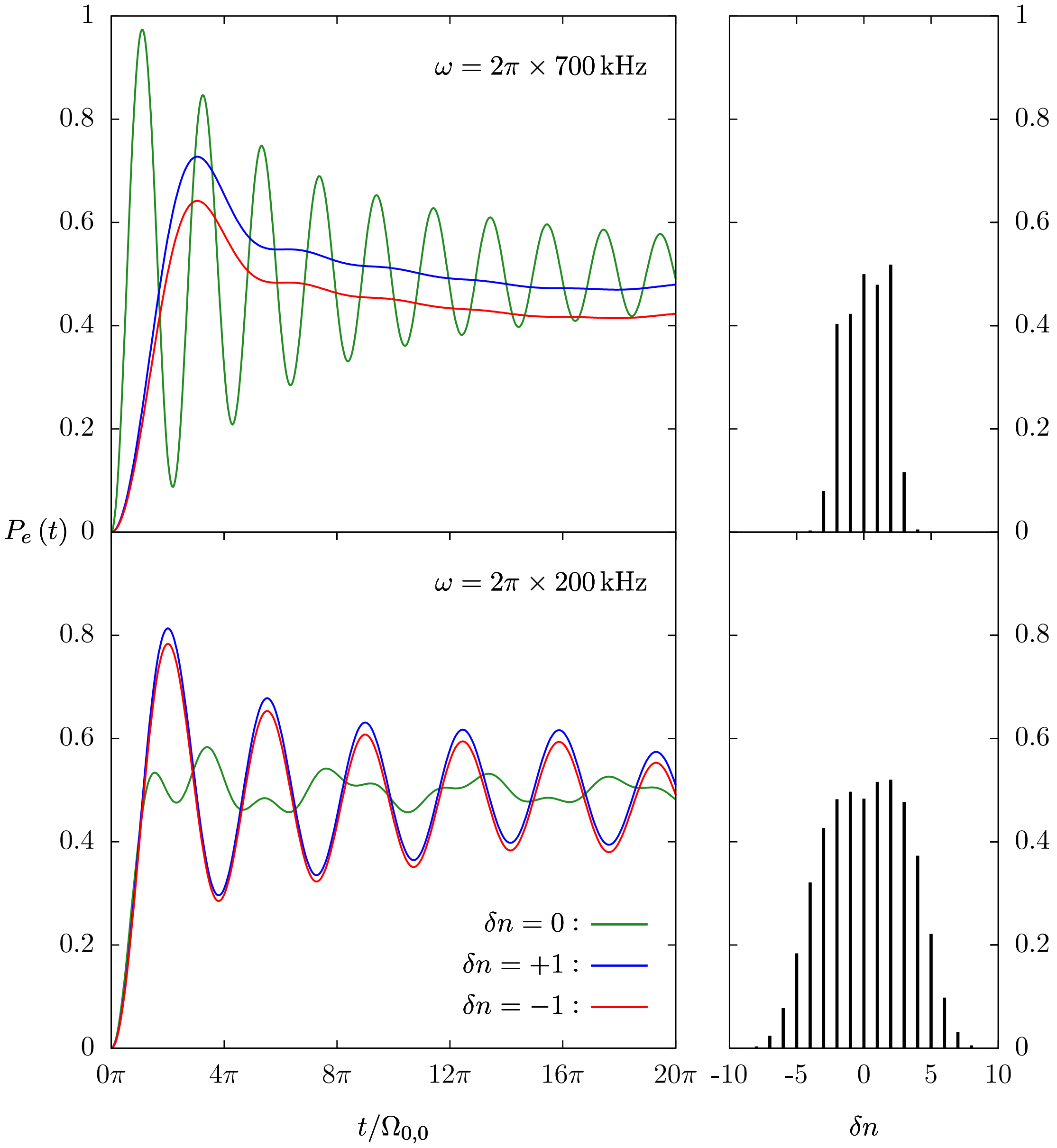

Figure 3.4: Predicted Rabi oscillations on carrier (drawn in green) and first red ($\delta n = -1$) and blue sidebands ($\delta n = +1$) for a mode with $\omega = 2\pi \times 700\,\mathrm{kHz}$ and $2\pi \times 200\,\mathrm{kHz}$ oscillation frequencies cooled to $\bar{n} = \gamma/4\omega_z$. The predicted sideband spectrum for $\Omega t = 20\pi$ is substituted into equation 3.55 and shown by calculating all Rabi oscillations to ±10 sidebands.

different sidebands as a function of occupation number and sets the envelope which contains the sidebands. In the case of a classical thermal state, we expect a Gaussian envelope just as we would for Doppler broadening in a transition without resolved sidebands. In the case where the population is distributed over a small range of number states, the excited state population oscillates between 0 and 1 but would eventually reach a steady state excited population of 0.5. In the intermediate regime between a classical and quantum system, the Rabi oscillations for each sideband must be calculated individually as shown in figure 3.4.

3.3 Broadening Mechanisms

During spectroscopy, the recorded linewidth is often broader than the linewidth that would be predicted by the Einstein A coefficient. The final lineshape is formed from a convolution of both the natural Lorentzian and the lineshapes from the different broadening mechanisms.

3.3.1 Doppler Broadening

For an atomic gas with the thermal velocity distribution, there is a Doppler shift depending on whether the atoms are moving towards or away from the laser. This shift leads to a broadening of the atomic transition, with a Gaussian profile. In a situation where the Doppler shift is small compared to the natural linewidth, we should expect a predominantly Lorentzian profile. It is simple to calculate the effect of Doppler broadening. The derivation in this section closely follows that in reference [30]. The atom can absorb light with a frequency

$$\omega = \omega_0 + kv \tag{3.56}$$

where ω_0 is the transition frequency at rest in the lab frame, k is the wavevector and v is the atom's velocity in the lab frame. Here we only consider a thermal distribution with the fraction of atoms in a velocity range dv, i.e.

$$f(v)dv = \frac{1}{u\sqrt{\pi}} \exp\left(-\frac{v^2}{u^2}dv\right), \tag{3.57}$$

where $u = \sqrt{2k_BT/m}$. Substituting equation 3.56 into equation 3.57 we can find the lineshape from this broadening mechanism,

$$G(\omega) = \frac{c}{u\omega_0\sqrt{\pi}} \exp\left[-\left(\frac{c}{u}\right)^2 \left(\frac{\omega-\omega_0}{\omega_0}\right)^2\right]. \tag{3.58}$$

This derivation is based on an ensemble of atoms with a Maxwell-Boltzmann distribution of energies. However, it also applies to a single particle where the population is a thermal distribution of number states.

3.3.2 Laser linewidth

Another source of spectral broadening which has not been mentioned until now is the laser linewidth. This is another factor, which convolves with the natural linewidth to give the eventual lineshape. If during the interrogation time the laser linewidth is of the same order, or even broader than the natural linewidth, this effect is clearly noticeable.

If a pulsed laser scheme is used, in the frequency domain the laser is broadened simply due to the time-bandwidth theorem. If the laser is on for 1 ms, the minimum linewidth is approximately 1 kHz. Also if the pulse is turned on and off in a *top-hat* style, then in the frequency domain it has the form of a sinc function. To produce the narrowest linewidth the pulse should have a Gaussian temporal profile.

Electric dipole transitions usually have scattering rate of approximately 10 MHz and, over short time scales, lasers with linewidths one tenth of this are commonly commercially available. It is usually not difficult to set up an optical system so that the laser linewidth is negligible in this case. However, stabilising a laser so that it does not broaden an electric quadrupole transition, which tend to have a natural linewidth in the 1 Hz range, is extremely technically challenging.

3.4 Laser cooling

Laser cooling was first demonstrated in 1978 on magnesium ions in a Penning trap [31] and in the same year on barium ions in an RF trap [32]. In 1989 laser cooling to the ground state of a bound potential was achieved for the first time, on this occasion, using a mercury ion in a Paul trap [16]. However, no groups have ground state cooled or previously performed optical motional sideband spectroscopy on a particle in a Penning trap. The negative energy in the magnetron motion and large magnetic field required for trapping lead to several complications in the laser cooling of ions in a Penning trap. I received have many hours of help from one of my supervisors, Prof. Richard Thompson, to help me understand the theoretical basis of laser cooling in a Penning trap.

3.4.1 Doppler Cooling

Doppler cooling is used in the regime where the motional sidebands are not resolved, i.e. $\omega < \gamma$. By only scattering photons when the atom has a particular velocity, light pressure exerted on a particle can be used to cool the particle's thermal motion [33]. This technique is used in our experiment to reduce the ion's equivalent temperature by 5–6 orders of magnitude from approximately 500 K down to around 1 mK.

This form of cooling works well with the axial and the modified cyclotron motion because the magnitude of the orbit decreases as the energy of the particle is reduced. However, to contract the magnetron motion, the energy of the mode must be increased. Hence, simply tuning the laser frequency below the atomic transition resonance would lead to an uncontrolled expansion of the orbit. To counter this, a laser beam with a lower frequency than the atomic transition and which has a non-uniform intensity profile across the radial motion of the ion is used. The modified cyclotron mode is cooled as normal. The Doppler shift brings the laser in to resonance with the atomic transition. In addition, more photons are scattered in the part of the motion where the laser beam intensity is higher. This is arranged such that there is a greater scattering rate in the part of the magnetron motion which moves in parallel to the wave vector of the laser beam. This way the energy of the magnetron mode is increased and therefore the ion becomes localised in the centre of the trap. The radial modes can only be treated using this simple method when they have a relatively large frequency difference and there is a sufficient intensity gradient across the radial orbit. From this point onwards I will abuse the term *cooling* to mean a reduction in the size of an orbit even if this requires that the energy of the magnetron mode is increased.

For a quantitative analysis we will closely follow the arguments in reference [15]. We start with equations 2.5, 2.13a and 2.13b and their time derivatives at time t and t'. This corresponds to immediately before and after an interaction with a photon. Using the assumption that the velocity changes instantaneously but the position does not, we can produce the set of simultaneous equations:

$$Z\cos\left(\omega_z t+\delta_z\right)=Z'\cos\left(\omega_z t'+\delta_z'\right), \tag{3.59a}$$

$$-\omega_z Z\sin\left(\omega_z t+\delta_z\right)+\Delta v_z=-\omega_z Z'\sin\left(\omega_z t'+\delta_z'\right), \tag{3.59b}$$

$$\begin{aligned}R_+\cos\left(\omega_+ t+\delta_+\right)&+R_-\cos\left(\omega_- t+\delta_-\right)\\&=R_+'\cos\left(\omega_+ t'+\delta_+'\right)+R_-'\cos\left(\omega_- t'+\delta_-'\right),\end{aligned} \tag{3.59c}$$

$$\begin{aligned}-\omega_+R_+\sin\left(\omega_+ t+\delta_+\right)&-\omega_-R_-\sin\left(\omega_- t+\delta_-\right)+\Delta v_x\\&=-\omega_+R_+'\sin\left(\omega_+ t'+\delta_+'\right)-\omega_-R_-'\sin\left(\omega_- t'+\delta_-'\right),\end{aligned} \tag{3.59d}$$

$$\begin{aligned}-R_+\sin\left(\omega_+ t+\delta_+\right)&-R_-\sin\left(\omega_- t+\delta_-\right)\\&=-R_+'\sin\left(\omega_+ t'+\delta_+'\right)-R_-'\sin\left(\omega_- t'+\delta_-'\right),\end{aligned} \tag{3.59e}$$

$$\begin{aligned}-\omega_+R_+\cos\left(\omega_+ t+\delta_+\right)&-\omega_-R_-\cos\left(\omega_- t+\delta_-\right)+\Delta v_y\\&=-\omega_+R_+'\cos\left(\omega_+ t'+\delta_+'\right)-\omega_-R_-'\cos\left(\omega_- t'+\delta_-'\right).\end{aligned} \tag{3.59f}$$

Calculating $(3.59\text{a}\times\omega_z)^2+(3.59\text{b})^2$ directly leads to the equation

$$\Delta Z^2=Z'^2-Z^2=\left(\frac{\Delta v_z}{\omega_z}\right)^2-\frac{2\Delta v_z Z}{\omega_z}\sin\left(\omega_z t+\delta_z\right), \tag{3.60}$$

which gives the change in the magnitude of the axial motion for one scattering event. The equations that relate to the radial motion need to be treated slightly more carefully to uncouple the two different modes. Initially, equations 3.59c and 3.59e are multiplied by ω_+ and ω_- in the 4 possible combinations. Then these equations are added or subtracted with equations 3.59d and 3.59f to produce the four simultaneous equations

$$-2\omega_1 R_+\cos\left(\omega_+ t+\delta_+\right)+\Delta v_y=-2\omega_1 R_+'\cos\left(\omega_+ t'+\delta_+'\right), \tag{3.61a}$$

$$2\omega_1 R_-\cos\left(\omega_- t+\delta_-\right)+\Delta v_y=2\omega_1 R_-'\cos\left(\omega_- t'+\delta_-'\right), \tag{3.61b}$$

$$-2\omega_1 R_+\sin\left(\omega_+ t+\delta_+\right)+\Delta v_x=-2\omega_1 R_+'\sin\left(\omega_+ t'+\delta_+'\right), \tag{3.61c}$$

$$2\omega_1 R_-\sin\left(\omega_- t+\delta_-\right)+\Delta v_x=2\omega_1 R_-'\sin\left(\omega_- t'+\delta_-'\right), \tag{3.61d}$$

where $2\omega_1=\omega_+-\omega_-$. Now, calculating $(3.61\text{a})^2+(3.61\text{c})^2$ and $(3.61\text{b})^2+(3.61\text{d})^2$ we find

$$\Delta R_-^2=R_-'^2-R_-^2=\frac{\Delta v_x^2+\Delta v_y^2}{4\omega_1^2}+\frac{R_-}{\omega_1}\left[\Delta v_x\sin\left(\omega_- t+\delta_-\right)+\Delta v_y\cos\left(\omega_- t+\delta_-\right)\right], \tag{3.62}$$

$$\Delta R_+^2=R_+'^2-R_+^2=\frac{\Delta v_x^2+\Delta v_y^2}{4\omega_1^2}-\frac{R_+}{\omega_1}\left[\Delta v_x\sin\left(\omega_+ t+\delta_+\right)+\Delta v_y\cos\left(\omega_+ t+\delta_+\right)\right]. \tag{3.63}$$

We can calculate the change in velocity and energy for a particular scattering event, using simple conservation of energy and momentum equations,

$$\boldsymbol{\Delta}\mathbf{v} = \mathbf{v}' - \mathbf{v} = \frac{\hbar\left(\mathbf{k} - \mathbf{k_s}\right)}{m} \tag{3.64}$$

$$\Delta E = \frac{m}{2}\left(\mathbf{v}'^2 - \mathbf{v}^2\right) = \frac{\hbar^2\left(\mathbf{k} - \mathbf{k_s}\right)^2}{2m} + \hbar\left(\mathbf{k} - \mathbf{k_s}\right)\cdot\mathbf{v}, \tag{3.65}$$

where an atom initially travelling with velocity v is accelerated to velocity v' after absorbing a photon with wave vector $\mathbf{k}$ and emitting a photon with wavevector $\mathbf{k_s}$. When the change in energy per scattering event is split into vector components $i = x, y, z$, we can write equation 3.65 as

$$\Delta E_i = \frac{\hbar^2\left(k_i - k_{si}\right)^2}{2m} + \hbar\left(k_i - k_{si}\right)v_i. \tag{3.66}$$

Averaging over scattering directions we find $\langle\Delta E\rangle_s = 2R + \hbar k\cdot v$ where $R = \left(\hbar k\right)^2/2m$ is the recoil energy. The time averaged power loss (gain) depends on the energy change per scattering event, the cross section and, in the low intensity limit, the photon frequency, $I/\hbar\omega_{\mathrm{L}}$. The cross section depends on the velocity of the atom and the natural linewidth so that

$$\sigma\left(\omega, v\right) = \frac{\sigma_0\left(\gamma/2\right)^2}{\left(\omega_0 + \mathbf{k}\cdot\mathbf{v} + R/\hbar - \omega_{\mathrm{L}}\right)^2 + \left(\gamma/2\right)^2}, \tag{3.67}$$

where ω_{L} and ω_0 are the laser and atomic resonance frequencies respectively and σ_0 is related to the coefficients that were calculated in section 3.1.

To calculate a minimum temperature that can be reached using this method, we can assume that cooling has already taken place so that the transition linewidth is dominated by the spontaneous decay rather than Doppler broadening. In this limit the cross section in equation 3.67 can be simplified. Also, we can ignore the term $R/\hbar$ in the denominator of equation 3.67 which is small compared to the natural linewidth, $R/\hbar\gamma = 1.5\times10^{-3}$ for the 397 nm Doppler cooling transition in $^{40}\mathrm{Ca}^+$. In this case, we can write equation 3.67 as

$$\sigma\left(\omega, v\right) \approx \frac{\sigma_0\left(\gamma/2\right)^2}{\left(\omega_0 - \omega_{\mathrm{L}}\right)^2 + 2\left(\omega_0 - \omega_{\mathrm{L}}\right)\mathbf{k}\cdot\mathbf{v} + \left(\gamma/2\right)^2} \tag{3.68a}$$

$$= \frac{\sigma_0\left(\gamma/2\right)^2}{\left(\omega_0 - \omega_{\mathrm{L}}\right)^2 + \left(\gamma/2\right)^2}\frac{1}{1 + \dfrac{2\left(\omega_0 - \omega_{\mathrm{L}}\right)\mathbf{k}\cdot\mathbf{v}}{\left(\omega_0 - \omega_{\mathrm{L}}\right)^2 + \left(\gamma/2\right)^2}} \tag{3.68b}$$

$$\approx \frac{\sigma_0\left(\gamma/2\right)^2}{\left(\omega_0 - \omega_{\mathrm{L}}\right)^2 + \left(\gamma/2\right)^2}\left[1 - \frac{2\left(\omega_0 - \omega_{\mathrm{L}}\right)\mathbf{k}\cdot\mathbf{v}}{\left(\omega_0 - \omega_{\mathrm{L}}\right)^2 + \left(\gamma/2\right)^2}\right], \tag{3.68c}$$

where only the first order terms of the Taylor expansion, in the final step, have been included. The first term in the parenthesis of equation 3.68c refers to the DC light pressure and the term linearly dependent on velocity term relates to laser cooling (heating), which is maximised at $\omega_0 - \omega_{\mathrm{L}} = \gamma/2$ ($\omega_0 - \omega_{\mathrm{L}} = -\gamma/2$). The rate of energy change, induced by a single laser, averaged over a particular velocity distribution, in vector components is given by

$$\frac{dE_i}{dt} = \frac{I}{\hbar\omega_L}\langle\sigma\left(\omega_{\mathrm{L}}, v\right)\left[\hbar k_i v_i + R\left(f_i + f_{si}\right)\right]\rangle_v, \tag{3.69}$$

where $f_i = \hat{k}_i^2$ and $f_{si} = \int P_s(\hat{k}_s)\hat{k}_{si}^2 d\Omega$ and where the functions $P_s(\hat{k}_s)$ are listed in table 3.2. It can be shown that it is not possible to cool all three modes of motion with a single uniform intensity laser beam [15]. In this treatment I will consider a non-uniform beam, with maximum intensity I_1, incident perpendicular to the magnetic field and another uniform beam, with intensity I_2, parallel to the magnetic field. This is the situation which is used in the experiments later on in this thesis. It is assumed that when the ion is cooled, the amplitude of the motion in the radial plane, is much smaller than the width of the laser beam so that a Gaussian intensity profile

$$I\left(y\right) = \frac{1}{b\sqrt{2\pi}}\exp\left[-\frac{\left(y-a\right)^2}{2b^2}\right] \tag{3.70}$$

can be approximated by the linear function $I\left(y\right) \approx I_0\left(1 + y/y_0\right)$ where $y_0 = b$ at the point of maximum intensity gradient on the Gaussian profile. Figure 3.5 shows how these two functions compare.

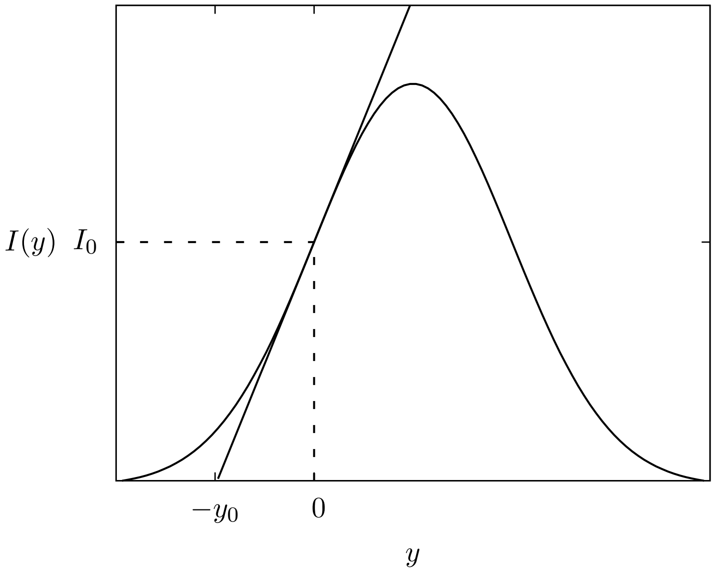

Figure 3.5: Linear approximation to Gaussian beam at the point of maximum gradient.

In this case, the equations describing the evolution of the amplitude of motion can be written as

$$\frac{d\left\langle i^2\right\rangle}{dt} = \frac{I_1}{\hbar\omega_{\mathrm{L1}}}\left\langle\left(1+\frac{y}{y_0}\right)\sigma_1\left(\omega_{\mathrm{L1}},v\right)\Delta i\right\rangle + \frac{I_2}{\hbar\omega_{\mathrm{L2}}}\left\langle\sigma_2\left(\omega_{\mathrm{L2}},v\right)\Delta i\right\rangle, \tag{3.71}$$

where $i = Z, R_+, R_-$ [15]. Using the approximation in equation 3.68 the three rate equations describing the change in amplitude of the three different modes can be written as

$$\frac{d\left\langle Z^2\right\rangle}{dt} = -\frac{2\gamma_{s2}\hbar k_2^2\left(\omega_0-\omega_{\mathrm{L2}}\right)\left\langle Z^2\right\rangle}{m\left[\left(\gamma/2\right)^2+\left(\omega_0-\omega_{\mathrm{L2}}\right)^2\right]} + \frac{\gamma_{s2}\hbar^2 k_2^2\left[1+\left(1+\gamma_{s1}/\gamma_{s2}\right)f_{sz}\right]}{m^2\omega_z^2}, \tag{3.72a}$$

$$\begin{aligned}\frac{d\left\langle R_-^2\right\rangle}{dt} = &-\frac{\gamma_{s1}\hbar k_1\left\langle R_-^2\right\rangle}{2my_0\omega_1} + \frac{\gamma_{s1}\hbar k_1^2\omega_-\left(\omega_0-\omega_{\mathrm{L1}}\right)\left\langle R_-^2\right\rangle}{m\omega_1\left[\left(\gamma/2\right)^2+\left(\omega_0-\omega_{\mathrm{L1}}\right)^2\right]}\\ &+\frac{\gamma_{s1}\hbar^2 k_1^2\left[1+\left(1+\gamma_{s1}/\gamma_{s2}\right)\left(f_{sx}+f_{sy}\right)\right]}{4m^2\omega_1},\end{aligned} \tag{3.72b}$$

$$\begin{aligned}\frac{d\left\langle R_+^2\right\rangle}{dt} = &+\frac{\gamma_{s1}\hbar k_1\left\langle R_+^2\right\rangle}{2my_0\omega_1} - \frac{\gamma_{s1}\hbar k_1^2\omega_-\left(\omega_0-\omega_{\mathrm{L1}}\right)\left\langle R_+^2\right\rangle}{m\omega_1\left[\left(\gamma/2\right)^2+\left(\omega_0-\omega_{\mathrm{L1}}\right)^2\right]}\\ &+\frac{\gamma_{s1}\hbar^2 k_1^2\left[1+\left(1+\gamma_{s1}/\gamma_{s2}\right)\left(f_{sx}+f_{sy}\right)\right]}{4m^2\omega_1}.\end{aligned} \tag{3.72c}$$

To ensure that the lasers cool the radial motion rather than heat, the sum of the first two terms of equations 3.72b and 3.72c must be negative. This limits the value of y_0 within the range

$$\omega_- < \frac{\left(\gamma/2\right)^2+\left(\omega_0-\omega_{\mathrm{L1}}\right)^2}{2k_1 y_0\left(\omega_0-\omega_{\mathrm{L1}}\right)} < \omega_+. \tag{3.73}$$

These limits are plotted alongside trap frequencies in figure 3.6, as a function of the maximum stable trapping voltage. It is clear that y_0 can take a wider range of values and still lead to cooling both the magnetron and cyclotron motions at lower trap voltages. This is directly a consequence of the relatively large frequency difference between the two modes. This difference allows simple velocity selection (Doppler) cooling for the modified cyclotron motion and only a small amount of heating of the magnetron motion. Simultaneously, the intensity gradient can also impart energy to the magnetron mode. This energy transfer reduces the amplitude of the magnetron motion while not having too great a heating effect on the modified cyclotron mode. The cooling limits

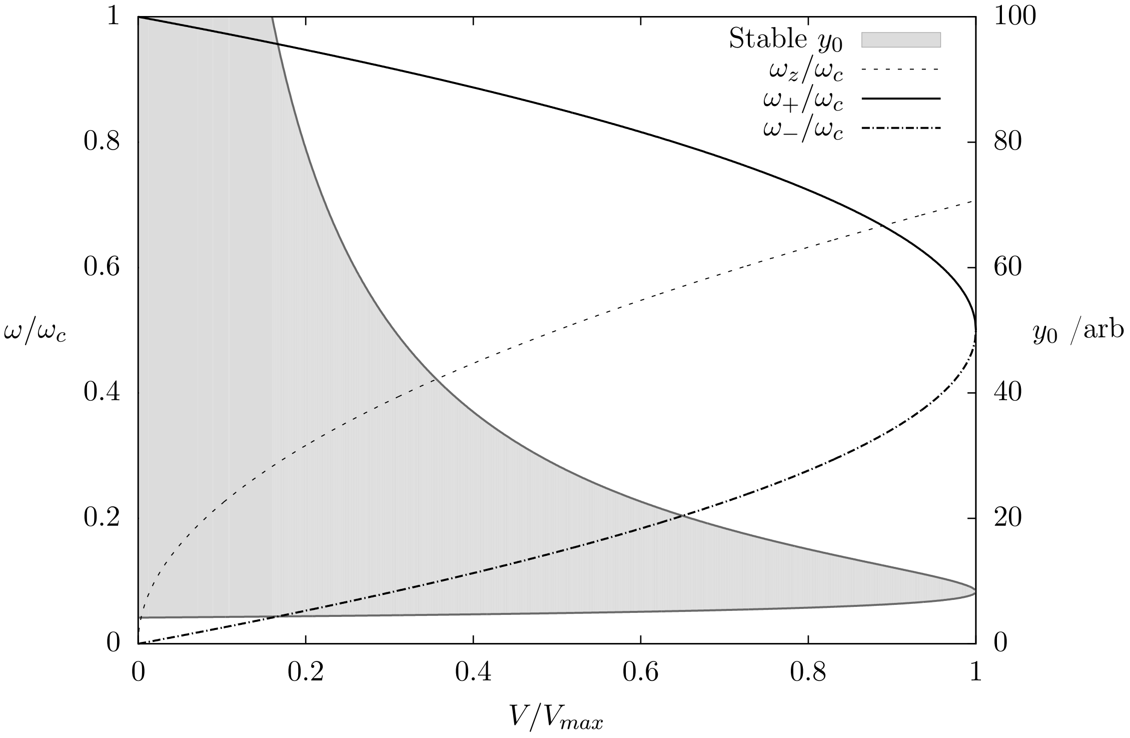

Figure 3.6: Trap frequencies and the range of laser intensity gradients which lead to stable laser cooling as a function of trap bias. The frequencies are in units of ω_c and the laser intensity gradient is calculated at a detuning of $\gamma/2$ at the Ca^+ Doppler cooling wavelength. For $^{40}\mathrm{Ca}^+$ions the optimal intensity gradient as a function of magnetic field is $y_0/|\mathbf{B}| = 3.5\,\mu\mathrm{m\,T}$.

$$\left\langle Z^2\right\rangle = \frac{\hbar\left[(\gamma/2)^2 + (\omega_0-\omega_{\mathrm{L2}})^2\right]\left[1+(1+\gamma_{s1}/\gamma_{s2})f_{sz}\right]}{2m\omega_z^2(\omega_0-\omega_{\mathrm{L2}})}, \tag{3.74a}$$

$$\left\langle R_-^2\right\rangle = \frac{\hbar k_1 y_0\left[1+(1+\gamma_{s2}/\gamma_{s1})(f_{sx}+f_{sy})\right]}{2m\omega_1\left[1-\dfrac{2k_1y_0(\omega_0-\omega_{\mathrm{L1}})\omega_-}{(\gamma/2)^2+(\omega_0-\omega_{\mathrm{L1}})^2}\right]}, \tag{3.74b}$$

$$\left\langle R_+^2\right\rangle = \frac{\hbar k_1 y_0\left[1+(1+\gamma_{s2}/\gamma_{s1})(f_{sx}+f_{sy})\right]}{2m\omega_1\left[\dfrac{k_1y_0(\omega_0-\omega_{\mathrm{L1}})\omega_+}{(\gamma/2)^2+(\omega_0-\omega_{\mathrm{L1}})^2}-1\right]}, \tag{3.74c}$$

can be derived by setting equations 3.72 equal to zero and rearranging them to find the mean squared amplitudes. Setting the detuning to $\gamma/2$ minimises these amplitudes,

$$\left\langle Z^2 \right\rangle_{\min} = \frac{9\hbar\gamma}{10m\omega_z^2}, \tag{3.75a}$$

$$\left\langle R_-^2 \right\rangle_{\min} = \frac{11\hbar\gamma}{20m\omega_1\omega_-\left(\frac{\gamma}{2k_1y_0\omega_-}-1\right)}, \tag{3.75b}$$

$$\left\langle R_+^2 \right\rangle_{\min} = \frac{11\hbar\gamma}{10m\omega_1\omega_+\left(1-\frac{\gamma}{k_1y_0\omega_+}\right)}, \tag{3.75c}$$

where we have assuming that both lasers address the same $|\Delta m| = 1$ transitions, where $f_{sz} = 4/10$ and $f_{sx} = f_{sy} = 3/10$ (this is essential to do laser cooling parallel to the applied magnetic field as we do). Equations 3.75 clearly show that the mode amplitudes are dependent on trap frequencies, which in turn are dependent on the trap bias and the magnetic field. Figure 3.7 shows the amplitudes of the three different modes for typical trap and laser parameters as a function of the maximum stable trap bias. Using equations 2.29

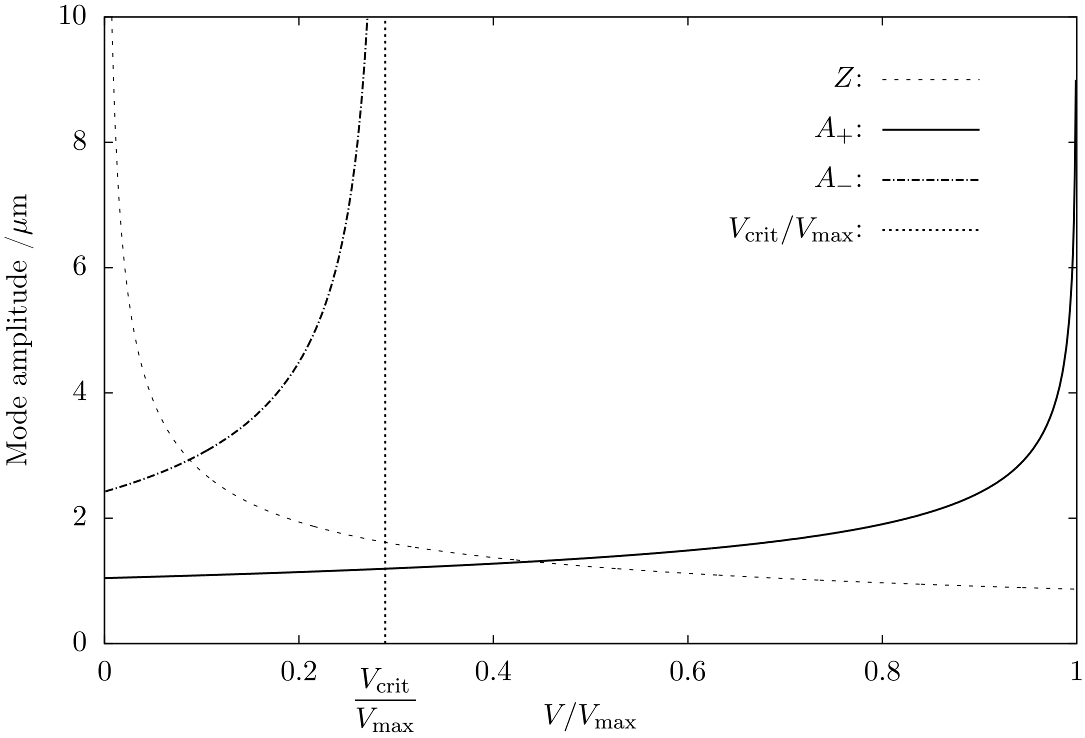

Figure 3.7: The absolute amplitude of motion for the three different modes at the Doppler cooling limit and the critical voltage where the magnetron mode becomes unstable, i.e. heating from laser light detuned to a lower frequency than the atomic resonance is greater than cooling due to the intensity gradient. The plot is for 397 nm laser cooling on a $^{40}\text{Ca}^+$ ion, parameters assumed are: $|\mathbf{B}| = 1.85\,\text{T}$ and $y_0 = 12\,\mu\text{m}$.

we can determine the average occupation numbers for the different modes at the Doppler cooling limit for the trapping parameters given in figure 3.7. These limits are plotted as a function of trap voltage in figure 3.8. We can calculate the kinetic energy in each of these modes by using equations 2.17. The kinetic energy in the three cases is

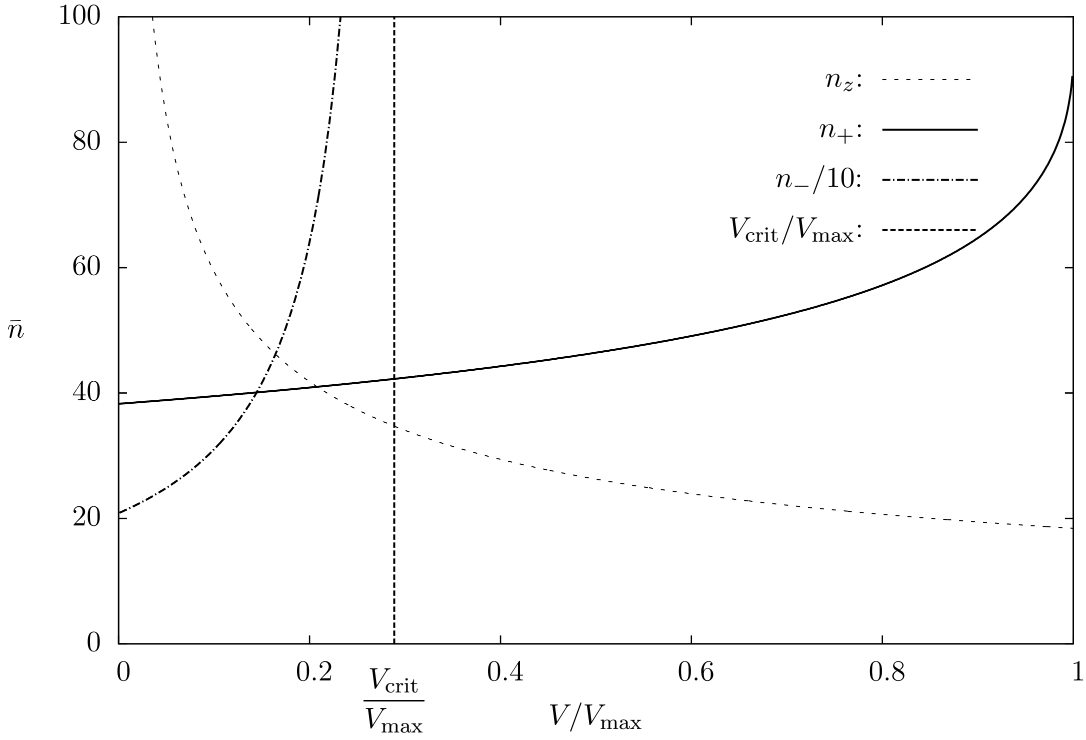

Figure 3.8: The value of $\bar{n}$ as a function of maximum stable trap bias. Assumed trap parameters are the same as figure 3.7.

$$\langle \mathrm{KE}_z \rangle = \frac{9\hbar\gamma}{40}, \tag{3.76a}$$

$$\langle \mathrm{KE}_- \rangle = \frac{11\hbar\gamma\omega_-}{40\omega_1\left(\dfrac{\gamma}{2k_1 y_0 \omega_-} - 1\right)}, \tag{3.76b}$$

$$\langle \mathrm{KE}_+ \rangle = \frac{11\hbar\gamma\omega_+}{20\omega_1\left(1 - \dfrac{\gamma}{k_1 y_0 \omega_+}\right)}. \tag{3.76c}$$

These modes show different behaviour: the kinetic energy of the axial motion is a constant and not affected by trap bias whereas the other modes increase their kinetic energy as a function of trap voltage. The magnetron kinetic energy is initially very small but still becomes unstable for a particular value of y_0. Close to this trap potential the kinetic energy becomes very large because the denominator in equation 3.76b approaches zero.

3.4.2 Resolved sideband cooling

The Doppler cooling limit derived in the previous section is not fundamental and the kinetic energy of the ion can be reduced further. To date, two methods have been used to cool a trapped ion the ground state of motion: resolved sideband cooling either via direct optical excitation [16] or Raman transitions [17] and Stark shift tuned electromagnetic induced transparency cooling [34].

Once an ion has been cooled to the ground state of motion, the population distribution is described by a number state (specifically $n = 0$). An ion in this state will display full contrast Rabi oscillations. Ground state cooled ions are a useful resource for many applications:

1. Arbitrary superpositions of quantum states.
2. A starting point for complicated quantum computations and simulations.
3. Reduced Doppler shifts for atomic clocks & high resolution spectroscopy.
4. Potentially, higher resolution mass measurements.

The coherent motion of a trapped ion modulates the atomic spectrum. This frequency modulation produces sidebands on the carrier transition; in the resolved-sideband regime where $\gamma < \omega$, these sidebands can be optically resolved. In a Penning trap the energy levels in figure 2.5 are superimposed on the internal states. To simplify the situation, we only consider a pseudo-two-level atom (ion) modulated by the axial motion. A method of cooling that exploits these ideas was initially investigated for a Penning trap in reference [35]. By selectively stimulating a sideband with frequency lower than the transition carrier,

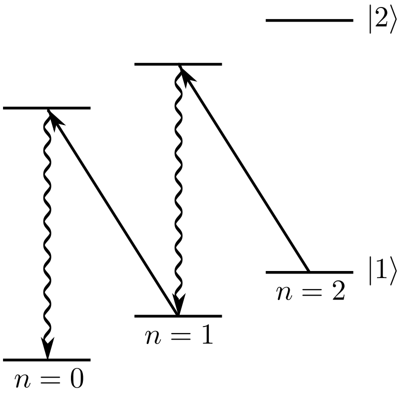

Figure 3.9: Axial motional states superimposed on two internal energy levels, $|1\rangle$ and $|2\rangle$. The solid arrows represent stimulation on the red sideband followed by decay on carrier transitions, drawn with wavy arrows.

the motional state of the ion is reduced. Figure 3.9 shows a schematic diagram of how this proceedure could be used to reduce the energy of the axial motion of an ion in a Penning trap. In the Lamb-Dicke regime, defined by $\eta(2\bar{n}+1) < 1$, the decay happens predominantly on the carrier transition without a change in occupation number. However, it is clear from figure 3.4, that it is very difficult to achieve this regime in a Penning trap by merely Doppler cooling without a low mass ion e.g. Be^+, a high magnetic field $>10\,\mathrm{T}$ and a beam profile with a region of large intensity gradient (this could be either a tight focus or higher order Laguerre-Gaussian beam) with $y_0 \sim 1\,\mu m$. This is challenging to achieve given the restricted optical access in Penning traps.

Theoretical papers have proposed efficient sideband cooling from outside the Lamb-Dicke regime [36]. This method has not been demonstrated experimentally to this date. However, a simpler technique where the laser is initially tuned to the second red sideband, on average removing two quanta of energy per scattering event, as a pre-cooling step to reach the Lamb-Dicke regime, has been shown to work. This step was followed by the standard sideband cooling procedure, to reach the ground motional state in reference [37].

To calculate the cooling rate for this laser cooling method, we need to treat the motion of the ion quantum mechanically. The analysis in section we closely follow the arguments in reference [35]. We start by writing the down the rate equation

$$\frac{d\left\langle n_i\right\rangle}{dt} = \frac{I_m}{\hbar\omega_m}\sum_{n_{i,j}} P\left(n_{i,l}\right)\sigma\left(n_{i,l}\to n_{i,f}\right)\left(n_{i,f}-n_{i,l}\right), \tag{3.77}$$

where $i = +,-,z$, $P\left(n_{i,l}\right)$ is the initial population distribution, $n_{i,j}$ and $n_{i,f}$ are the intermediate and final vibrational level respectively, and $\sigma\left(n_{i,l}\to n_{i,f}\right)$ is the cross section from $n_{i,l}$ to $n_{i,f}$ for laser m. The cross section is now written as

$$\sigma\left(n_{i,l}\to n_{i,f}\right) =$$
$$\frac{\sigma_0\gamma^2}{4}\int\left|\sum_{n_{i,j}}\frac{\left\langle n_{i,f}\left|\exp\left(-\imath\mathbf{k_s}\cdot\mathbf{r}\right)\right|n_{i,j}\right\rangle\left\langle n_{i,j}\left|\exp\left(\imath\mathbf{k_m}\cdot\mathbf{r}\right)\right|n_{i,l}\right\rangle}{\omega_0-\omega_m+\left(\omega_{i,j}-\omega_{i,l}\right)-\imath\gamma/2}\right|^2 P_s\left(\hat{\mathbf{k}}_\mathbf{s}\right)d\Omega. \tag{3.78}$$

It can be shown that equation 3.78 can be written as

$$\frac{d\left\langle n_i\right\rangle}{dt} = \frac{I_m\sigma_0}{\hbar\omega_0}\int I'd\omega\sum_{n_{i,l},n_{i,j}} P\left(n_{i,l}\right)\frac{\left[\beta_i f_{si}+n_{i,j}-n_{i,l}\right]\left|\left\langle n_{i,j}\left|\exp\left(\imath\mathbf{k_m}\cdot\mathbf{r}\right)\right|n_{i,l}\right\rangle\right|^2}{1+\left\{\frac{2}{\gamma}\left[\omega_0-\omega_m+\left(\omega_{i,j}-\omega_{i,l}\right)\right]\right\}}, \tag{3.79}$$

where

$$\beta_i = \begin{cases} (kr_0)^2/4 & \text{if } i = c \text{ or } m \\ (kz_0)^2 & \text{if } i = z, \end{cases} \qquad f_{si} = \begin{cases} f_{sx} + f_{sy} & \text{if } i = c \text{ or } m \\ f_{sz} & \text{if } i = z \end{cases} \qquad [35]. \tag{3.80}$$

The physical meanings of the terms in equation 3.79 are explained in table 3.4. In general solving equation 3.79 can be quite complicated, however, if somehow the atom has already been cooled to the Lamb-Dicke regime, where only transitions on the carrier and first order sidebands need to be considered, the absorption and decay rates in equation 3.52 can be well approximated by simple polynomial functions. In this case, the Rabi frequencies on the carrier, first red and first blue sidebands are proportional to $1 - \eta^2(n+1)/2$, $\eta\sqrt{n}$ and $\eta\sqrt{n+1}$ respectively. These Rabi frequencies can then be used to calculate equation 3.55.

$I_m\sigma_0/\hbar\omega_0$	The on-resonance scattering rate.
$\int I' d\omega$	The integral takes into account the spectral purity of the laser relative to the transition linewidth. The integral is normalised to unity.
$\beta_i f_{si}$	The photon recoil frequency relative to the trap frequency, this is the change in occupation number which occurs on decay.
$n_{i,j} - n_{i,l}$	The change in occupation number which occurs in stimulated excitation. For cooling, this term must be less than zero.
$\left\langle n_{i,j} \left\| \exp\left(\imath \mathbf{k_m} \cdot \mathbf{r}\right) \right\| n_{i,l} \right\rangle$	The Rabi frequency between levels $n_{i,j}$ and $n_{i,l}$.
$\frac{2}{\gamma}\left[\omega_0 - \omega_m + \left(\omega_{i,j} - \omega_{i,l}\right)\right]$	Takes into account the detuning from the resonance of a sideband.

Table 3.4: Physical meanings of terms in equation 3.79.

If an ion is placed in both the ground electronic and motional states there is no level to which it can be excited with a laser tuned to the first red sideband. Hence, the excitation probability at this laser frequency tends to zero as $\bar{n}$ approaches zero. In this regime, the mean vibrational level can be directly calculated from

$$\bar{n} = \frac{P_e^{\mathrm{RSB}}}{P_e^{\mathrm{BSB}} - P_e^{\mathrm{RSB}}}, \tag{3.81}$$

where P_e^{RSB} and P_e^{RSB} are the excitation probability of the first red and blue sidebands respectively at saturation laser intensity for the carrier transition.

The bandwidth of resolved sideband cooling described so far is limited by the spontaneous decay rate of the transition, around 1 Hz using the 729 nm electric quadrupole transition in calcium. The linewidth of transition may be artificially broadened to $\tilde{\gamma}$, to increase the cooling rate, by coupling to a level with an electric dipole allowed transition back to the ground state. This decay will have a different recoil energy. Using this method of cooling the minimum obtainable occupation number is given by

$$\bar{n}_{\text{min}} \approx \left(\frac{\tilde{\gamma}}{2\omega}\right)^2 \left[\left(\frac{\eta_{\text{decay}}}{\eta_{\text{absorb}}}\right)^2 + \frac{1}{4}\right], \tag{3.82}$$

where care has to be taken to understand that the Lamb-Dicke parameter for the absorbed and emitted photons are different [38].

When a third electronic level is used to increase the linewidth of the weak transition in a 2 photon excitation scheme, as shown in figure 3.10, the cooling rate can be increased [39].

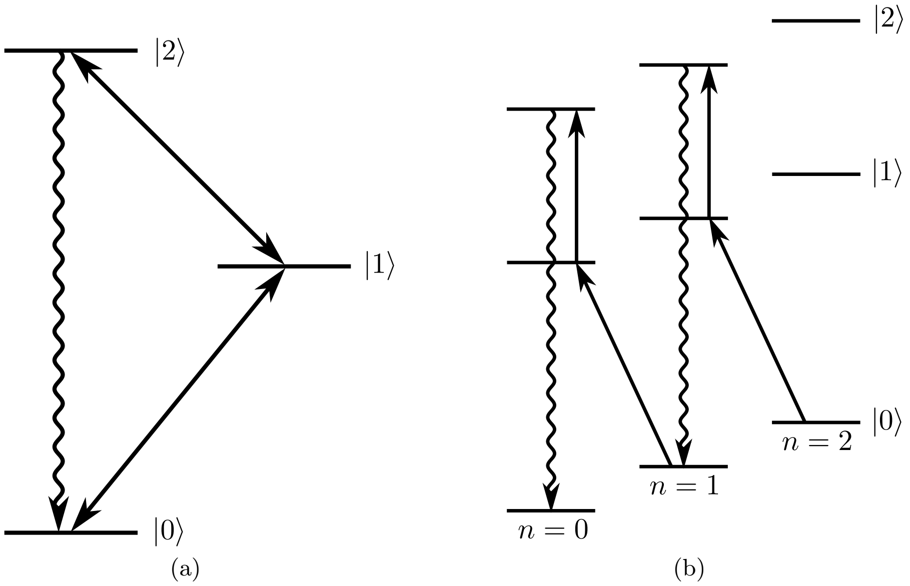

Figure 3.10: Left: By coupling the long lived state $|1\rangle$ to another level $|2\rangle$, with a fast decay back to the ground state, below saturation, the effective decay rate of the narrow linewidth transition can be increased. Right: figure showing the internal and external energy levels of the three states in the scheme. We assume that the vibrational level does not change on average when exciting between internal states $|1\rangle \leftrightarrow |2\rangle$.

Reference [39] suggests the laser used to stimulate the $|1\rangle \leftrightarrow |2\rangle$ broadening transition in $^{40}\text{Ca}^+$ ions should be driven at approximately 1/5 times saturation intensity. The detuning of this laser is not crucial and setting it to $\delta_{12} \approx 10\gamma_{20}$, where δ_{ij} and γ_{ij} are the detuning and spontaneous decay rate from level $|i\rangle$ to $|j\rangle$ respectively, is a good compromise. This is still effectively a two level system because the decay from $|2\rangle$ is extremely fast compared to the spontaneous decay rate γ_{10}. For this pseudo two level system the effective decay rate,

$$\tilde{\gamma} = \frac{\Omega_{12}^2/2}{\left[\left(\gamma_{20} + \gamma_{21}\right)/2\right]^2 + \delta_{12}^2}\gamma_{20}, \tag{3.83}$$

depends quadratically on the Rabi frequency of the transition used to increase the spontaneous decay rate and linearly on the decay rate of state $|2\rangle$ to the ground state. A simpler, more intuitive way of thinking of the combined linewidth is $1/\tau$ where τ is the time required for a single closed cooling cycle. However, it is important to remember that when broadening the weak transition, the resolved sideband condition, $\tilde{\gamma} < \omega$, must remain true to perform sideband cooling.

It is clear from figure 3.8 that resolved sideband cooling the magnetron motion is always going to tricky, not only because $\bar{n}$ at the Doppler cooling limit is very high but also because the oscillation frequency is so low that a compromise must be made between broadening the weak transition to increase the cooling rate and still resolving motional sidebands.

Chapter 4

Experimental Setup

4.1 Calcium II level structure

The atomic energy level structure of $^{40}\mathrm{Ca}^{+}$ ions can be seen in figure 4.1. All the transitions marked in figure 4.1 are dipole allowed transitions except for the 729 nm $\mathrm{S}_{1/2} \leftrightarrow \mathrm{D}_{5/2}$ transition, which is electric quadrupole allowed, with a natural lifetime of approximately 1 s [40].

The two $\mathrm{S}_{1/2} \leftrightarrow \mathrm{P}_{1/2}$ transitions are used for Doppler cooling. On approximately $1/15^{\mathrm{th}}$ of occasions the ion decays from the $\mathrm{P}_{1/2}$ state to the $\mathrm{D}_{3/2}$ state [28]. This state needs to be repumped to maintain a closed cooling cycle. In a Penning trap the Zeeman splitting of the $\mathrm{P}_{1/2} \leftrightarrow \mathrm{D}_{3/2}$ transitions is much larger than the natural and laser linewidths. Therefore, to repump the $\mathrm{D}_{3/2}$ levels we phase modulate the repumping laser field with an electroptic modulator (EOM); see section 4.4.1 for details.

These laser beams are sent via polarisation maintaining (PM) optical fibres to the trap. Fluorescence from the ions in the trap is collected, imaged onto multimode optical fibres and detected on photomultiplier tubes, or an amplified camera.

4.1.1 J quantum number magnetic mixing

Spin and orbital angular momentum couple together in the absence of an external field to form J, the total angular momentum. This interaction can be thought of as being due to the magnetic field caused by the nucleus and electronic core orbiting the valence electron, interacting with the electron magnetic moment, in the frame of reference where

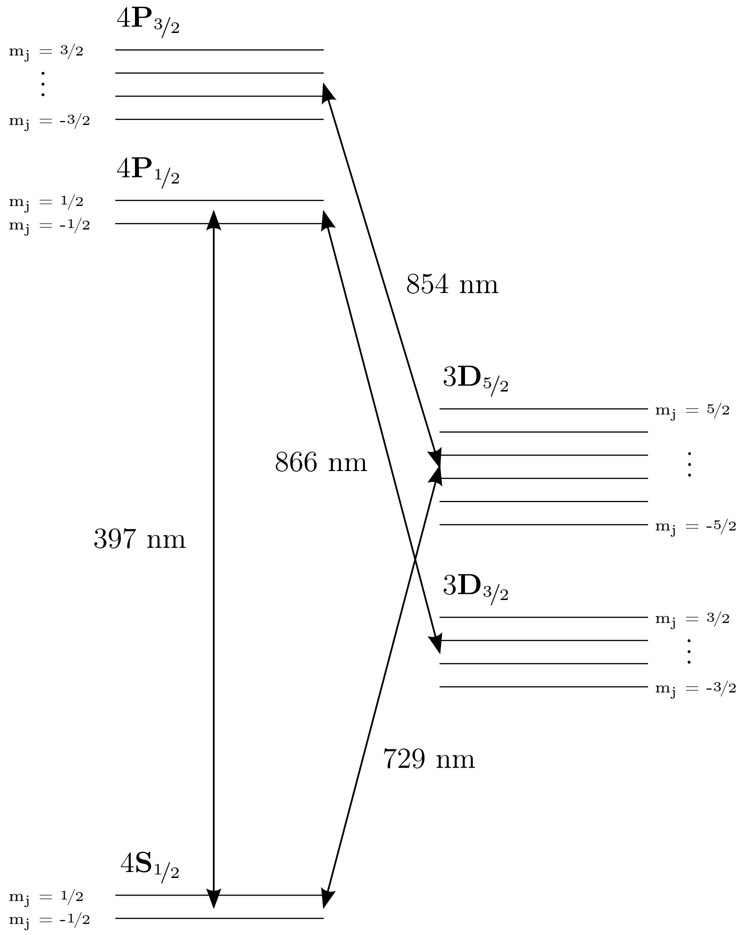

Figure 4.1: Relevant Zeeman split energy levels for $^{40}\mathrm{Ca}^{+}$ ions, in the low magnetic field regime (not to scale).

the electron is stationary. The Hamiltonian has the form

$$\hat{H} = f\left(r\right)\left(\hat{J}^2 - \hat{L}^2 - \hat{S}^2\right), \tag{4.1}$$

where $f(r)$ depends on the principal quantum number and several other factors. Here the good quantum numbers to use are J, L, S & m_J.

Applying a small magnetic field splits each J level linearly into $2J+1$ states, with energy proportional to m_J, so that

$$\Delta E_{Zeeman} = \mu_B g_J m_J B, \tag{4.2}$$

where g_J is the Landé g-factor and μ_B is the Bohr magnetron.

In calcium the fine structure splitting between the metastable D-states is approximately 1.1 THz, whereas the Zeeman splitting is of the order of 10 GHz T^{-1}. It is clear that at a trapping field of 1.85 T, we are in a regime where the spin-orbit coupling dominates.

It is possible to modify the eigenstates to take account of the applied magnetic field [41]. In the weak applied field regime, the obvious basis to use is J & m_J. The effect of the magnetic field is to mix levels with the same L and m_J [41], i.e. the $\mathrm{P}_{1/2,\pm 1/2}$ and $\mathrm{P}_{3/2,\pm 1/2}$ states mix and $\mathrm{D}_{3/2,-3/2\ldots 3/2}$ and $\mathrm{D}_{5/2,-3/2\ldots 3/2}$ states also mix together. The magnetically mixed state makes some of the highly forbidden $\mathrm{P}_{1/2} \leftrightarrow \mathrm{D}_{5/2}$ transitions allowed, with a small electric dipole amplitude.

This process can be seen experimentally during Doppler cooling. When the ion is excited to the $\mathrm{P}_{1/2}$ level instead of always decaying to the $\mathrm{S}_{1/2}$ or $\mathrm{D}_{3/2}$ levels, the ion occasionally decays to the $\mathrm{D}_{5/2}$ level which removes it from the standard cooling cycle. The rate at which this decay happens can be calculated with first order perturbation theory. It can be shown that

$$\frac{\gamma\left(\mathrm{P}_{1/2} \rightarrow \mathrm{D}_{5/2}\right)}{\gamma\left(\mathrm{P}_{1/2} \rightarrow \mathrm{S}_{1/2}\right)} \approx 4.2 \times 10^{-7}\,\mathrm{T}^{-2}, \tag{4.3}$$

where $\gamma\left(\mathrm{P}_{1/2} \rightarrow \mathrm{D}_{5/2}\right)$ and $\gamma\left(\mathrm{P}_{1/2} \rightarrow \mathrm{S}_{1/2}\right)$ are partial spontaneous decay rates from the $\mathrm{P}_{1/2}$ state [42]. In a 1.85 T magnetic field approximately 7.0×10^5 photons will be emitted on average before shelving to the metastable state. On average an ion will only scatter photons for 54 ms before shelving to the $\mathrm{D}_{5/2}$ level when the cooling transition is saturated.

In order to remove this problem, we apply a laser at 854 nm to drive the $\mathrm{D}_{5/2} \leftrightarrow \mathrm{P}_{3/2}$ transitions and to return the ion to the cooling cycle. The required repumping rate is much slower than all the other Doppler cooling transitions, so only a very small amount of power is needed in this laser, or alternatively, the laser can be detuned by a few hundred megahertz and still remain useful.

4.2 Diode Lasers

The two lasers we use for main 397 nm laser cooling transitions are GaN laser diodes[1]. They are used to stimulate the $\mathrm{S}_{1/2,1/2} \leftrightarrow \mathrm{P}_{1/2,-1/2}$ and $\mathrm{S}_{1/2,1/2} \leftrightarrow \mathrm{P}_{1/2,-1/2}$ transitions which have a 69 GHz frequency splitting in a 1.85 T magnetic field. They are housed in TuiOptic (now called Toptica) commercial extended cavity diode laser (ECDL) systems with Littrow feedback. These lasers are locked to low finesse tunable cavities via feedback to the diode current and a piezoelectric element on to which the diffraction grating is mounted. These cavities are in turn locked to a reference HeNe laser with a home-made spectrum analyser to produce a pair of 2–3 MHz linewidth lasers over several hours.

---

[1] NDV4814T laser diode from Nichia Corporation.

The light from these lasers that is not used for frequency stabilisation is then double passed through acousto-optic modulators (AOMs) to allow high speed switching with extinction >36 dB. The laser beams are then combined on a 50/50 non-polarising beam splitter and sent, via polarisation maintaining (PM) optical fibres, to the optical breadboard on which the trap rests. See section 4.6 for details.

The repumping lasers at 866 nm and 854 nm and the narrow linewidth spectroscopy laser at 729 nm are home made ECDL setups. The design of these are all based around a commercial mirror mount with a piezo stack and ruled diffraction grating mounted 1.5–2 cm from the laser diode. The angle of the grating is set to send the -1 diffraction order back into the laser. A schematic design of these laser heads is shown in figure 4.2. Choosing the blaze angle of the grating is a trade off between power out of the laser and the fraction of light sent back to the the laser to stabilise its frequency. Our lasers use different feedback proportions but we found in general that the anti-reflection coated IR diodes required less feedback (15 %–20 %) to lase single mode compared to standard laser diodes which required about 30 % feedback.

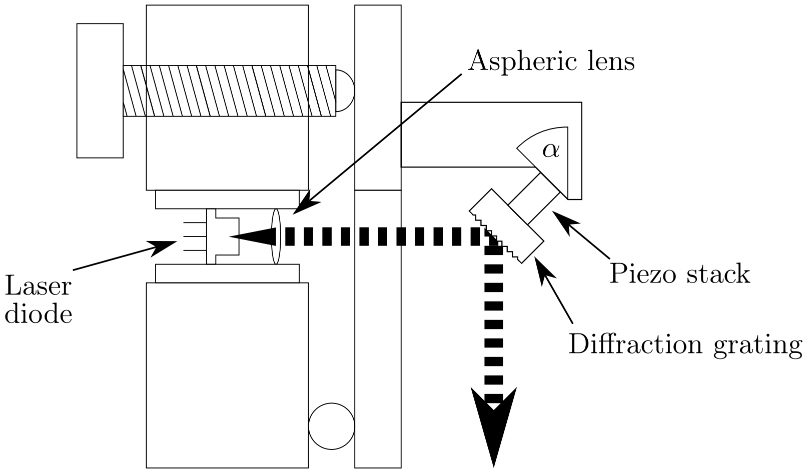

Figure 4.2: A schematic diagram of the ECDL used for the repumping lasers and narrow linewidth 729 nm spectroscopy laser. The design is based around a commercial mirror mount with laser diode and aspheric collimating lenses in a threaded tube. The diffraction angle is tuned so that $\sin\alpha = \lambda/\left(2d\right)$ where d is the diffraction grating line spacing and λ is the laser wavelength.

4.3 Laser Locking

A number of different locking schemes are used for the various lasers employed in the experiment. This section covers the background required to understand these systems. Common feedback mechanisms in ECDLs are:

- To the piezoelectric element on which the diffraction grating is mounted.
- Directly to the laser current.
- To an external acousto-optic (AOM) or electro-optic (EOM) modulator.

Feedback to the piezo allows large frequency correction although it usually has a maximum bandwidth of about 1 kHz, limited by the mechanical resonance and capacitance of the system. Feedback to the laser diode current can occur on significantly shorter time-scales; however in this case, the servo electronics have to be designed carefully not to introduce external noise. Feedback to the laser current has two effects: at lower frequencies, there is a thermal effect which changes the material refractive index and has a negative df/dI coefficient. However, at times shorter than around 1 μs this process becomes less important and another effect related to the carriers in the diode with a positive df/dI coefficient becomes dominant [43]. These two competing mechanisms with their associated phase responses make it difficult to design and build a servo system with a bandwidth higher than a few megahertz. To use an acousto-optic or electro-optic modulator the carrier RF frequency is modulated by the feedback signal. Bandwidth limits on AOMs, usually around 1 MHz, are simply determined by the speed of sound in the crystal. Alternatively, an external EOM has the highest possible modulation bandwidth of all the methods discussed here and is only limited by the capacitance of the crystal. Modulators exist that have extremely wide bandwidths. For example, in section 4.4.1 I will discuss using an EOM with 20 GHz bandwidth which could also be used inside a feedback loop.

4.3.1 Pound-Drever-Hall lock theory

The Pound-Drever-Hall (PDH) locking scheme between a laser and an optical cavity allows high bandwidth feedback. The laser is coupled to the cavity and the reflected light is detected on a photodiode. The PDH locking technique compares the light leaking out from the cavity and the light that is promptly reflected from the input coupling mirror. This produces clear benefits over the side-of-fringe technique [43]. The side-of-fringe technique operates by stabilising the power transmitted through a cavity to some set point; usually half the maximum transmission. The error signal in this case forms an odd function without requiring any external electronics, making it much easier to set up, although with some limitations. Two of the most obvious benefits of a PDH lock compared to a side-of-fringe scheme are:

1. The bandwidth of the lock can be higher than the linewidth of the cavity.
2. The error signal is insensitive to laser amplitude noise to first order.

When a laser is coupled to a Fabry-Perot cavity on resonance, there is a dip in the intensity of the reflected signal. If the laser shifts frequency the amount of reflected light increases but there is no discrimination between a positive or negative frequency shift. To produce an odd function which has a zero point at the cavity resonance, the laser is modulated and the reflected sidebands and carrier are mixed on a photodiode where they interfere to produce an error signal. The error signal is then amplified in a *loop filter* and fed back to the laser. The design of the loop filter and reduction of external noise sources is often where the experimental skill is required. A schematic diagram of a PDH locking system for a laser diode is shown in figure 4.3.

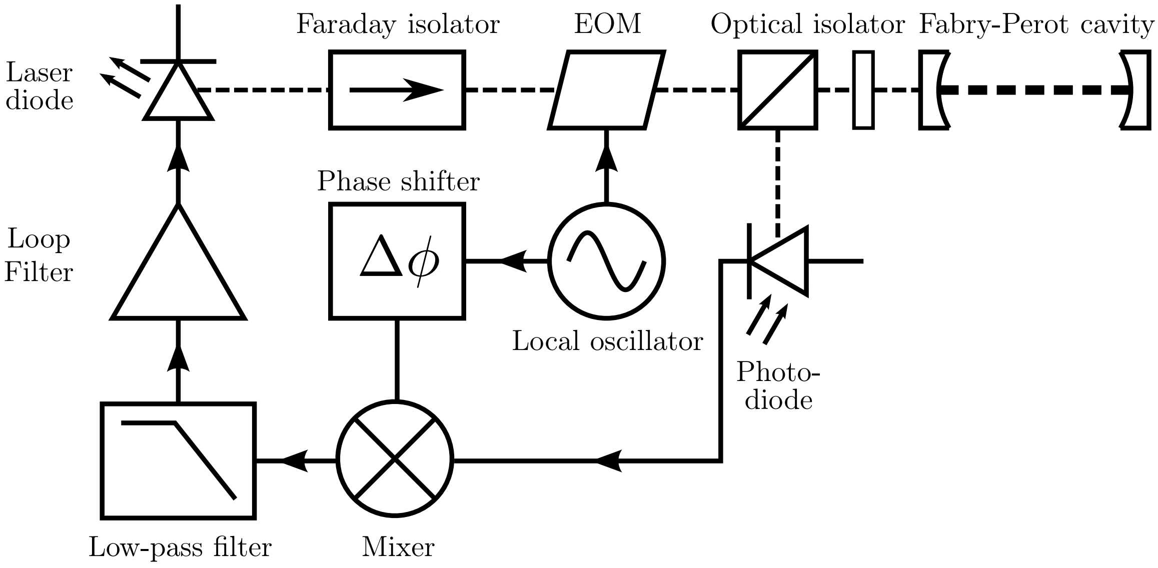

Figure 4.3: Key components of a laser diode PDH locking scheme. Here the phase modulation is imposed on the light using an EOM but sidebands could also be produced by modulating the laser diode current directly.

For a quantitative description, we follow the method in reference [44]. The first step is to phase modulate the laser beam such that the light incident on the cavity can be written as

$$E_{\text{inc}} = E_0 e^{\imath[\omega t + \beta \sin(\Omega t)]} \tag{4.4}$$

$$= E_0 \left[J_0(\beta) e^{\imath\omega t} + J_1(\beta) e^{\imath(\omega+\Omega)t} - J_1(\beta) e^{\imath(\omega-\Omega)t} \right], \tag{4.5}$$

where the sinusoidally varying phase has been expanded in terms of Bessel functions with modulation index β and frequency Ω. The modulation index should be kept low so that $J_0 + 2J_1 \simeq 1$. We now drop the modulation index from the equations but it is implied. For a symmetric, lossless, Fabry-Perot cavity the reflected light can be calculated from $E_{\text{ref}} =$

$F(\omega)\, E_{\text{inc}}$ where the incident light is multiplied by the frequency dependent reflection coefficient

$$F(\omega) = \frac{r\left(e^{\imath\omega/\omega_{\text{FSR}}} - 1\right)}{1 - r^2 e^{\imath\omega/\omega_{\text{FSR}}}}, \tag{4.6}$$

r is the reflection amplitude of one mirror and $\omega/\omega_{\text{FSR}}$ is the optical phase which is an integer multiple of 2π at resonance. The amplitude of the reflected light can be written as

$$E_{\text{ref}} = E_0 \left[F(\omega)\, J_0 e^{\imath\omega t} + F(\omega+\Omega)\, J_1 e^{\imath(\omega+\Omega)t} - F(\omega-\Omega)\, J_1 e^{\imath(\omega-\Omega)t}\right]. \tag{4.7}$$

The photodiode only detects the reflected power, not the amplitude, so we should calculate $P_{\text{ref}} = |E_{\text{ref}}|^2$. Using Euler's formula and the identities $(x+\imath y) + (x+\imath y)^* = 2\Re\{x+\imath y\}$ and $(x+\imath y) - (x+\imath y)^* = 2\Im\{x+\imath y\}$ we can write

$$\begin{aligned} P_{\text{ref}} =& P_C |F(\omega)|^2 + P_S \left\{|F(\omega+\Omega)|^2 + |F(\omega+\Omega)|^2\right\} \\ &+ 2\sqrt{P_C P_S}\left\{\Re\left[F(\omega)\, F^*(\omega+\Omega) - F^*(\omega)\, F(\omega-\Omega)\right]\cos\Omega t \right. \\ &\left. + \Im\left[F(\omega)\, F^*(\omega+\Omega) - F^*(\omega)\, F(\omega-\Omega)\right]\sin\Omega t\right\} \\ &+ 2\Omega \text{ terms}, \end{aligned} \tag{4.8}$$

where P_C and P_S is the power in the carrier and first order sidebands. We are only interested in the second and third terms of 4.8 because they contain information about the mixed carrier and sidebands. The DC and 2Ω terms can be removed by AC coupling the photodiode and putting a low pass filter in series with the signal respectively.

Which of the remaining terms is dominant depends on the size of the modulation frequency relative to the cavity bandwidth. In the PDH scheme, the sidebands are almost completely reflected, i.e.

$$F(\omega+\Omega) \approx F(\omega-\Omega) \approx -1. \tag{4.9}$$

Then the term inside the square brackets in 4.8 can be written as

$$\begin{aligned} F(\omega)\, F^*(\omega+\Omega) - F^*(\omega)\, F(\omega-\Omega) \approx& -\left[F(\omega) - F^*(\omega)\right] \\ =& -\imath 2\Im\left[F(\omega)\right]. \end{aligned} \tag{4.10}$$

Only the sin term remains in 4.8 after this substitution. By adjusting the phase of signal and multiplying it by the modulation on a mixer, the error signal,

$$\epsilon = -2\sqrt{P_C P_S}\,\Im\left[F(\omega)\, F^*(\omega+\Omega) - F^*(\omega)\, F(\omega-\Omega)\right], \tag{4.11}$$

can be extracted. Figure 4.4 shows an example error signal. Within the cavity linewidth, the error signal is approximately a linear function proportional to the displacement from resonance. However, the capture range (the range over which the signal remains positive to the right of the central feature or remains negative to the left) extends all the way to the sideband resonance. Fundamentally, the laser locking bandwidth is limited to the sideband frequency. However, as this can be made arbitrarily large using an EOM, the limiting factors are usually the feedback mechanism and loop filter electronics which amplifies the error signal. We use a PDH lock to reduce the linewidth of the 729 nm laser used to interrogate the quadrupole $S_{1/2} \leftrightarrow D_{5/2}$ transitions. Section 4.5 describes technical details about this locking system.

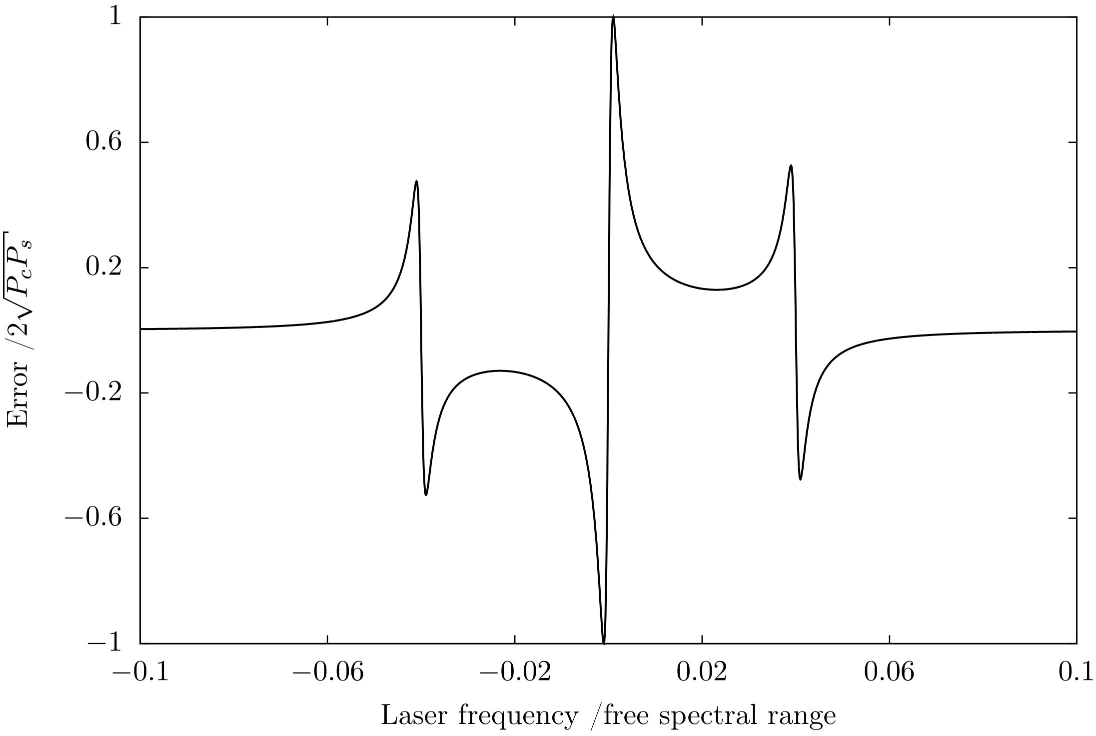

Figure 4.4: Calculated PDH error signal as a laser is scanned around resonance for a cavity finesse of 1000 and a laser modulation of approximately 40 cavity linewidths.

4.3.2 Dither lock

If the cavity used for laser locking has a broad resonance relative to the modulation frequency the features in figure 4.4 at the sideband resonances are no longer distinct. The name of the laser lock in this regime is called a dither lock. Hence, in a dither lock the approximation in equation 4.9 no longer holds true. In this regime we can approximate the reflection coefficients at the sidebands as,

$$F(\omega - \Omega) \approx F(\omega) - \frac{dF(\omega)}{d\omega}\Omega. \tag{4.12}$$

Hence the term

$$F(\omega)F^*(\omega + \Omega) - F^*(\omega)F(\omega - \Omega) \approx 2\Omega\Re\left\{F(\omega)\frac{dF^*(\omega)}{d\omega}\right\} \tag{4.13}$$

only contains real components. The phase of the signal must be modified so that a cosine modulation appears at the mixer and the error signal

$$\epsilon \approx 2\sqrt{P_C P_S}\frac{d|F(\omega)|^2}{d\omega}\Omega \tag{4.14}$$

is demodulated, amplified through the loop filter and fed back to the laser.

4.3.3 Doppler cooling lasers dither lock

The two 397 nm Doppler cooling lasers are dither locked to two different re-entrant design tunable cavities with Zerodur spacers. The cavities are described in more detail in reference [45]. However, in brief, they have finesses of approximately 40 and 60, and a 1.5 GHz free spectral range. The cavities are housed inside a large vacuum chamber with float glass windows at a pressure less than 10^{-1} mbar. The injection current to the lasers is directly modulated to produce sidebands approximately 10 MHz from the carrier. The optical and electronic setup is shown in figure 4.5.

The error signal is amplified and fed back to laser current using a loop filter similar to the circuit described in reference [43]. In order that the laser does not hop to another longitudinal laser mode with a large DC current offset, the error signal is digitally integrated and fed back to the piezo as well. The microcontroller controlling feedback to the piezo also has an input from the transmission of the locking cavities. This ensures that if the laser becomes unlocked or the beam is blocked, the piezo is not suddenly pushed to a voltage rail.

The bandwidth of this lock is 0.5–1 MHz, easily removing any acoustic noise that is present. However, higher frequency noise from the lock broadens the short term linewidth of each laser to approximately 2 MHz. This is equivalent to locking to approximately $1/20^{th}$ of the cavity linewidth.

Figure 4.6 shows an oscilloscope trace of one of the locking cavities scanning over resonance with one of the Doppler cooling lasers. The error signal is fit to equation 4.14 and the

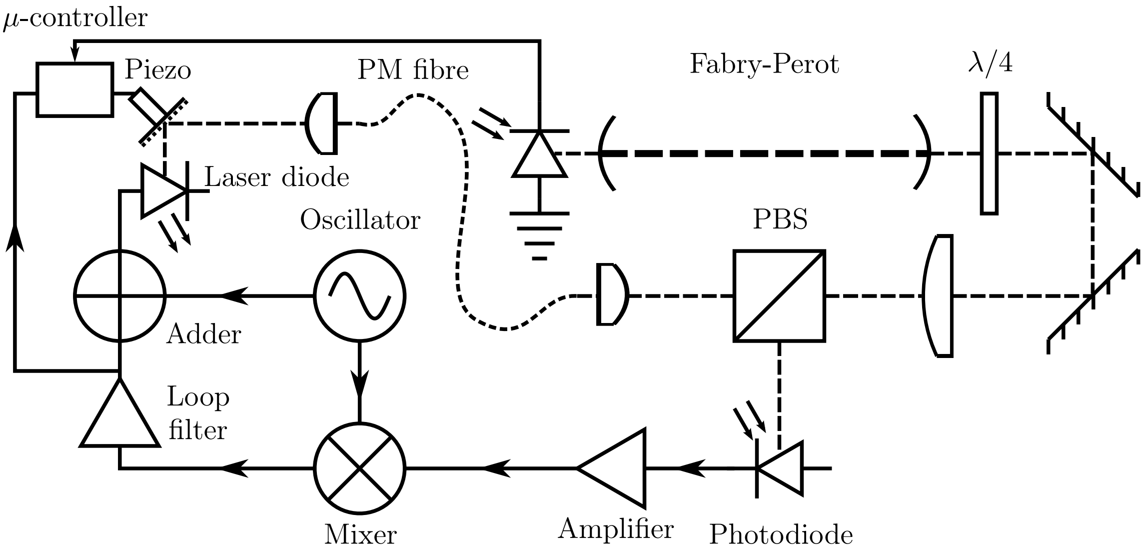

Figure 4.5: Schematic diagram of the dither lock for one of the 397 nm Doppler cooling lasers. Solid lines are electrical signals, dashed lines are light and the short dashed line is a PM fibre to take the light to the cavity setup. The DC laser diode current and piezo voltage supplies are not shown for clarity. See text for details.

best fit parameters suggest a cavity finesse of 50. However, if we measure the width of the transmission peak, the finesse is only 30. The difference is due to the imperfect peak shape. This can be attributed to dirt on the mirrors. Despite being housed in a vacuum chamber, they have been removed occasionally and were originally purchased more than a decade ago. The finesse of one of the cavities was significantly improved by intentionally snapping a mirror off the spacer and cleaning it before re-gluing it to the spacer.

4.3.4 Doppler cooling lasers transfer cavity lock

The cavities used in section 4.3.2 drift due to temperature variation such that they need to be adjusted several times an hour to maintain a constant fluorescence rate from the trapped ions. In order to remove any long term drift, the lasers are locked to a polarisation–stabilised HeNe laser via a home-made spectrum analyser. The essence of the lock is to keep the time difference from the HeNe to the Doppler cooling laser resonances constant, as the spectrum analyser is scanned over one free spectral range.

The cavity and electronics were built by Joe Goodwin and Daniel Crick. In this thesis an overview of the technical set up is provided but more information can be found in reference [46]. The cavity is built around a brass spacer with internal threading. Brass mirror holders with external threading fit onto the ends of the spacer. The mirrors have dielectric coatings for 633 nm and 397 nm. The cavity finesses at the different wavelengths are roughly 400 at 633 nm and 65 at 397 nm. The cavity has a single disc piezo attached

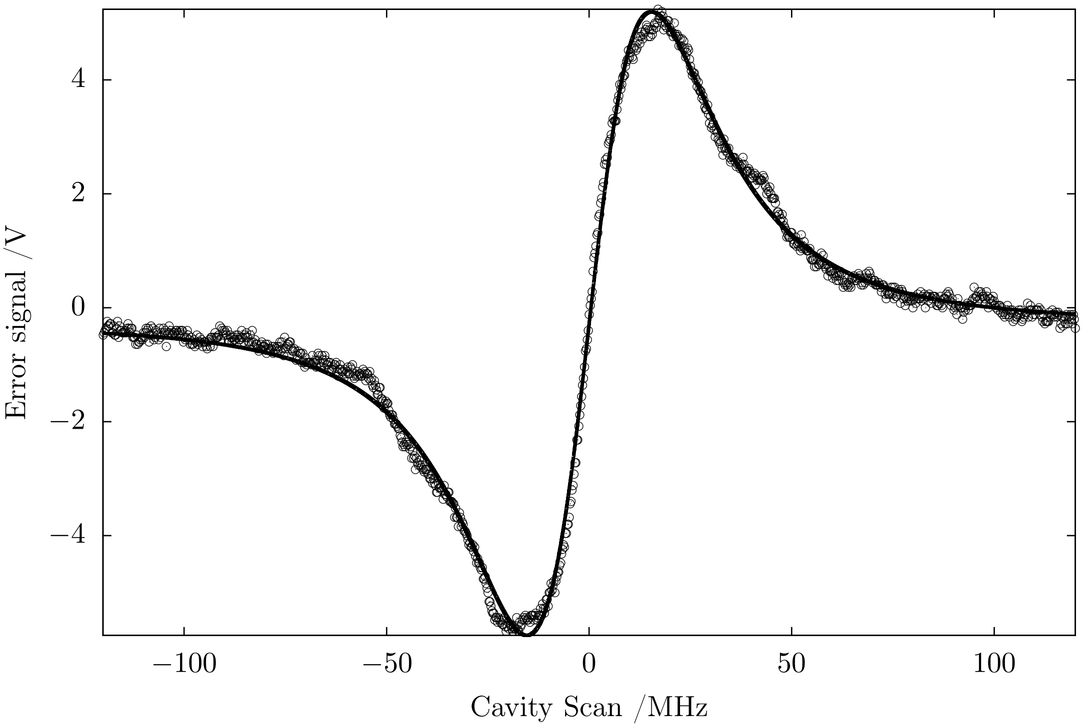

Figure 4.6: The loop filter amplified error signal of one of the Doppler cooling lasers as the Fabry-Perot cavity is scanned over a resonance (black circles). The error signal is fitted to equation 4.14 (black line).

to one mirror for scanning over slightly more than one free spectral range. A stacked disc piezo is attached to the other mirror and is used to compensate for thermal variations and to select a particular free spectral range with a suitable peak splitting.

In this section the HeNe laser will be referred to as the master and Doppler cooling lasers as slaves. Light from both slaves emerges from a PM optical fibre, is overlapped with the master on a dichroic mirror and coupled to the spectrum analyser. The cavity is 150 mm long and aligned to be confocal. The cavity is scanned with a sinusoidal drive voltage over one free spectral range of the master at approximately 2 kHz using a synthesised signal generator and a home-made amplifier. The free spectral range of the slaves is $\lambda_{397}/\lambda_{633} = 0.63$ times that of the master; so normally we observe 3 peaks from the Doppler cooling lasers within one free spectral range of the master. Two of these peaks are from one slave laser and one peak from the other. The transmitted light is split on a dichroic mirror. The master is detected on a photodiode and the slaves are coupled to a 600 μm multimode optical fibre and detected by a photomultiplier tube (PMT) with a simple transimpedance amplifier.

High speed analogue peak detectors convert the amplified photodiode signals to 5 V digital pulses. The peak detector only triggers when the differential of the photodiode signal goes through zero *and* when the absolute signal is above an adjustable threshold. After this point the pulses can be dealt with digitally. An inexpensive Arduino microcontroller measures the number of clock cycles from the start of the scan to several different pulses. The pulses and times that are measured by the microprocessor are shown schematically in figure 4.7. If the temperature in the lab varies, the length of the cavity spacer and the pressure and refractive index of air in the lab change. T_1 will get longer or shorter depending on the optical path in the cavity. To keep a whole free spectral range of the master inside the scan range, a voltage is fed back to the piezo stack. We assume that the scan frequency is stable but thermal variation of the amplifier may cause the amplitude of the scan to vary over time. This would appear like an effective frequency shift of the lasers. To avoid this, the microcontroller measures the time between the master peaks within one free spectral range, T_4. It then feeds back to the voltage controlled amplitude input of the signal generator to stabilise the scan amplitude.

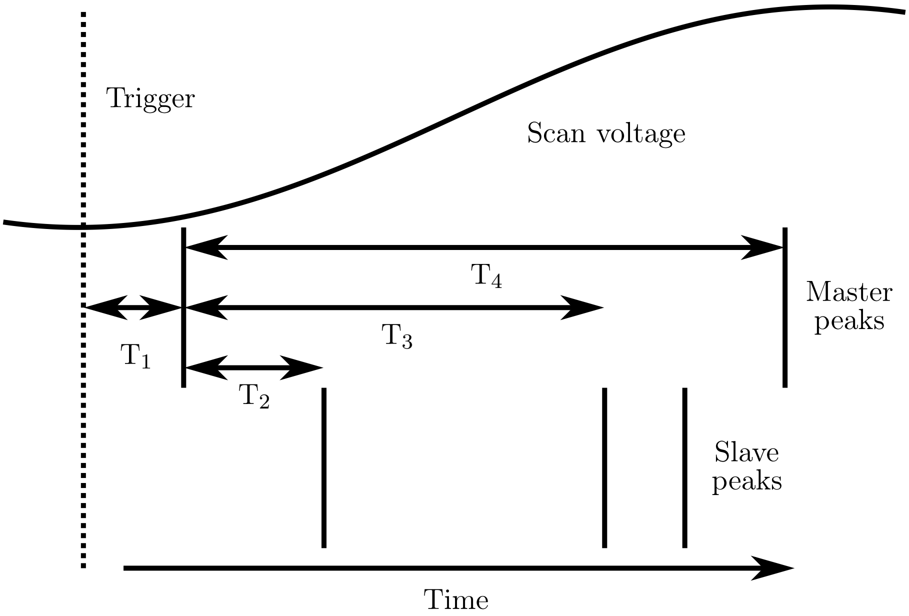

Figure 4.7: Order of peaks received by the microprocessor and the relevant times measured in clock cycles, from the trigger received from the signal generator. See text for details.

The differences between T_2 and T_3 during a particular scan, and their values when the lock is initialised are the effective error signals which are used as feedback to the lasers. These error signals are digitally integrated and fed back to the low-finesse dither-lock cavities through an aggressive low pass filter to avoid digitisation noise. The lasers are locked to these cavities via high bandwidth feedback to the laser diode current and ECDL grating piezo.

The measurements of T_1 to T_4 are made during one half of the sinusoidal scan. This type of scan was used after it was observed that harmonics in a triangle wave scan excited mechanical resonances in the cavity. On the return half of the scan, the feedback parameters are calculated using a look up table to compute arcsin (this removes non-linearities in the peak displacement). This error signal outputs via 16-bit, parallel digital-to-analogue converters (DACs)[2].

The set point of the lock is held as a digital variable in the Arduino memory. There is an external input which is used use to alter this variable. The lasers can then be tuned around resonance with 100 kHz resolution as long as the slave peaks in figure 4.7 do not overlap.

4.4 Repumping lasers

4.4.1 Multiple transition repumping

In section 4.1.1 it was mentioned that we need to repump not only the four $D_{3/2}$ but also four of the $D_{5/2}$ levels. The g_J values which determine the energy splitting of these levels, as a function of magnetic field, are shown in table 4.1.

State	g_J	Splitting /(GHz T^{-1})
$S_{1/2}$	2	27.992
$P_{1/2}$	2/3	9.331
$P_{3/2}$	4/3	18.662
$D_{3/2}$	4/5	11.197
$D_{5/2}$	6/5	16.795

Table 4.1: The g_J values and low-field Zeeman splittings for the relevant levels in $^{40}Ca^+$.

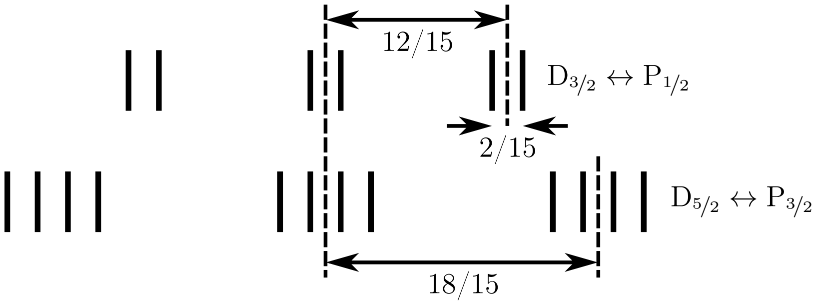

Figure 4.8: The splitting of the transitions between metastable D-states and P-states relative to the transitions in no magnetic field, in units of $\mu_B B$.

---

[2] Linear Technology LTC1597

Fortuitously, the energy splittings of the 854 nm and 866 nm transitions have a simple integer relationship. Figure 4.8 shows the magnetic field split $D_{3/2} \leftrightarrow P_{1/2}$ and $D_{5/2} \leftrightarrow P_{3/2}$ transitions at 866 nm and 854 nm. We modulate the phase of the laser light with an EOM to produce sidebands. The modulation frequency is $\nu_\alpha = 6\mu_B B/15$ and we set the modulation index to maximise the second order sidebands. When the second order sidebands are maximised, we also have a considerable amount of light in the third order sidebands, at the centre of the sigma $D_{5/2} \leftrightarrow P_{3/2}$ transitions. Then we also modulate the light by $\nu_\beta = \mu_B B/15$ to maximise the first order sidebands at this frequency using the same EOM. By combining both laser and microwave sources before sending them to the same EOM we obtain a whole array of sidebands. Figure 4.9 shows the optimal intensity we expect in the resonant sidebands relative to the total power out from the EOM. We have to remember that only the $D_{5/2,-3/2\ldots3/2}$ are populated via quantum J-state mixing. Hence this arrangement repumps all the relevant magnetic sub-levels for closed cycle Doppler cooling. We note that while the frequency splitting of the sidebands on the 854 nm laser is accurate, the carrier wavelength may drift by several hundred megahertz over a day because it is not included in the transfer cavity lock.

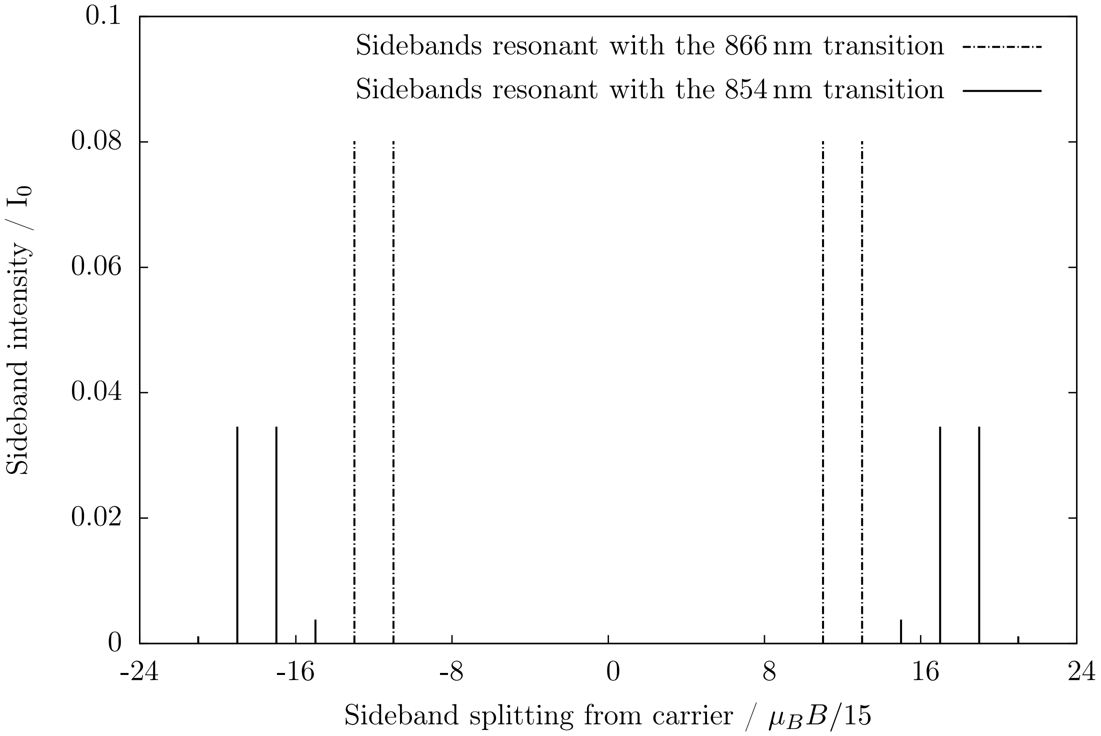

Figure 4.9: The lasers are modulated to maximise the second order sideband at $6/15\,\mu_B B$ and the first order sideband at $1/15\,\mu_B B$. The optimum sideband intensities relative to the total power out of the EOM is plotted. The remainder of the power is in the non-resonant sidebands (not shown).

The microwave frequencies that we use are derived from different sources so they are incoherent. For an analysis of using coherent microwave sources with controllable phase differences to optimise the relevant sideband amplitudes, and also a proposal to stimulate all the magnetic field split $D_{5/2} \leftrightarrow P_{3/2}$, $D_{3/2} \leftrightarrow P_{3/2}$ and $D_{3/2} \leftrightarrow P_{1/2}$ transitions in $^{40}Ca^{+}$ using one EOM, two microwave frequencies and four lasers, see chapter six of reference [41].

To implement our scheme the lasers are combined on an angle tuned dielectric filter[3]. The same filter also attenuates 854 nm amplified stimulated emission (ASE) in the 866 nm laser by 36 dB. This is useful because during spectroscopy of the $S_{1/2} \leftrightarrow D_{5/2}$ quadrupole transition we need to apply laser pulses in the absence of any 854 nm light. These lasers are then coupled into the fibre pigtailed, waveguide EOM[4]. The modulator has approximately 40 % transmission due to imperfect mode-matching between the input (and output) fibre and the waveguide. The microwaves are derived from a synthesised CW generator[5] at 10.4000 GHz and a voltage controlled oscillator[6] (VCO) at 1.7365 GHz. The signal generator can be attenuated in 0.1 dB steps but the power of the VCO, nominally 7 dBm, can only be altered in 1 dB steps with fixed, inline, attenuators. These sources are then combined on a resistive power splitter[7] and amplified using a wideband amplifier[8] with 26 dB gain. The setup is shown in figure 4.10.

The fibre-pigtailed EOM that we use couples light from the input polarisation-maintaining fibre into a $LiNbO_3$ waveguide. The waveguide has a similar width to the input and output fibre, which allows the electrodes, which are either side, to produce a high electric field for a relatively small input voltage. The RF input power is then dumped into an internal 50 Ω terminator, with a maximum power rating of +27 dBm. The electric field can also be applied over the entire length of the waveguide to allow a high modulation index. We characterised the modulation index as a function of RF voltage; figure 4.11 shows the intensities of sidebands after the modulator when driven at 16.8 GHz. We have observed it is possible to maximise the 4th order sideband at this frequency, limited by the internal terminator.

4.4.2 Repumping lasers transfer cavity lock

The transfer cavity lock for the repumping lasers works in a similar way to the one described in section 4.3.4 with a few minor changes. The cavity is the same design and uses the same

---

[3] Semrock LP02-980RS-25

[4] EOSPACE PM-0K5-20-PFA-PFA-850

[5] HP 8650L

[6] Mini-Circuits ZX95-2600-S+

[7] Mini-Circuits ZFRSC-183-S+

[8] Mini-Circuits ZVA-213-S+

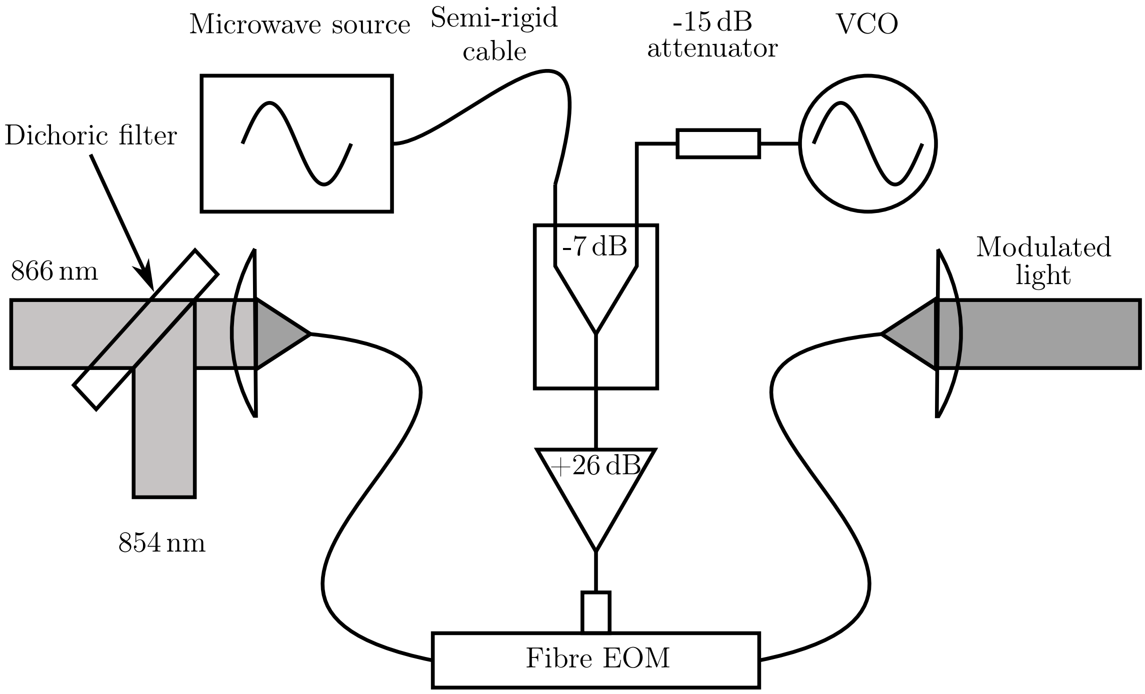

Figure 4.10: Experimental apparatus for repumper laser modulation.

master laser as a reference. The mirrors are also custom made with finesses of roughly 50 at 633 nm and 866 nm. We only lock the 866 nm laser using this method, while the 854 nm laser is left unlocked, since the repumping rate required from this laser is very low. Transmission through this cavity at the relevant wavelengths is much higher than the spectrum analyser described in section 4.3.4 therefore the transmitted light is simply detected on photodiodes with transimpedance amplifiers.

This cavity is scanned at 200 Hz with a triangle wave and instead of feeding back to the function generator to maintain a constant scan amplitude we divide all the variables by the time required to scan a free spectral range of the cavity at 633 nm.

The feedback from the transfer lock is applied directly to the ECDL grating piezo; there is no other high bandwidth locking system involved with the 866 nm laser. We attempt to heavily saturate the $D_{3/2} \leftrightarrow P_{1/2}$ transition so small variations of the laser frequency do not significantly alter the repumping rate.

4.5 Stabilised 729 nm Laser

The vast majority of work to stabilise the 729 nm laser diode to the reference cavity was done by Daniel Crick with some minor help from Sean Donnellan and myself. Some of the technical details of the locking system are described here for completeness only. For more

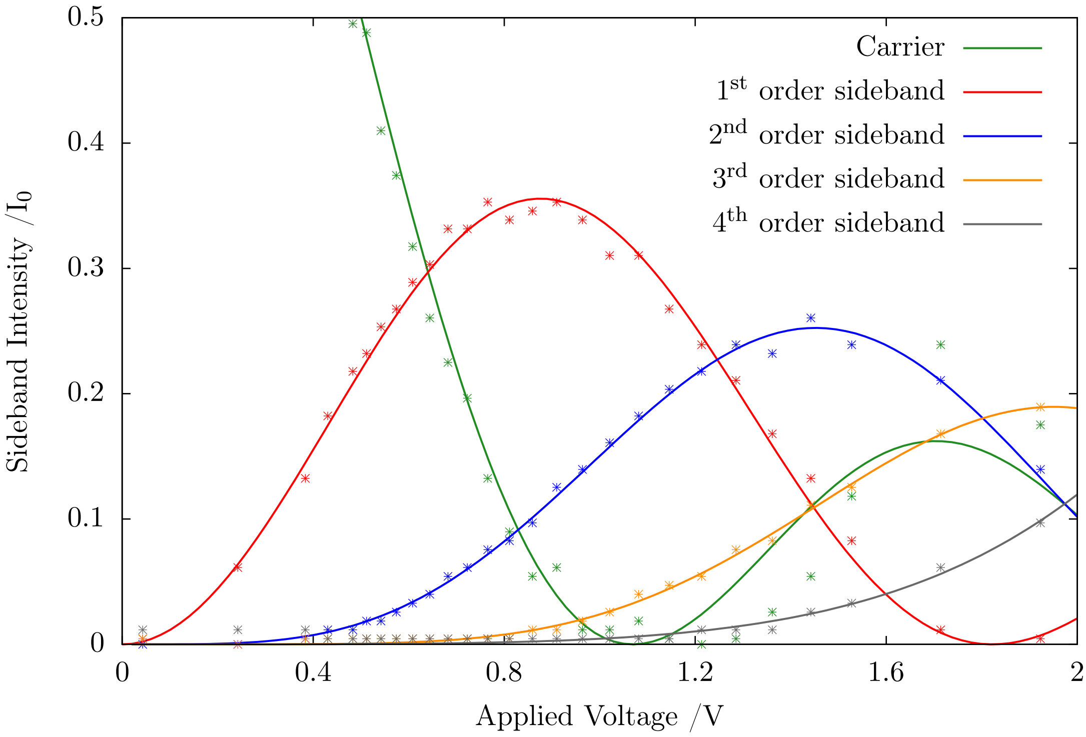

Figure 4.11: Sideband intensities measured on an optical spectrum analyser after the fibre EOM at a 16.8 GHz modulation frequency. The intensities have been fitted to Bessel functions and normalised to the output carrier intensity with no modulation. The input RF voltage was set on a microwave source and then connected to the fibre EOM using a homemade semi-rigid cable with unknown S-parameters, so the applied voltage must be multiplied by some factor less than unity.

general information, reference [43] is an excellent introduction into locking ECDLs to high finesse cavities via the PDH scheme.

We lock a diode laser[9] to a high finesse cavity with a spacer made of ultra-low expansion (ULE) glass to reduce its linewidth. If the trap was perfectly stable, the ion would act as an extremely high-Q oscillator to which the laser could be compared. However, it is unknown whether the width of the sidebands in section 6 is predominantly from laser phase noise or magnetic field fluctuations.

4.5.1 ULE high finesse cavity

The cavity was placed inside an ultra-high vacuum chamber and evacuated with a turbo molecular pump. The vacuum chamber was valved off after a few days with an all metal angle valve and any remaining pumping done with an ion pump. The ion pump current

---

[9] Optnext HL7301MG

supply suggests a vacuum pressure between 10^{-7}–10^{-8} mbar. The vacuum ensures that there is no pressure change inside the cavity, maintaining a constant optical path length. To shield the laser system and locking optics from air currents and variations in temperature the entire system is enclosed inside a wooden box lined with foam. The temperature of the vacuum chamber is also stabilised and the recorded error signal showed a maximum deviation of approximately 0.5 mK while the box enclosing the laser stabilisation setup remained closed. The vacuum chamber also provides thermal isolation of the cavity from the environment.

ULE glass is designed so that it has a very small expansion coefficient which goes through zero at a temperature near 20°C. Above the turning point the glass expands with increasing temperature whereas below the turning point the glass contract with increasing temperature. The manufacturer is not able to control the temperature of the turning point from batch to batch. It is therefore necessary for users to identify the turning point by making their own measurements. The results in this thesis were taken while the cavity was temperature stabilised but not at the thermal turning point.

The cavity linewidth (and finesse) can be found by first locking the laser to the cavity and then quickly shifting the laser off resonance. The cavity mode decays as light leaks out through the mirrors. The rate of decay of the intensity of light incident on the transmission photodiode should be directly related to the cavity linewidth. This technique is commonly named cavity ring-down spectroscopy. The data in figure 4.12 is fitted to an exponential decay and suggests that the cavity has a linewidth of 25.3 kHz (or a finesse of 59300).

4.5.2 Laser & Locking electronics

The vast majority of the electronics for this laser were home built by Daniel Crick. The commercial alternatives that were initially used were found to add noise to the laser light.

DC current supply

The laser diode has a 75 mA operating current and a 100 mA absolute maximum rating and a 2.5 V diode voltage drop. The DC supply is provided by ten 10 V voltage references and 1 kΩ low thermal coefficient shunt resistors in parallel. The circuit diagram is shown in figure 4.13.

Voltage references provide an extremely low drift supply with very low noise. The noise is attenuated further when used in parallel as shown in figure 4.13. These are both properties that make them ideal for a low noise current supply. However, we still found it useful to employ a high-capacity, trickle charged, 12 V battery as the power supply. This reduced

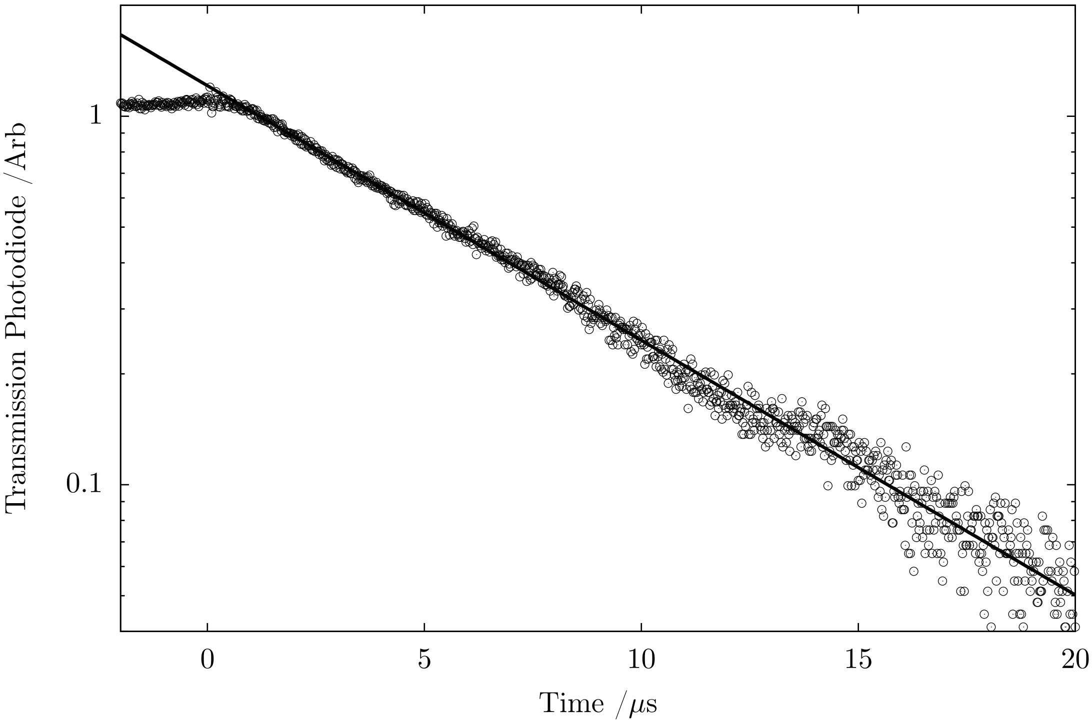

Figure 4.12: Light detected on a photodiode recording transmission through the high finesse cavity after the laser was quickly removed from lock (black circles). This data is fit to an exponential decay function to measure the decay time for the cavity mode (black line). Data obtained by Daniel Crick.

the residual mains noise on the laser.

Feedback electronics

The electronic servo system should be designed not to limit the bandwidth of the lock. The loop filter should provide enough electronic gain to the laser diode to reduce the frequency fluctuations to less than the linewidth of the reference oscillator. The phase margin (the phase shift from 180° at the frequency where the amplifier gain falls below unity) should be at least 45° to avoid oscillation [43]. This usually means that the transfer function should not be steeper than -20 dB per decade or equivalent to $1/f$ slope at unity gain. However, ideally there should be very large gains at low frequencies because the suppression of noise at a particular frequency is approximately the inverse of the gain at that frequency.

A high finesse cavity acts as a frequency discriminator at frequencies lower than the cavity bandwidth, but like an integrator at higher frequency. This adds a pole to the transfer function of the feedback at the cavity bandwidth. The transfer function of the loop filter

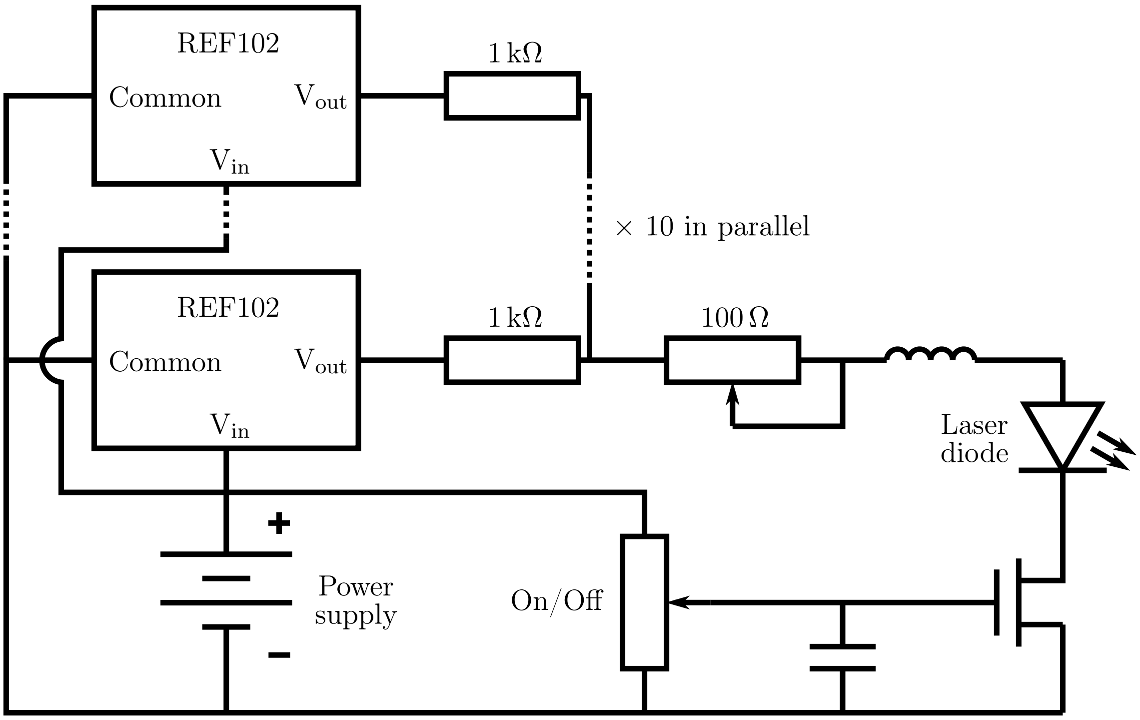

Figure 4.13: Laser diode DC current supply using voltage references. The supply has very low drift and allows the current to be varied between 68 mA and 75 mA assuming a 2.5 V potential difference across the laser diode.

is designed to take into account this effect. The loop filter has several TTL switches to change the transfer function between a full integrator at low frequency to merely a very high gain amplifier.

A diagram of the locking system is shown in figure 4.14. The loop filter has two offsets that must be set manually to maintain a good lock. First is the input offset; this is a DC offset on the error signal which can be nulled by summing the error signal from the mixer with a DC voltage. The second is the output offset, which keeps the voltage at the output with no gain on the amplifier the same as the laser diode voltage drop. This means that when the lock is engaged the laser frequency is not disturbed.

An Arduino microcontroller controls several TTL operated analogue switches inside the loop filter. This controller takes an input from a photodiode placed after the reference cavity to measure transmission. This signal is compared to approximately half of that which is expected when the laser is locked. When the auto-relock switch is engaged, and this comparator gives a low signal, the error signal is replaced with a slow (approximately 150 Hz) triangle wave at the input of the loop filter to scan the laser frequency. When transmission through the cavity increases again, and the laser is on resonance with the cavity, the standard locking system is re-engaged.

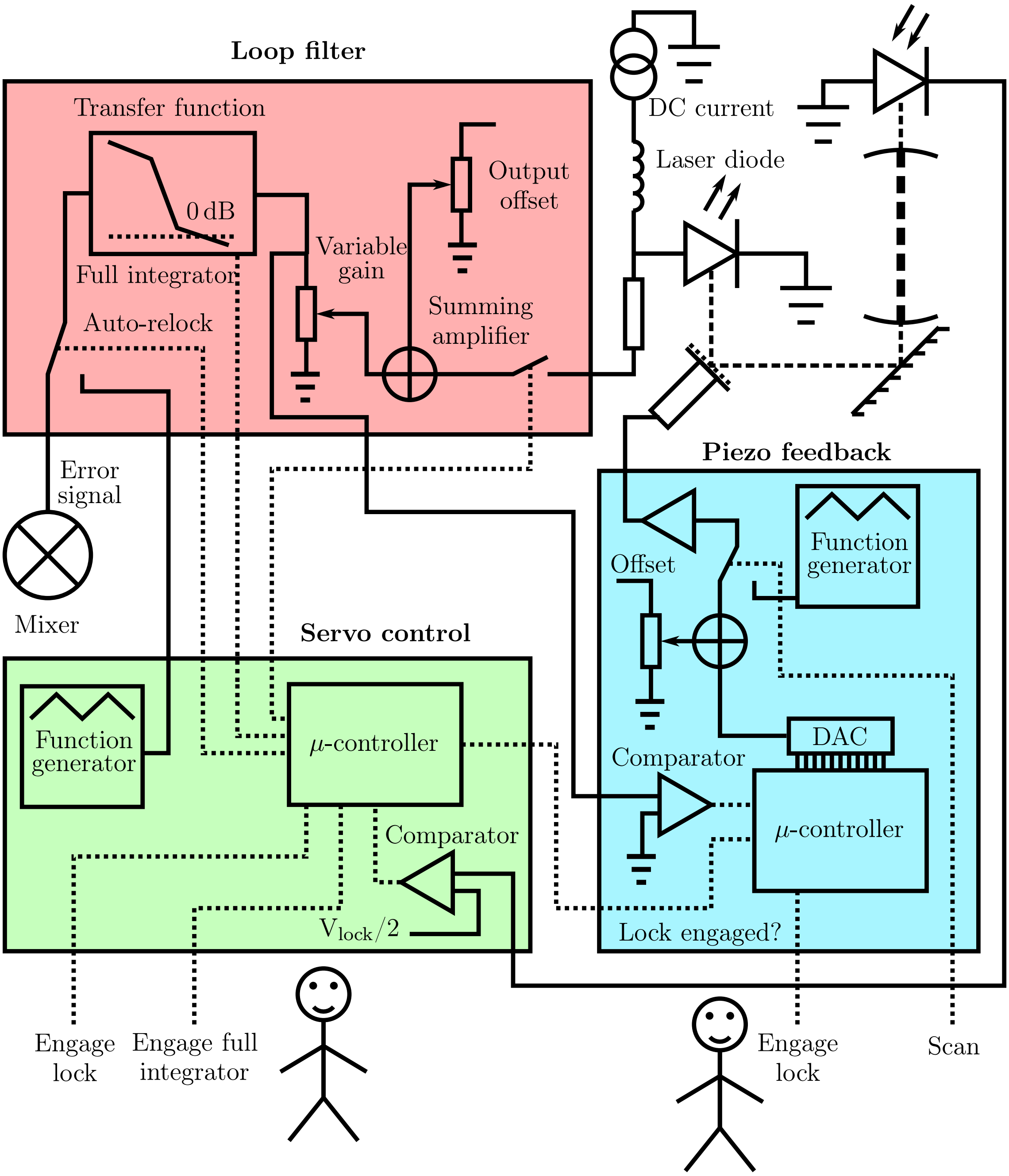

Figure 4.14: Schematic block diagram of the high bandwidth laser locking scheme for the quadrupole spectroscopy 729 nm laser. Solid lines are analogue signals, dotted lines are digital signals and dashed lines are light. Not all the details are show for clarity, see text for more information.

The loop filter provides an error monitor before the variable gain stage. This is sent to a separate control system for the piezo feedback, increasing the low frequency gain. Inside the piezo controller, the error signal is compared to ground to detect whether the error signal is positive or negative. The microprocessor then increments the piezo voltage via a 16-bit, high speed, low glitch, parallel DAC[10].

Additionally, the piezo controller takes an input from the servo controller to instantly freeze the piezo voltage and avoid the laser frequency moving too far from resonance if the laser becomes unlocked. The piezo feedback is restored when the transmission photodiode measures that the lock has been restored.

4.6 Optical setup

The overall optical setup of the experiment is separated into two parts. The first is the optical tables with the associated laser locking and switching apparatus. Fibre optics at the end of this chain then transfer the laser light to an optical breadboard on which the experimental vacuum chamber sits. The breadboard includes optics for combining different wavelength light and focusing it onto the ion.

Light from all the laser diodes used have different widths in the vertical and horizontal directions because the diodes themselves physically have an aspect ratio of roughly 3:1. We initially shape these beams using either anamorphic prisms or single axis Keplerian telescopes composed of cylindrical lenses. The lenses are tilted slightly to avoid back reflections to the diodes. The light then passes through Faraday isolators to reduce feedback from optical elements further down the beam line. After the isolators, half wave plates and polarising beam splitters are used to split the light into two paths, one for laser locking and wavelength determination and the other for the laser cooling in the experiment.

For the Doppler cooling lasers some light is picked off the laser locking beam path, and then sent to the dither lock cavities described in section 4.3.3 via PM fibres. The remainder of this light, from the two lasers, is combined on a 50:50 non-polarising beam splitter cube. The mixed light from one of the output ports of the beam splitter goes to the transfer cavity lock described in section 4.3.4 via a PM optical fibre. The light from the other output port is sent to a Fizeau interferometer wavemeter[11] in an adjacent laboratory[12], via an approximately 60 m long single mode fibre.

The light that is sent to the experiment after the isolator first travels through double passed

---

[10] Linear Technology LTC1597

[11] High Finesse WS-6

[12] Use of the wavemeter is kindly provided by Centre for Cold Matter at Imperial College.

AOMs[13] before being combined on a non polarising beam splitter cube. The beams from the two outputs act as a pair of cooling beams, one sent along the axis of the trap (axial cooling beam) and one sent along the radial plane (radial cooling beam).

Of the repumping lasers, only the 854 nm laser has an AOM in its path. The 866 nm laser is left on continuously. These two laser beams are combined on a dielectric filter and pass through the high frequency EOM described in section 4.4.1. The combined repumping light is then split on a 80/20 plate beam splitter with 80 % to the radial repumping beam and 20 % to the axial repumping beam via PM optical fibres. The narrow linewidth laser at 729 nm is combined with the axial or radial repumping light after the EOM. A diagram showing the major features of the layout is shown in figure 4.15.

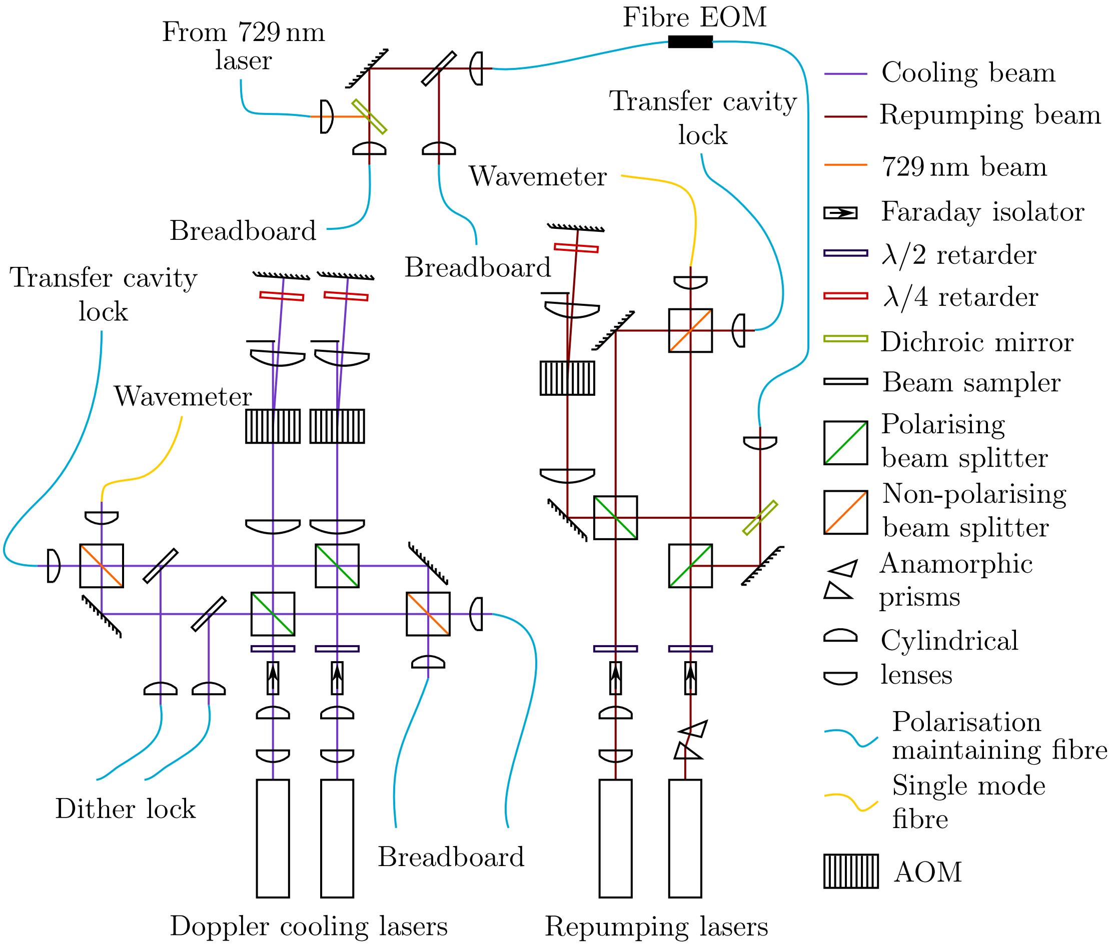

Figure 4.15: Optical table layout (beam steering mirrors are not shown). The labels on the diagram show where the fibres end. See text for details.

All the light required for laser cooling is coupled into PM fibres and sent to the breadboard

---

[13] Isomet 1206C-833

holding the trap apparatus. On the breadboard, one set of repumping laser beams and one set of cooling laser beams are overlapped to form the axial laser beam, using a dichroic beam splitter. Similarly, the other set of repumping and cooling beams are combined to form the radial laser beam. These beams are then focused onto the trap centre. The axial beam uses a $f = 400\,\mathrm{mm}$ lens and the radial beam, a $f = 500\,\mathrm{mm}$ focal length lens which give $1/\mathrm{e}^2$ diameter spot sizes of $85\,\mu\mathrm{m}$ and $105\,\mu\mathrm{m}$ respectively. The radial beam exits the trap and is reflected back down to the breadboard, passes through a glass colour filter and hits a quadrant photodiode. The vertical beam exits through a window on the top of the vacuum chamber, passes through a dielectric beam splitter and a glass colour filter before hitting another quadrant photodiode. We use these detectors and a simple computer program to monitor the position of the laser beams.

For trap loading, photoionisation is performed via non-resonant multi-photon excitation at 532 nm using light from a pulsed, frequency-doubled Nd:YAG laser. This laser sits on a separate small table bolted to the superconducting magnet cryostat. The output from this pulsed laser cannot be coupled into a fibre because the instantaneous pulse power is too high. The light counter-propagates along the axial laser cooling path with a focusing lens just before the window above the trap. There are more details of the loading procedure in section 4.8. A diagram of the optical setup on the breadboard can be seen in figure 4.16.

4.7 Trap configuration

The trap that we use for the experiments was originally built by Shailen Bharadia and described in reference [47]. Here, I provide a brief description of the trap and and the changes made to the optical access to perform the experiments in this thesis.

We use a solenoid superconducting magnet, operating at 1.85 T, to provide the radial confinement. The trap is inside a vacuum system pumped by a $40\,\mathrm{l\,s}^{-1}$ ion pump and a non-evaporable getter pump[14] which is especially good for low mass particles. The pressure inside the vacuum system is less than 10^{-9} mbar.

The trap electrodes are cylindrical and machined from oxygen-free high conductivity copper. They have a 21.6 mm inner diameter. This means that they are much less sensitive to misalignment than in a miniature ion traps. The ring electrode is split vertically in to 4 segments, to allow a rotating dipole RF field to be applied to the ion [48]. Precise dimensions for all the electrodes are given in reference [47]. There is also a 4 mm diameter hole drilled in each of the ring segments. Two of these apertures are used for laser beam access and the other two are used for fluorescence collection. The electrodes are kept electrically

---

[14] SAES Getters CapaciTorr D 400

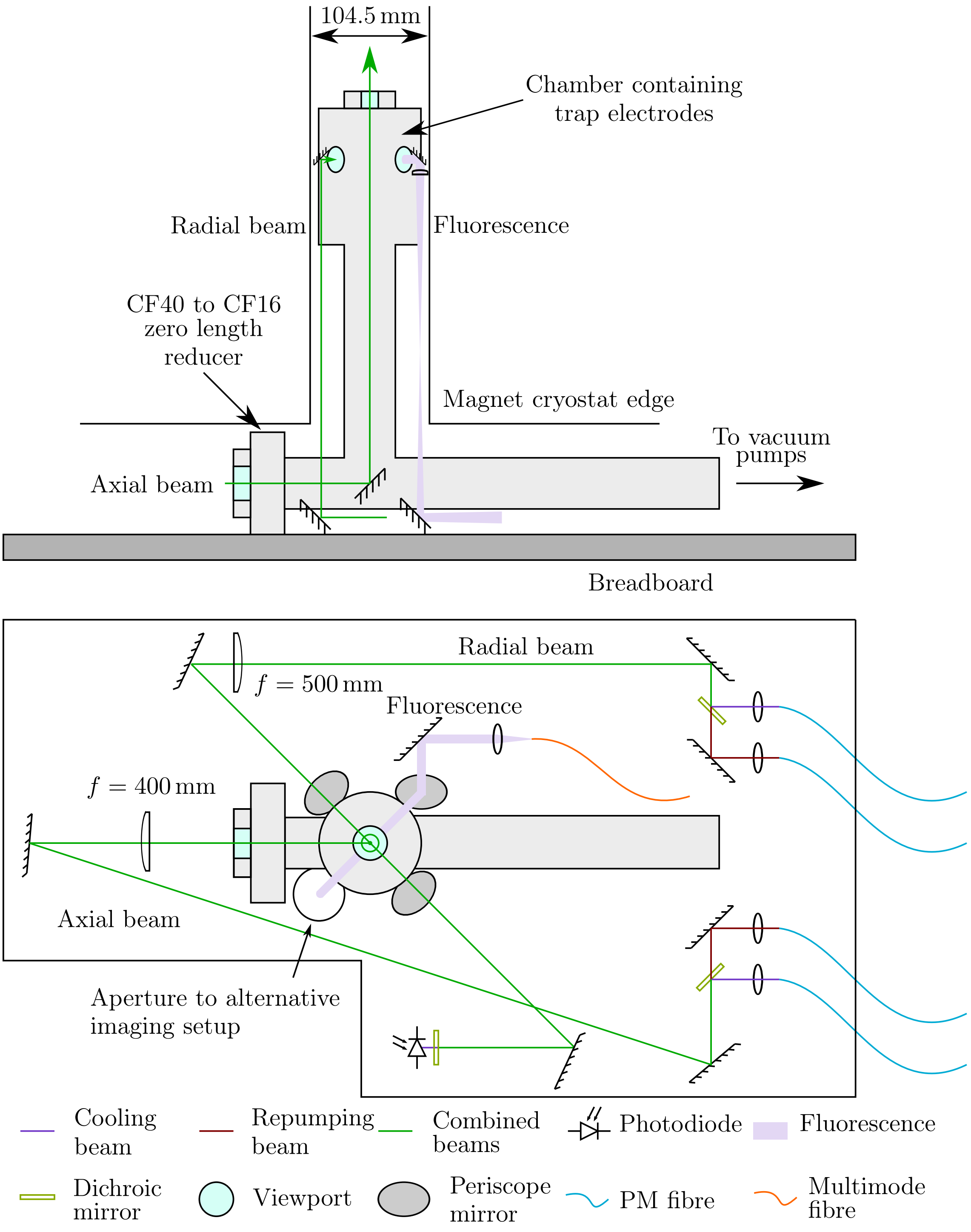

Figure 4.16: Top: simplified diagram of the vacuum chamber and laser beam paths seen from the side. The mirror that directs the axial beam vertically is inside the vacuum chamber, see section 4.7. Bottom: top down view of the optical and vacuum setup. Only part of the vacuum chamber is shown (light gray). All the laser light arrives at the breadboard via PM fibres. The first mirror after the radial beam focusing lens is a computer controlled piezo motor mount.

isolated either using small sapphire balls or macor rings. The trap electrodes are mounted on four copper rods which attach to a mounting plate. The mounting plate is bolted onto a vacuum flange which also has three 4-pin feedthroughs welded onto it. The vacuum flange is also fitted with a CF16 viewport.

Optical access has been increased since reference [47] to allow laser beam access along the trap axis. A window was installed on the vacuum system at the same level as the optical breadboard optics to allow laser access. A custom, fixed, mirror holder is bolted to the inside of the vacuum chamber. A mirror here allows laser light to be directed vertically upwards. Figure 4.17 shows a CAD rendering of the mirror holder and the vertical laser beam. The holder mounts into two threaded holes in a CF40 to CF16 zero length reducer. There is an 397 nm anti-reflection coated CF16 viewport[15] on the other side of the reducer. This window is used to send the laser light into and out of the trap. We use a Semrock Maxmirror in the vacuum which has high reflectivity for all polarisations and wavelengths from 350 nm to 1100 nm.

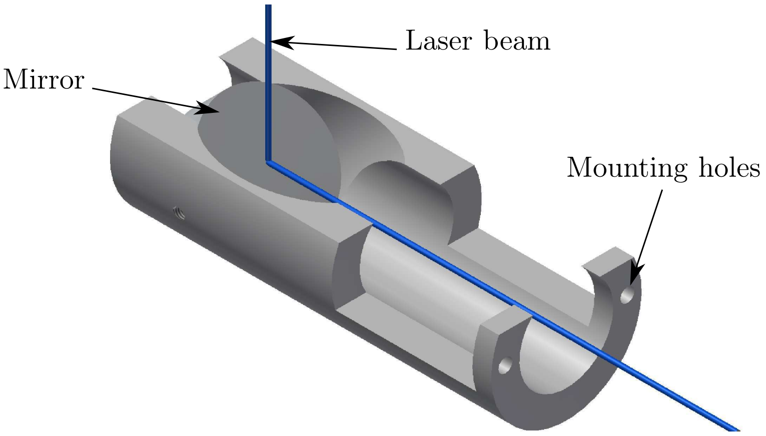

Figure 4.17: Mirror mount which allows vertical optical access. The holder is mounted in the vacuum chamber on CF40 to CF16 zero length reducer as shown on figure 4.16.

To allow unobstructed optical access vertically along the trap, we have removed the electron bombardment filament used for the experiments in reference [47]. The effusive calcium oven has also been shifted to below the trap and off-axis. Figure 4.18 shows the current setup of the trap with laser beams, fluorescence detection optics and electrodes displayed.

Apertures in the ring segments through which fluorescence is collected limit the detection solid angle. The combination of both 4 mm diameter apertures, 10.8 mm from centre of the trap allow, at most, the collection of 1.5 % of the spontaneously emitted light. The light is channelled along two paths, through 14 mm gaps, between the vacuum chamber and the edge of the magnet bore before it can be detected.

---

[15] Torr Scientific VPZ16VAR-LN

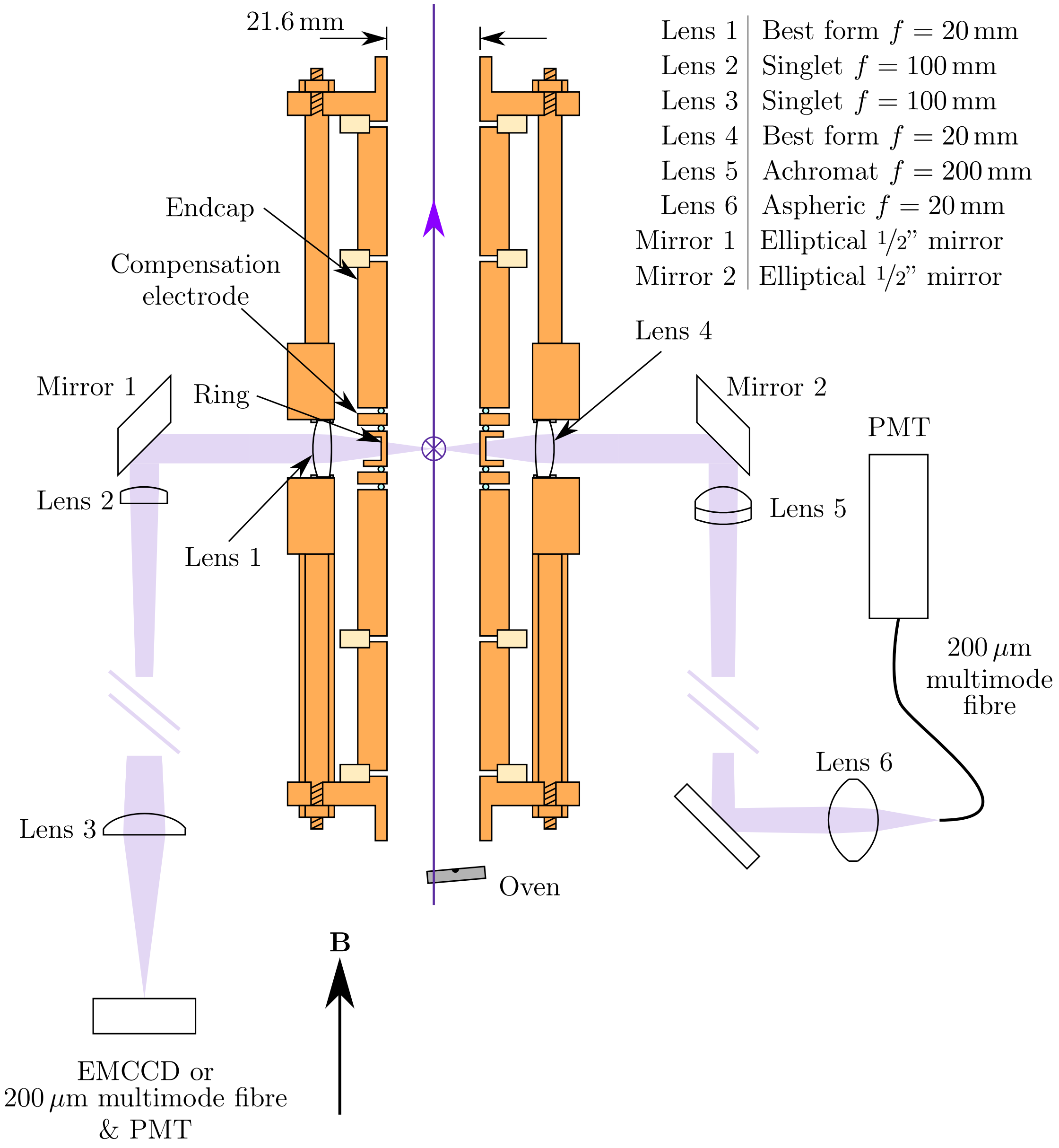

Figure 4.18: Trap and fluorescence detection setup. The trap electrodes are shown in orange along with the support structure which is also made of copper. The support structure is comprised of a pair of end plates and four copper rods. A pair of copper lens holders are attached to the rods near the centre of the trap. The central electrode is the ring which is radially split into 4 segments. Each segment has a 4 mm aperture. The fluorescence, shown in light-purple, exits through two apertures and is nominally collimated by lenses inside the vacuum chamber. Above and below the ring are a pair of compensation electrodes. Above and below the compensation electrodes are the endcaps. Above and below the endcaps are another pair of electrodes not used in this work and which are internally grounded. The inner electrodes are separated by small sapphire balls, shown in light-blue, and the larger electrodes by macor rings, shown in beige. The laser beams propagate vertically, shown by the purple arrow, and radially shown by the circle with a cross inside at the centre of the trap. The oven is below the electrode and displaced from the trap axis.

Photomultiplier tubes are susceptible to the fringe field of the magnet; they need to be at least 1 m from the base of the magnet to operate properly. To avoid long-distance free space optics, we permanently couple one of the paths into a 200 μm, 0.22 NA, solarization-resistant optical fibre. These optical fibres do not have anti-reflection coated ends and a bulk attenuation of around 1.5 %/m. The end of the fibre is fixed with an adapter approximately 2 mm from the detection face of the PMTs. The other path can be swapped between a similar multimode fibre or an amplified camera[16] for imaging.

4.8 Loading Ions

To load $^{40}\mathrm{Ca}^+$ ions into the trap we follow a three step procedure. Initially, we resistively heat a 2 cm long calcium filled tantalum tube with a hole in one side pointing towards the centre of the trap. Once this tube, which we call the oven, begins to glow dimly a small amount of calcium starts to effuse out of the hole and some of it is sent towards the trapping region. After the oven has been heated like this for 30–60 s we pulse the Nd:YAG laser[17] 5–50 times in a short burst lasting a few seconds. The laser has an average pulse power of 1–10 MW during its approximately 5 ns pulses. A non-linear non-resonant three-photon process ionises some of the atoms. The process is not isotope selective and the loading rate is greatly variable. These atoms are ionised over the length of the 532 nm beam which may not overlap with the centre of the trap. This creates ions out at large radii and with large axial displacements. Figure 4.19 shows fluorescence from $^{40}\mathrm{Ca}^+$ ions cooling into the centre of the trap from large orbits over several seconds after we have stopped pulsing the high power laser. This behaviour can continue for several minutes. This is highly undesirable if we wish to perform experiments with a single ion or a well defined number of ions. We have developed a method to control the number of ions loaded which is described below.

Penning traps have no micromotion and the ions are not heated when they are away from the centre of the trap. Furthermore Penning traps are stable for ions with a large range of charge to mass ratios. Hence, our loading process can produce many undesirable ions. The laser cooling acts quickly on the correct isotope of calcium but non-resonant ions can remain trapped in large orbits which occasionally interfere with the experiment. To remove the unwanted ions we simply turn off the electrostatic trapping field for 10–20 μs. During this time the cooled ions in the trap undergo a Coulomb explosion. The ions in large orbits are lost from the trap altogether. After the trapping field is restored the calcium ions that were initially in the centre of the trap are quickly cooled again. To reduce the number of ions in the trap we repeat the same procedure but when the required number of ions have

---

[16] Andor Luca R.

[17] Continuum Surelite II

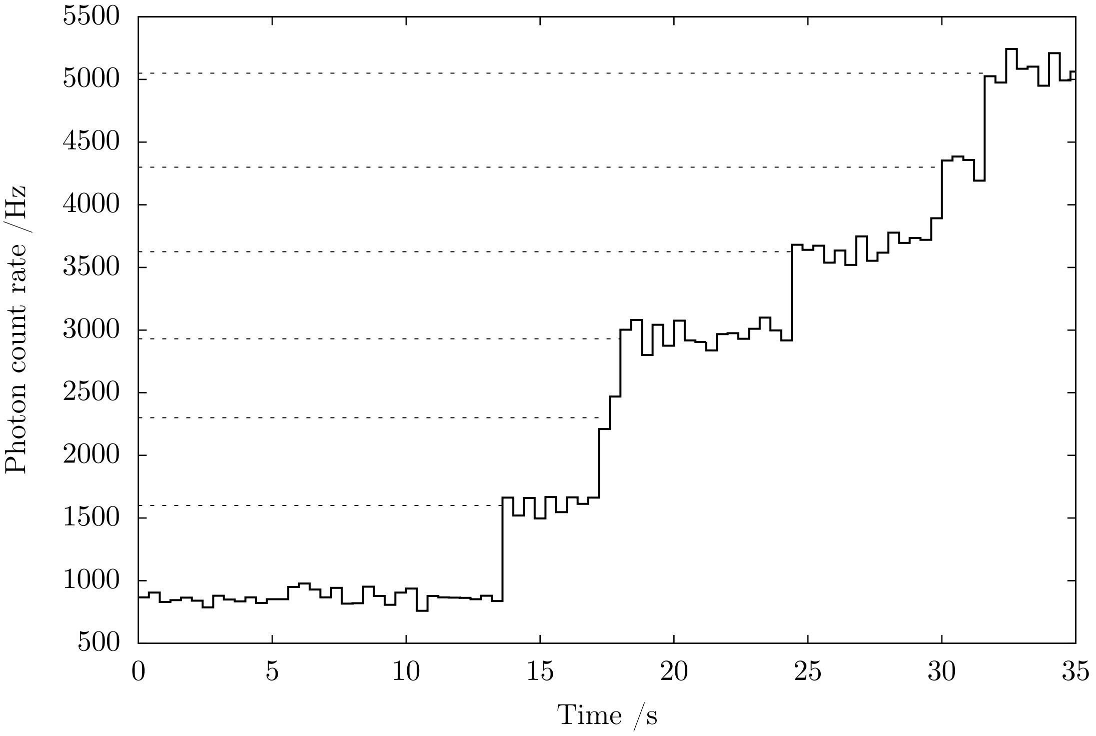

Figure 4.19: PMT count data after loading using the non-resonant pulsed Nd:YAG laser. Dashed lines are marked where ions cool to the centre of the trap. The initial count at approximately 800 Hz is scattered background light from the lasers.

been re-cooled to the centre of the trap we turn off the trap again in an attempt to eject any remaining $^{40}\mathrm{Ca}^{+}$ ions still in larger orbits. Using this technique we can load between one and roughly 30 ions at will.

4.9 FPGA and computer control

The $\mathrm{S}_{1/2} \leftrightarrow \mathrm{D}_{5/2}$ electric quadrupole transition in $^{40}\mathrm{Ca}^{+}$ has a spontaneous decay rate of roughly 1 Hz. This makes standard fluorescence or absorption spectroscopy infeasible. Instead we use the high bandwidth $\mathrm{S}_{1/2} \leftrightarrow \mathrm{P}_{1/2}$ transition as a diagnostic as to whether the ion has been shelved in metastable $\mathrm{D}_{5/2}$ state. The procedure is to Doppler cool an ion for a few milliseconds, then turn off a particular 397 nm laser for around a hundred microseconds. This leaves the ion in a thermal state, optically pumped into one of the magnetic sub-levels of the $\mathrm{S}_{1/2}$ states. The 729 nm spectroscopy laser is then pulsed on for a few milliseconds. This is again followed by a few milliseconds of Doppler cooling. The ion will not fluoresce during this final stage if the 729 nm laser has excited the ion to the long-lived $\mathrm{D}_{5/2}$ state. This technique produces a digital signal (i.e. is the ion fluorescing or not) which must be repeated many times at each laser frequency to calculate a shelving probability. Once this is done, the laser frequency can be changed and the whole procedure repeated to build up a spectrum.

During my time in the laboratory, we installed AOMs in the beam lines to allow repetitive pulsed spectroscopy to be carried out. Also, previously, photons detected by PMTs were counted using a fast EG & G Ortec multichannel scaler card. This computer card only has 8192 channels and was reliant on a computer with an ISA interface, which is now an obsolete standard. To overcome these limitations we decided to build a more future-proof system based around a modern PC and a field programmable gate array (FPGA) development board. The system was developed by two MSci project students, Shamim Patel and Stefan Zeeman, with supervision from Daniel Crick and myself. More information can be found in references [49, 50].

A standard experiment starts at a particular frequency, and carries out many pulse sequences to detect the state of the ion after applying the 729 nm laser to the ion. The FPGA then records the number of photons detected by the PMTs. See section 6.1 for more details. The data for that frequency are sent back to the computer and analysed to build up a spectrum of the transition. The computer then tells the function generator to change frequency and the FPGA repeats the pulse sequences. Eventually, the FPGA reaches a stop command, a signal is sent back to the computer and the experiment ends.

The control system should be able to perform all the laser pulses and gated photon counting described in section 6.1. We also require an efficient communication protocol between the PC and FPGA. Figure 4.20 shows the network of computer controlled apparatus in the experiment and the communication between these items.

FPGAs are made up of logical elements. Each logical element can be configured to imitate different digital gates. These gates can be configured in different orders to perform different tasks. Hence, FPGAs can be considered as software programmable hardware. This direct hardware manipulation of inputs to give certain outputs is inherently faster than using a standard microprocessor because the processing is done by optimised discrete elements. One area of the device can be configured to deal with a certain task and another area can perform a completely different task. These operations can then be synchronised exactly. This is in contrast to executing a list of instructions in a serial fashion which is what happens on a microprocessor. For example, the signal to switch several AOMs on or off can be sent at exactly the same time, measured to within the resolution of our 300 MHz oscilloscope[18], as well as doing several other tasks simultaneously. The timing resolution of these operations is set by the clock speed of the FPGA: 50 MHz for our development board.

---

[18] Tektronix TDS3032B

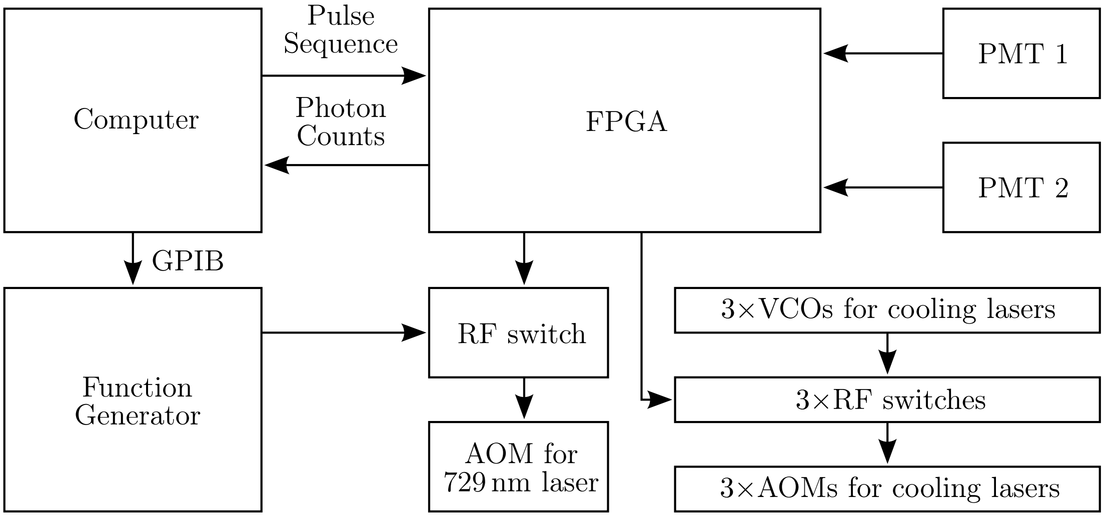

Figure 4.20: The interaction between the apparatus used to automate pulsed spectroscopy.

The FPGA[19] that we use employs an internal 3.3 V TTL voltage. To interface with 5 V signals in other parts of the system we step the voltages up and down using digital buffers[20]. These are extremely fast, 13 ns propagation delay according to the data sheet, and provide no discernible delay on the signals.

4.9.1 Computer front-end

The program which interfaces with the FPGA and the function generator was written in-house by the masters students mentioned in section 4.9. This computer interface provides a simple way of setting up an experiment. The program compiles the experimental sequence into the binary format which the FPGA expects and uploads it. This program also tells a GPIB interface card[21] what data to send to the signal generator. In addition, the computer program receives data from the FPGA, saves it in a suitable text file, and performs several simple handshaking requirements. Figure 4.21 shows a screenshot of the control program.

4.9.2 FPGA memory interface

The FPGA development board that we use has 3 types of memory available:

- Synchronous dynamic random access memory (SDRAM) - 8 MB: this is similar to memory on PCs. It has a relatively fast access rate and is large enough to hold a significant amount of data. This type of memory is volatile; if the FPGA is switched

---

[19] ALTERA - DK-CYCII-2C20N - KIT, FPGA, CYCLONE II DEVELOPMENT

[20] 3-State quad buffer MM74HC125N

[21] National Instruments PCI-GPIB

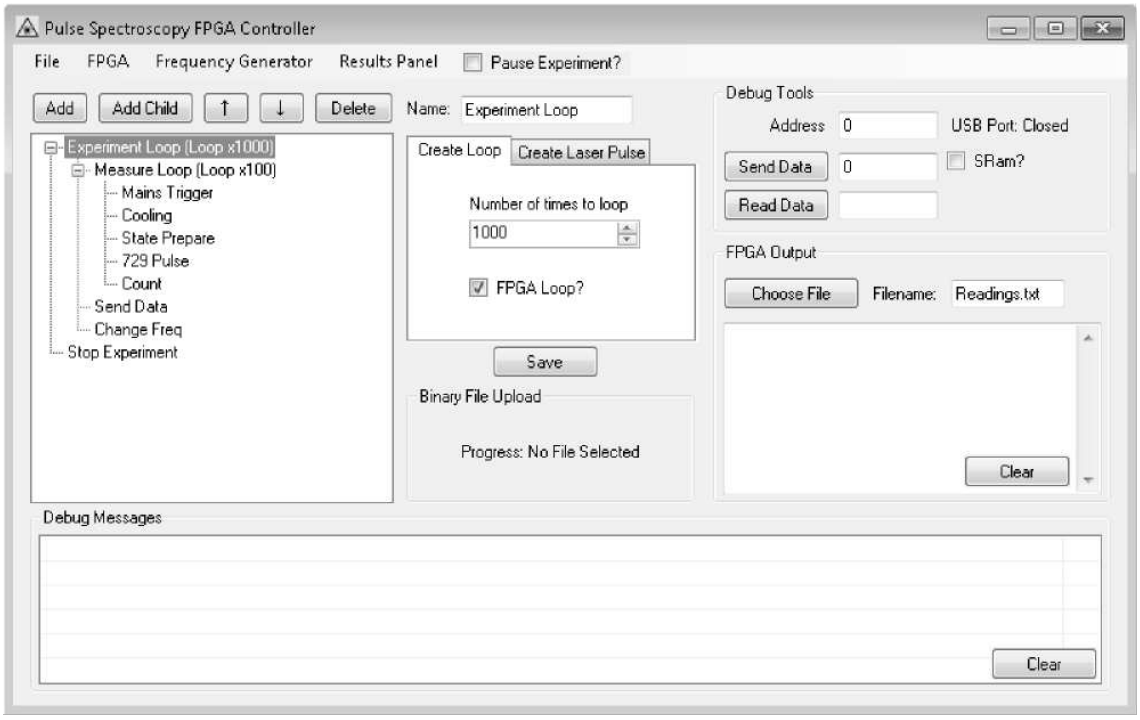

☐ Pause Experiment?

- Experiment Loop (Loop x1000)
  - Measure Loop (Loop x100)
    - Mains Trigger
    - Cooling
    - State Prepare
    - 729 Pulse
    - Count
  - Send Data
  - Change Freq
- Stop Experiment

Name: Experiment Loop

Number of times to loop
1000

☑ FPGA Loop?

Progress: No File Selected

Address 0
USB Port: Closed
Send Data 0
☐ SRam?

Filename: Readings.txt

Figure 4.21: The user interface of the program we use to setup the experiments and communicate with the FPGA and function generator.

off, the data stored in the SDRAM will be lost. Writing or reading to this type of memory takes up to 2 or 3 clock cycles. We use this type of memory to store the pulse sequence.

- Static random-access memory (SRAM) - 512 kB: not conventionally used in consumer electronics because it is relatively expensive, SRAM has several advantages over other types of memory e.g. SDRAM. For our purpose the main benefit is the speed of access: reading and writing to SRAM happens well within one clock cycle. From now on we will consider this as virtually instantaneous. This is where we store the PMT count data and laser lock information.

- Flash memory - 4 MB: This type of memory is the slowest of all those present on the development board. The memory is non-volatile, i.e. the data is not lost when the power is turned off. Flash memory has some limitations which make it unreliable for our purpose. Only a finite number of programming cycles can be implemented on the same memory bits before they become corrupted. Often the number of stable programming cycles is as high as 1,000,000 but because we repetitively change the pulse instructions and PMT data, we avoid using this memory chip.

There is much more detail that could be written about these different types of memory technologies. Many of the integrated devices are now so small that they utilise quantum tunnelling effects for their operation.

The compiled pulse sequence is received from the computer via a USB-to-TTL interface cable[22]. These data are uploaded to the SDRAM via the FPGA. The baud rate is deliberately kept low to avoid corrupted data as there are no error correction bits included in the data. The SDRAM can only be accessed in 16-bit words. Each pulse operation is stored as two of these words which are henceforth referred to as a phrase. Each phrase is split into three parts, 24-bits of timing data, allowing pulse lengths between 0 s and 0.335544300 s in 20 ns steps; 5-bits of laser data, these are essentially TTL outputs to RF switches and other devices; the remaining three bits are to tell the FPGA what operations to run during the pulse. These are:

- Mains wait - Leaves the lasers that were set on until the mains trigger is received and then moves onto the next laser pulse setting, see section 4.9.3.
- Normal - This setting turns on the lasers that are instructed to do so for the time set in the control software.
- Count - Turns the lasers on as requested and counts PMT photons saving the data along with a laser lock error code, which report if any of the lasers became accidentally unlocked in this interval, in the SRAM. This latter feature allows us to tag any data taken with the lasers unlocked so that it can be discarded in post-processing.
- Send Data - This flushes the data from the SRAM into the computer, which stores it in a text file. The transfer takes place via the USB-to-TTL cable.
- Function generator wait - This sends a signal to the computer to step the function generator frequency to the next value and waits for approximately 0.25 s for this to happen. The lasers are set to Doppler cool the ion during this period
- Start loop - This tell the FPGA that the instructions following this command and before the end loop command are to be repeated. The number of repetitions is stored in the timing data.
- End loop - This command marks the end of the internal hardware loop.
- Stop experiment - The FPGA sends a signal to the computer to say that the experiment has finished. After this point the Doppler cooling lasers are left on permanently.

---

[22] Future Technology Devices International Ltd. TTL-232R-3V3 USB to TTL Serial Converter Cable

We can store up to 8 MB/32-bit = 262144 phrases in the memory. However, using the hardware loop command we can send a standard set of instructions that has 1000 frequency steps in around only 500 commands.

4.9.3 Mains Trigger

The pulse sequence used for spectroscopy of the quadrupole transition is phase locked to the mains cycle to avoid ambient magnetic field fluctuations that would affect the atomic transition frequency, and voltage fluctuations in the electronic equipment. The trigger works by first stepping down mains voltage to 20 V amplitude on a small transformer. Then this signal is compared to ground on a simple LM311 voltage comparator. The output signal from this stage is shown in figure 4.22.

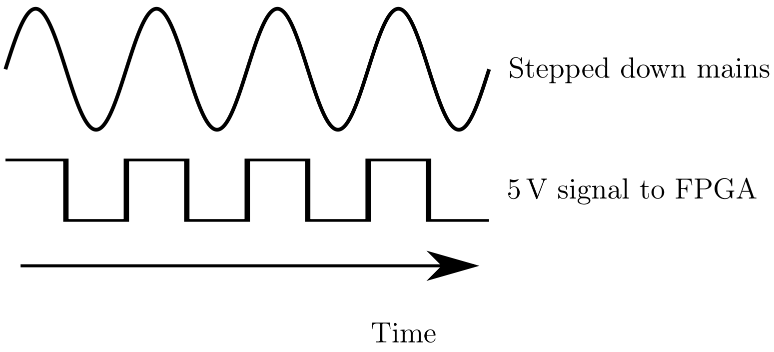

Figure 4.22: The trigger provides a high TTL signal when the mains voltage is above zero and a low signal when the mains voltage is below zero.

This signal is sent to the FPGA so that pulse sequences starts at a specific phase relative to the mains. The signal from the comparator is digitally filtered. If the output from the trigger changes, the FPGA waits to see if the signal is consistent for 3 clock cycles (60 ns) before acknowledging the trigger.

4.9.4 RF electronics

The RF electronics which control the Doppler cooling AOMs all have similar setups. For each setup a sinusoidal signal comes from a VCO[23] which passes through fixed attenuators, a homemade RF switch based on an Analog Devices ADG918 IC and a homemade voltage controlled amplifier based on a National Semiconductors LMH6505MA IC. The signals are amplified with a CATV amplifier[24] before being sent to the AOMs. The AOMs in the

---

[23] Minicircuits ZOS-100 for the 854 nm laser beam AOM, Minicircuits ZX95-200 of the 397 nm laser beam AOMs

[24] Amplifier Solutions Corporation ASC2832

Doppler cooling laser beam paths operate at a 110 MHz central frequency and the AOM in the 854 nm laser beam path operates at a 80 MHz central frequency.

The 729 nm laser is controlled from a stable, 1 Hz resolution function generator via a GPIB interface. This allows computer control of both the frequency and amplitude. The signal is sent to a high extinction RF switch[25] and RF amplifier[26] before going to the AOM. The AOM has a 250 MHz central frequency and approximately a 40 MHz tuning range. However, the power in the first order deflected beam coupled to the PM optical fibre can reduce to half over that range.

The TTL signals from the FPGA activate the RF switches; the homemade switches have an RF isolation between 28–35 dB and a 5–10 ns rise/fall time. The commercial RF switch for the 729 nm laser has a specified 100 dB isolation with a similar rise/fall time.

---

[25] Mini Circuits ZASWA-2-50DR+

[26] Mini Circuits ZHL-1-2W

Chapter 5

Coulomb Crystals

Coulomb crystals are formed when more than one ion is cooled to the solid phase. In this case the average thermal energy of the ions is much less than the energy required to overcome the Coulomb barrier for individual ions to swap positions. This is usually parametrised in the literature by the Coulomb coupling parameter, $\Gamma = e^2/(4\pi\epsilon_0 a k_B T)$; where a is the Wigner-Seitz radius defined by $4\pi a^3/3 = n_0^{-1}$, where n_0 is the number density of ions and k_B is the Boltzmann constant [51]. Different studies have shown that solid phase crystals are formed in large plasmas when $\Gamma > 172 - 178$ [52–56].

In this phase, the ions behave in a similar way to a rigid body, with the same centre of mass oscillation frequency common to all ions. Higher order motional modes are characterised by small vibrations around their equilibrium positions. The shape of these crystals is only controlled by the ratio of trapping frequencies in the axial and radial directions. In the case of a simple Penning trap, with no additional electric fields, there is no particular orientation in the radial plane and the crystal rotates. The rotation frequency for more than one ion is not fixed, and can vary anywhere between the magnetron and modified cyclotron frequency for a single ion in the same electric and magnetic fields [57]. Typically the Coulomb crystal will settle into a particular steady state rotation frequency dependent upon the parameters of the laser cooling. The rotation frequency and the number density of the particles in the crystal are related through the equation

$$n_0 = \frac{2m\epsilon_0\omega_r' \left(\omega_c - \omega_r'\right)}{q^2}, \tag{5.1}$$

where ω_r' is the rotation frequency in the laboratory frame [58]. This relation can be calculated by substituting the electric potential into Poisson's equation where the charge density is defined as $\rho = n_0 q$. Previously, two different methods have shown that it is possible to externally vary the rotation frequency; first by a laser induced torque [59] and later by applying a rotating quadrupole electric field [60, 61], colloquially called the *rotating wall* technique. The rotating wall technique distorts the radial trapping potential and phase locks the crystal rotation to a RF drive.

Forming a coupled array of particles like a Coulomb crystal in an ion trap is relatively simple when for example compared to an optical lattice. Here the ions need only to be laser cooled to around 5 mK to produce these configurations, whereas, in an optical lattice micropotentials must be formed via differential AC stark shifts in a standing wave. In the limit where the number of particles in a crystal is large, the ions become regularly spaced. For linear chains, the ions are equally spaced in a row and in 2-dimensions, planar arrays with six-fold rotational symmetry are formed [6]. In three dimensions, the picture is more complicated; crystals can form many different shapes from elongated spirals through concentric shells, to layers of planar arrays [62]. As the crystals become smaller, edge effects have to be taken into account and ion-ion spacing is no longer constant.

Coulomb crystals are not restricted to singly charged ions, they have also been observed in dusty plasmas [63] (with Coulomb coupling parameters as high as 20700 [64]). These crystals are formed of multiply charged, micron sized, clusters but form similar shaped arrays. In an astrophysical context, most of the matter in the universe is either plasma or dust particles. These crystals may help in the understanding of structures seen by telescopes, for a good review see reference [65].

Coulomb crystals have been instrumental in certain recent atomic physics experiments. Transverse optical cavity modes have been mapped out using both single ions [66] and large elongated crystals [67]. In the case of a single ion, the transverse mode was investigated by shifting the ion along the cavity mode and monitoring fluorescence. This allowed information about the light intensity to be gathered on a sub-wavelength scale. Cavity QED experiments in the strong coupling regime also become accessible with large Coulomb crystals using standard, macroscopic, mirrors. The coupling between the ions in the cavity and the cavity mode is proportional to $\sqrt{N}$, where N is the number of particles interacting with the cavity mode [68].

Another use of Coulomb crystals is to couple the internal states and collective motional modes of several ions. The Coulomb interaction allows excitation of the collective modes of the crystal via optical sidebands. This has been a key method in some of the experiments implementing quantum entanglement. In reference [2], a 14-ion linear Coulomb crystal in a RF trap is first cooled to the ground state of the centre of mass mode and then entangled using a narrowband laser beam. The ions were placed in a superposition of the form $(|0\dots0\rangle + |1\dots1\rangle)/\sqrt{2}$. It is possible to confirm that the particles are entangled by measuring the off diagonal (i.e. $\rho_{0\dots0,1\dots1}$ and $\rho_{1\dots1,0\dots0}$) elements of the density matrix [38]. An engineered quantum state of this type is commonly know as a Greenberger-Horne-Zeilinger (GHZ) state. One example application of this type of state is to increase sensitivity in spectroscopy experiments [69]. This procedure only works because the coupling between the ions is fast enough to produce collective oscillation modes. However, linear RF traps are limited to using chains of ions for this purpose. Any ions displaced from the trap axis are subject to micromotion at the RF drive frequency and are heated well above the quantum ground state. Currently this limits the number of ions that can be entangled, in a single crystal, in a RF trap.

Alternatively, using a Penning trap, both 2 and 3 dimensional crystals can be formed without any micromotion. These crystals can theoretically be cooled to the ground state for all motional modes. The readily available, harmonically confined, two and three dimensional arrays of coupled particles present a useful system for performing quantum simulation experiments [6]. As a starting point, entanglement between spin and motional states of several hundred particles in a planar two dimensional array is exploited to measure the temperature of the different modes transverse to the plane of the crystal in reference [70]. Initially the ions are placed in a superposition of all possible spin states (i.e. $\otimes_{j=1}^{N}(|\uparrow_j\rangle + |\downarrow_j\rangle)/\sqrt{2}$, where the N particles are labelled by the indices j), with a microwave pulse. A travelling wave, with angular frequency ω_{ODF}, produced from two laser fields which has a net wavevector transverse to the plane of ions is tuned close to the frequency of the different motional modes. The optical dipole force from the travelling wave induces decoherence of the spin state dependant on the temperature of the mode being investigated. The temperature of different modes can be determined by fitting the magnitude of the decoherence as ω_{ODF} is varied.

During my time in the lab we have improved our trap and laser setup to allow the production of small Coulomb crystals. Here proof of principle evidence that we can manipulate and image these crystals is reported. The work presented in this thesis will concentrate on small numbers of ions where all the ion-ion interactions can be numerically calculated on a standard computer. When the number of ions increases, the system must be approximated as a one component plasma [51] or large shell structure crystal [71] both of which have been investigated in Penning traps for many years.

In this chapter the spacing of ions, in a linear chain, in our trap, are compared to the values predicted in reference [24]. Linear chains of up to 29 ions are presented; previously only chains of up to 2 ions have been “crystallised” along the magnetic field axis in a Penning trap [9], although linear crystals have been seen in RF trap since 1987 [72]. If a linear chain is held in a trap and the axial frequency is increased, there comes a point where it is energetically favourable for the chain to develop kinks, taking up a zigzag formation. This is a well known effect which is routinely seen in for ion chains in linear RF traps, though it has never previously been observed in a Penning trap. I will compare photographs to computer simulations and infer the radial trap frequency. This information is used to examine the linear-zigzag configuration transition as a function of the number of trapped ions. Then using photos of 15 ions at a range of different trap voltages and their comparison to computer simulations it will be shown that it is possible to determine the radial trap frequency with a certain error bound. It will also be shown that this is also possible for intermediate sized crystals containing a few hundred ions as long as individual ions are still resolved. Finally, I investigate the effect of quantum J-state mixing on larger crystals of hundreds of ions.

5.1 Centre of Mass Oscillations

There are $3N$ oscillation modes for N ions. For a string of ions aligned along the trap axis, the centre of mass (COM) motion is always the lowest frequency axial mode and is independent of particle number. This oscillation frequency can be found by applying a small RF drive to one of the electrodes along the trap axis, varying its frequency and looking for a blurring of the image of a crystal on a camera as shown in figure 5.1. This occurs when the oscillating potential resonates with the crystal COM mode. Using a camera is a more sensitive detection technique than simply looking for a reduction in fluorescence using a PMT. With high enough magnification, large oscillations of the ions around their equilibrium positions can be imaged while the ions remain crystallised.

By changing the trap bias, and measuring the COM oscillation frequency we can calculate the constant of proportionality κ in the equation $\omega_z = 2\pi\kappa\sqrt{V}$ where V is the trap bias. The data plotted in figure 5.1 shows that $\kappa = 26.36 \pm 0.03\,\mathrm{kHz\,V^{-1/2}}$.

5.2 Magnetron mode instability

Section 3.4.1 shows that there is a maximum magnetron frequency, for a single ion, before the Doppler cooling lasers with a particular intensity gradient start to heat the magnetron motion. By measuring the diameter of the magnetron orbit using an amplified camera we can estimate the laser frequency relative to the atomic transition. We assume that the amplitude of the radial motion is dominated by the magnetron mode. The cooling lasers probably over saturate the transition by a factor of 2 - 5 ($\mathrm{I_{sat}} = 440\,\mu\mathrm{W\,mm^{-2}}$). In this case the interaction between laser beam and the ions is now a saturated Gaussian and not just determined by the laser beam profile which is a standard Gaussian. A saturated Gaussian can have a higher intensity gradient. Assuming that the intensity gradient is now $y_0 \approx 15\,\mu$m (y_0 is defined in figure 3.5), compared to $25\,\mu$m which should be the case when

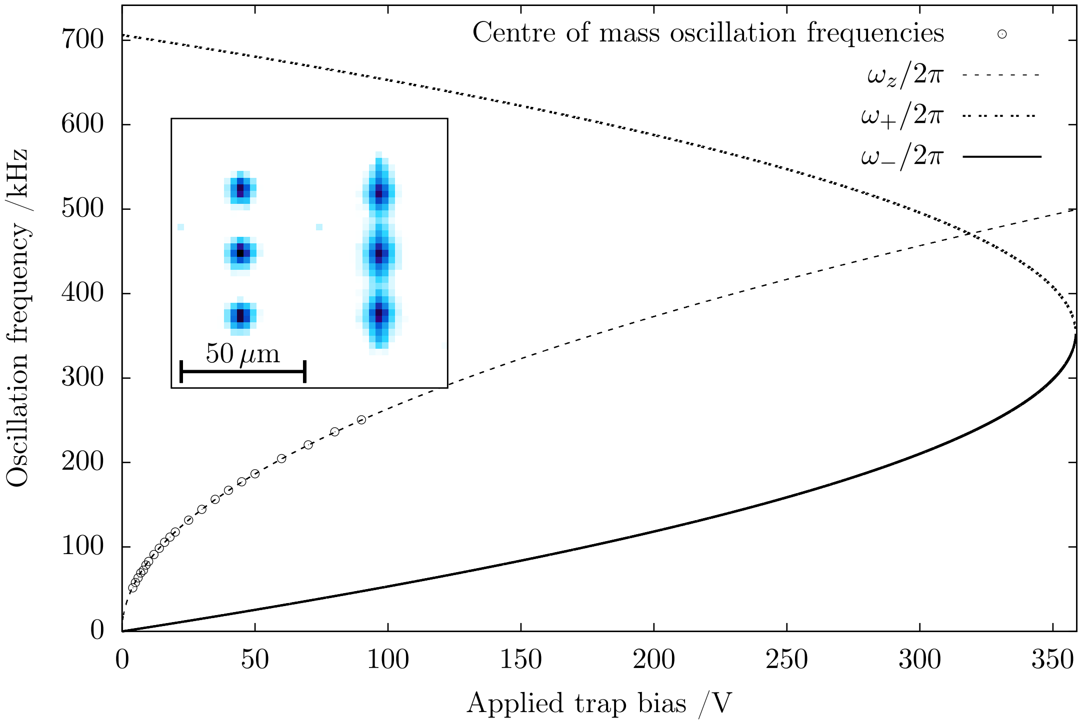

Figure 5.1: Measured axial oscillation frequency as a function of trap bias for a linear 3-ion crystal. The inferred modified cyclotron and magnetron frequencies are also shown. The axial COM motion is damped by the laser cooling and therefore accuracy in the frequency measurements is limited to around ±200 Hz. Insert shows example data. Left: a photo taken when the RF drive is off resonance. Right: photo taken when RF drive resonates with the COM axial mode.

the transition is not saturated, we should only expect good agreement between the fit and the data till the oscillation extends to around this diameter. The solid line in figure 5.2 is only fit to the data where the diameter of the magnetron motion extends to a maximum of 15 μm ($= y_0$) and is consistent with the cooling lasers being detuned by approximately half a natural linewidth. Alternatively if we include all the data up to 130 V we find a different fit (dashed-dot line). This fit does not follow the data as well for low voltages but is more consistent with the data around the region where the orbit expands dramatically. In this case the fit suggests that the laser detuning is 1–2 times the natural linewidth. These result is inferred from the data, rather than a measurement from an absolute frequency reference. The wavemeter that we use to initially set the laser frequencies is only accurate to a few hundred megahertz. When the diameter of the oscillation is greater than y_0, radial cooling is reduced and can no longer be approximated by equation 3.71. When the amplitude of the oscillation reaches around 100 μm the ion samples the entire width of the beam and the size of the orbit reaches some stable equilibrium.

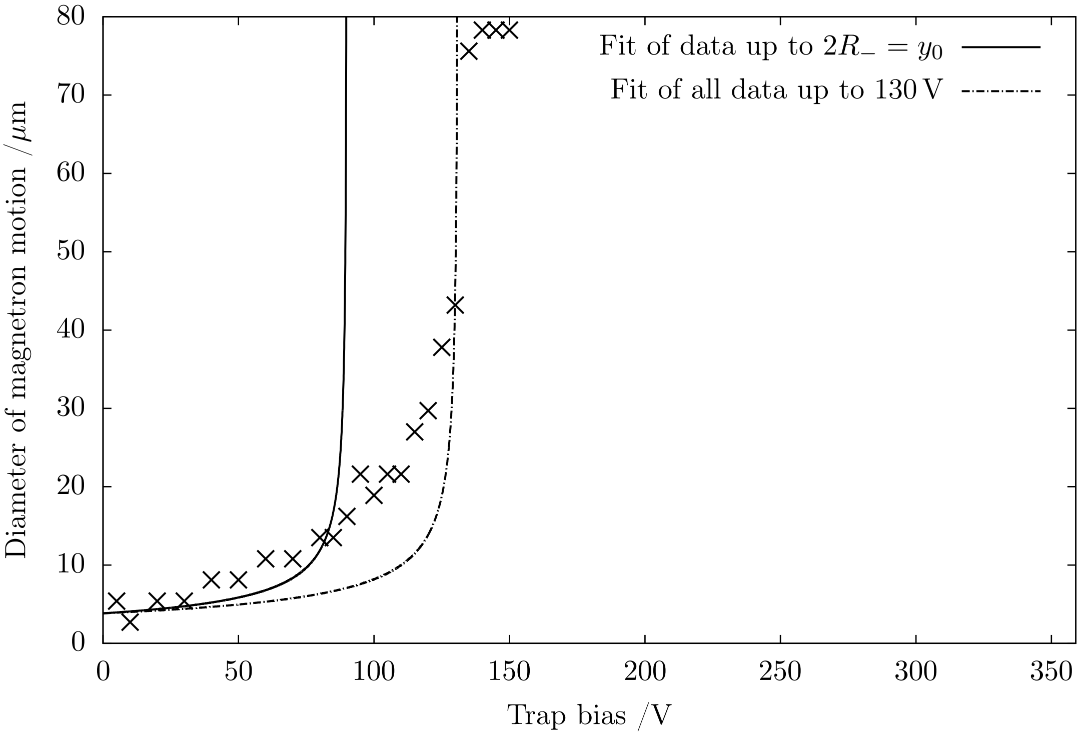

Figure 5.2: The amplitude of the radial motion of a single ion (×) fit against equation 3.74b for different data ranges (see text for details). The diameter of the motion is measured using an amplified camera at different trap bias settings. The imaging magnification (3 ± 0.1) and pixel size ($8\,\mu$m), limit the accuracy of the measurement to an error of around $\pm 1\,\mu$m.

5.3 Motion in a Rotating Frame

The laboratory frame is not the natural frame in which to consider the motion of an ion in a Penning trap. If instead we move into a frame rotating at $\omega_c/2$ the circular motion which couples the two radial co-ordinates, x and y, is removed and a simple harmonic motion in only one co-ordinate is retained. However, as is shown below, when there are two or more ions present they can rotate even in this frame. The standard result for the acceleration of a rigid body in a rotating frame, at a constant frequency, is

$$\ddot{s}_r = \ddot{s} - 2\Omega \times \dot{s} - |\Omega|^2 s, \tag{5.2}$$

where $\ddot{s}_r$ and $\ddot{s}$ are accelerations in the rotating and lab frames and Ω is the rotation frequency. The penultimate term in equation 5.2 relates to the Coriolis force and the final term relates to the centripetal force. If we substitute equation 2.7 and $\Omega = \omega_c/2$ into equation 5.2 we find,

$$\ddot{s}_r = -\left(\frac{\omega_c^2}{4} - \frac{\omega_z^2}{2}\right) s = -\omega_1^2 s. \tag{5.3}$$

This transformation has removed any rotation due to the magnetic field and essentially turned this system into a harmonic potential in 3-dimensions where the trapping frequencies in the x and y directions are degenerate. We can rewrite the potential energy of the system in the rotating frame as

$$V = \frac{m}{2}\sum_{n=1}^{N}\left[\omega_z^2 z_n^2 + \omega_1^2\left(x_n^2 + y_n^2\right)\right] + \frac{e^2}{8\pi\epsilon_0}\sum_{n,m\neq n}\frac{1}{r_{nm}}, \tag{5.4}$$

where the Coulomb repulsion of N ions has now been included. The indices n and m sum over the number of ions, and $r_{nm} = \sqrt{(x_n - x_m)^2 + (y_n - y_m)^2 + (z_n - z_m)^2}$ is the interparticle spacing. The directions x_n and y_n are arbitrary in the case of a Penning trap with no perturbing electric fields. If the crystal rotates in this frame at ω_r we can move into another frame where the ions are now stationary. To relate the frame where the ions are stationary and the laboratory frame, we can use the simple conversion, $\omega_r' = \omega_c/2 - \omega_r$, where ω_r' is the rotation frequency in the laboratory frame; this assumes that the rotation frequency in the laboratory frame is always less than $\omega_c/2$. The radial trap frequency can be written as

$$\omega_T^2 = \omega_1^2 - \omega_r^2 \tag{5.5}$$

which can be derived by considering the total energy of the system in the two different frames. Now the potential energy for the system can be written as

$$V = \frac{m}{2}\sum_{n=1}^{N}\left[\omega_z^2 z_n^2 + \omega_T^2\left(x_n^2 + y_n^2\right)\right] + \frac{e^2}{8\pi\epsilon_0}\sum_{n,m\neq n}\frac{1}{r_{nm}}. \tag{5.6}$$

When $\omega_r \neq 0$, or equivalently $\omega_T < \omega_1$, the maximum voltage at which the configuration is stable is reduced to $\frac{V_{\max}}{V_0} = 1 - \left(1 - 2\omega_r/\omega_c\right)^2$, where V_0 is the maximum stable bias for a single ion in a Penning trap with the same magnetic field.

5.3.1 Laser beam torque

The axial COM oscillation frequency, ω_z, is set directly by the trap potential. In our experiment the rotation frequency is set by the radial laser cooling beam which essentially applies a torque to the crystal. We do this by offsetting the laser beam from the centre of the Coulomb crystal. This method has been shown to vary the rotation frequency of a large non-neutral plasma from ω_- to ω_+ [57].

As the crystal becomes smaller, the torque that can be applied to the ions, which is proportional to distance between the centre of rotation and the laser beam, is reduced. When the diameter of the crystal in the radial plane is less than the width of the laser beam, a torque can be applied via an intensity gradient. This situation becomes very similar to laser cooling of a single ion described in section 3.4.1. Now the rotation frequency is not fixed and depends on unstable laser parameters such as intensity, frequency and beam position. The work in this thesis depends on the radial cooling beam to set the rotation frequency, hence the radial trap frequency.

5.4 Linear Ion Chains

By relaxing the axial trapping potential in a Penning trap with a fixed magnetic field, the ions form linear Coulomb crystals aligned along the trap axis. For small numbers of ions the infinite range $1/r$ Coulomb repulsion leads to a non-linear ion-ion spacing. By solving the N coupled simultaneous equations 5.4, we can predict their positions. These equations can be solved analytically for chains of up to 3 ions however for larger numbers of ions the equations must be solved numerically [24]. The solutions are tabulated in reference [24] for up to 10 ions.

The right-hand-side of figure 5.3 is a collage of photos of 1 to 9 ions aligned along the trap axis. The numerical solution to equations 5.4 have also been plotted as circles. The experimental data fit these theoretical points well, suggesting that the harmonic trapping term is dominant. We can also cool larger strings of ions. The left-hand-side of figure 5.3, shows a photo of a 29 ion crystal. Previously only two-ion linear crystals have been shown to align along the axis of a Penning trap [9]. The ions at the edges of the 29 ion chain, which is $505 \pm 15\,\mu$m long, appear less intense than the central ions. If the axial beam was not aligned properly it may not have good enough a spatial overlap to saturate the laser cooling transitions for the outer ions. Also, as ions are held further from the centre of the trap, they become more susceptible to electrical noise on the electrodes. This may also induce oscillations in the crystals shown in figure 5.3.

The radial cooling beam width ($1/\mathrm{e}^2$ diameter is approximately $100\,\mu$m) is too small to provide any laser cooling at the edges of the long string of ions in figure 5.3. The axial cooling beam heats the radial motion of the ions through photon recoil. In cases where the crystal is made to extend even further along the trap axis, it is possible to see a larger radial motion of the end ions compared to the ions in the centre of the crystal.

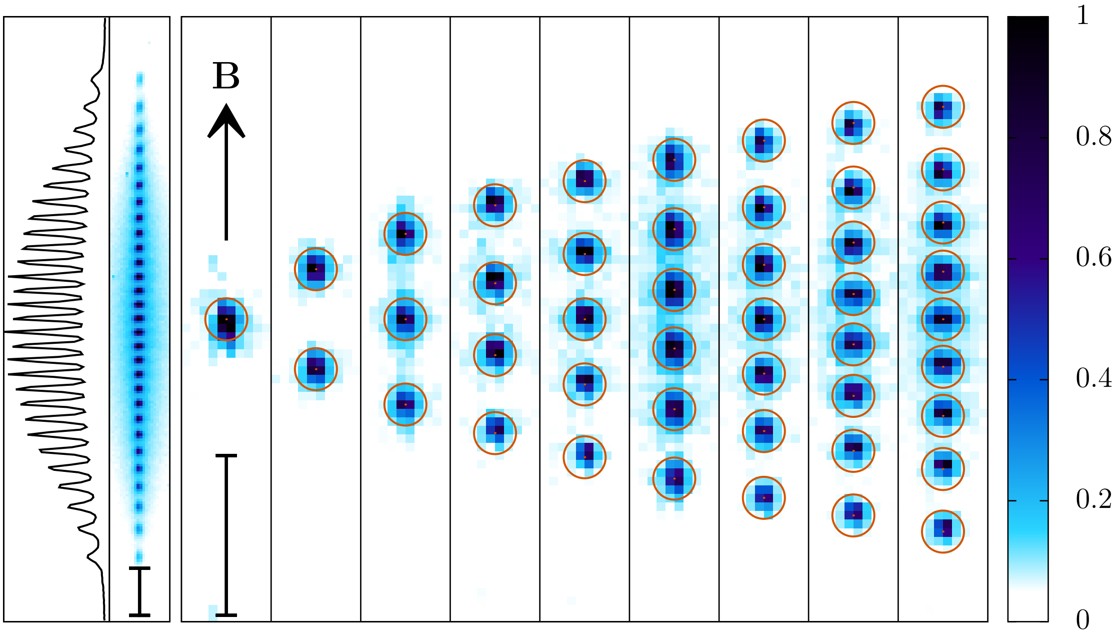

Figure 5.3: Right: collage of linear crystals of 1–9 ions. The trap bias is set at 8.95 V for all of the photos. Each photo is an accumulation of twenty 1 second exposures and the maximum intensity in each photo is normalised to unity. Each pixel is equivalent to $2.65 \pm 0.15\,\mu$m in the centre of the trap. The circles around the ions are the theoretically calculated positions, from reference [24], and not from a fit to the data. Left: a chain of 29 ions and their intensity profile. The ions at the end of the chain are less bright than the centre ions probably because they are not as well overlapped with the laser beams. The bars at the bottom of the photos both represent a length of $50\,\mu$m.

5.5 Higher dimensional Coulomb crystals

The shape of two and three ion crystals in a Penning trap is determined analytically in references [73, 74]. However, only numerical analysis is possible for larger numbers of ions. To progress further, I wrote a simple script in the Matlab programming language to find the equilibrium positions for the ions. The same program also displays an image which should be similar to what we see on the camera after a long exposure.

The magnetic field, number of ions and axial (ω_z) and radial (ω_T) trap frequencies are input into the program. The ions are originally given random positions in space for the three dimensions. The random positions should help avoid any unstable equilibria which the simulation may find. For the first ion, the net force due to the Coulomb repulsion from all the other ions and the trap potential is found. This is repeated for all the other ions to find the magnitude and direction of the net force. Now the program takes a small time step. The position of each ion is moved in the same direction as the force from the previous step. The magnitude of the force determines how far to move a particular ion. The new positions are then used as starting points and the process is iterated several thousand times to find the equilibrium positions.

At the end of this process, each ion has a position in three dimensional space where the total force on all the ions is minimised. The script could easily be optimised to stop looping if the total force on all the ions drops below a certain threshold but this modification has not been implemented to produce the results in this thesis.

In the laboratory frame, the crystallised ions are rotating around the trap axis. When we take a photograph in the experiment, fluorescence from the ions appears to be smeared out because the exposure is much longer than a single rotation period. The ions are cooled to a few milli-Kelvin and hence have fixed relative positions so their orbits are circular. When this motion is projected onto the plane imaged by the camera, it is easy to see that an ion appears to spend more time at the extrema of its apparently sinusoidal motion. We can simulate what kind of an image we expect to see, assuming that the fluorescence rate is constant, by applying the formula

$$I \propto \arcsin\left(\frac{X+\Delta X/2}{r}\right) - \arcsin\left(\frac{X-\Delta X/2}{r}\right), \tag{5.7}$$

where I is the intensity incident on a particular pixel on the camera, X is the position of the pixel relative to the centre of the image, ΔX is the width of a pixel and r is the radius of motion for a particular ion [9]. The image can be simulated by summing the fluorescence we expect to observe from each individual ion, assuming that they all interact equally with the cooling lasers. This assumption may be flawed but it is used anyway. For example, if the orbit of an ion has a radius of $10\,\mu$m we expect the Doppler shift of the cooling transitions, when the rotation frequency in the lab frame equals $\omega_c/2$, to be

$$\begin{aligned} \Delta f &= \frac{(\omega_c/2) \times 10\,\mu\mathrm{m}}{c} f_0 \\ &\approx 55\,\mathrm{MHz}, \end{aligned} \tag{5.8}$$

where c is the speed of light and f_0 is the frequency of the cooling transitions (approximately 755 THz).

The image is then filtered with a Gaussian point spread function commensurate with our imaging system. This is simple using the functions provided by Matlab. Figure 5.4 shows an example of an image we would expect to observe when seven ions are formed in to a linear string, a zigzag if there was no rotation and a zigzag when rotation in the radial plane is taken into account.

By maintaining the same axial frequency (which is solely dependent on the trap bias) but altering the radial frequency input to the computer code to match photographs from the experiment and images from the simulation, we can find the rotation frequency, ω_r, of the

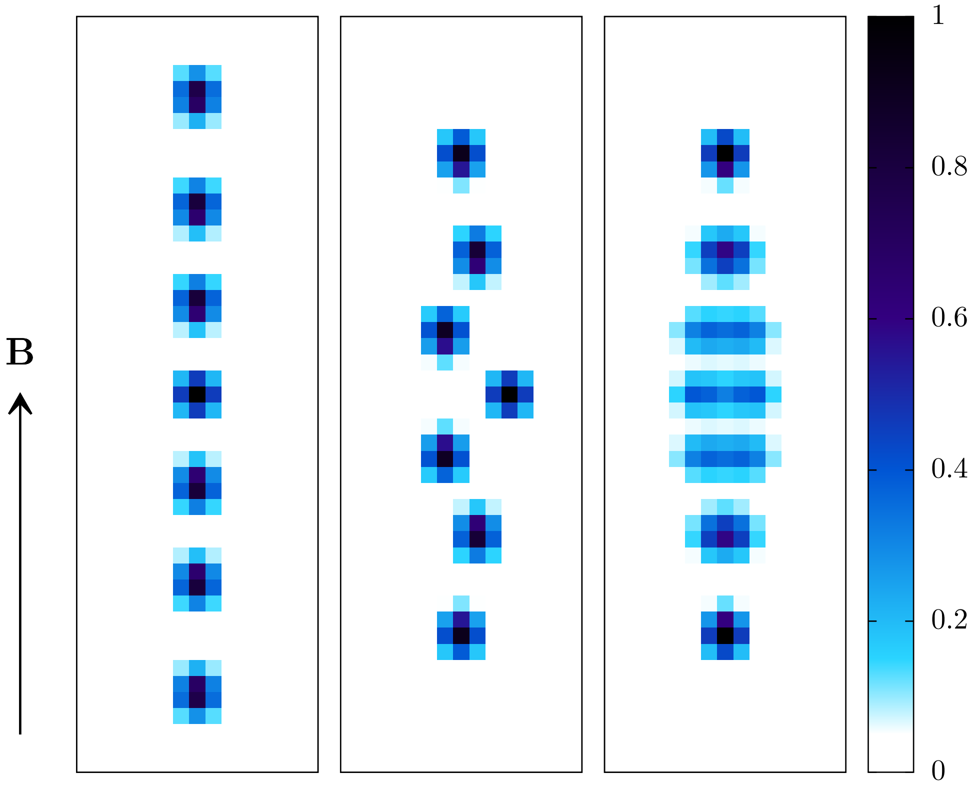

Figure 5.4: Simulated images for seven ions. Left: when the ions form a string, they appear in a line from our point of view even though they are rotating. Centre: when the axial frequency is increased the ions form a zigzag shape. If the camera we used to image these ions could be gated in phase with the crystal rotation we would observe an image similar to the one shown in the centre. Right: a simulated image for the ions in a zigzag configuration taking into account the fact that we are viewing the crystal while it rotates.

crystal.

The first non-linear shape which we observe is a zigzag geometry. Reference [75] determines the ratio of axial and radial trapping frequencies where the linear to zigzag transition takes place. By calculating this ratio for a wide range of ion string lengths, an empirical scaling law to predict the the transition is inferred.

In a linear chain, all the ions lie along the trap axis. However, from simple arguments we can see that if there is a zigzag pattern none of the ions can lie along the trap axis. As proof, consider the case where only a few central ions lie off axis. The transverse electrostatic repulsive forces from these ions in the chain may balance perfectly for a single ion further along the chain. However, the next ion along has a different forces acting on it because the Coulomb repulsion is a function of distance. Hence, we can see that it would be impossible for a few ions to be off axis in the centre of the chain and the remainder to lie exactly along the trap axis [76].

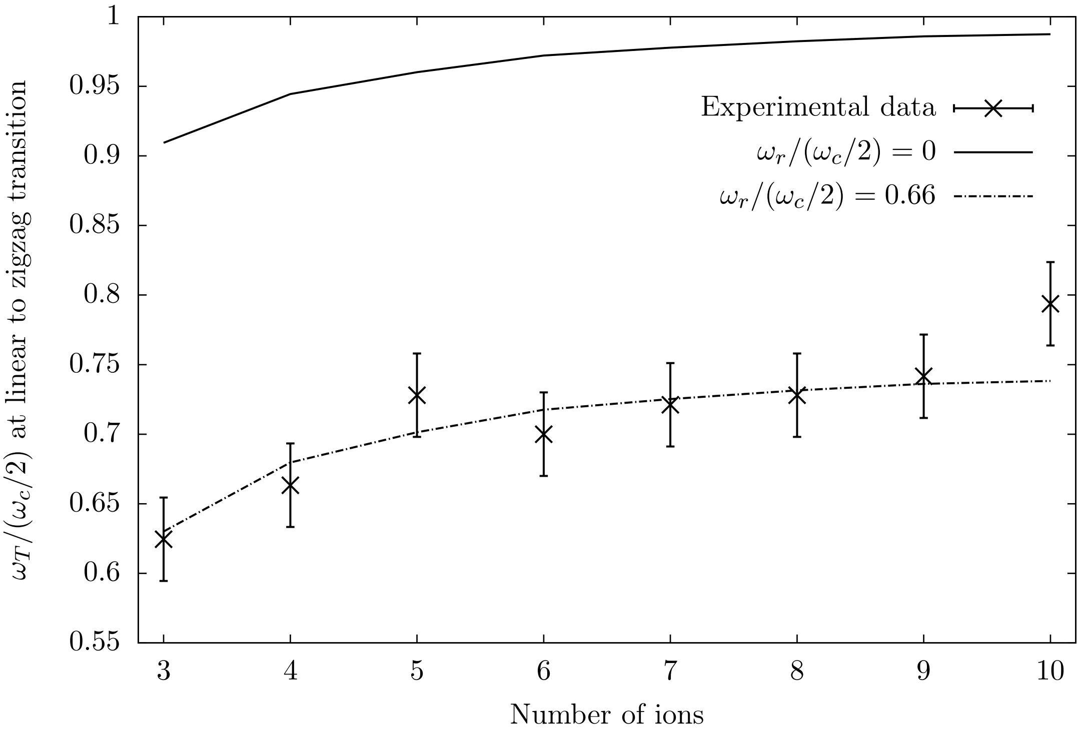

Figure 5.5: By measuring the trap bias when a linear to zigzag transition occurs we can predict the radial trap frequency. This figure shows the frequency ω_T inferred from the experimental data. These data are consistent with $\omega_r = 0.66 \pm 0.05$. The frequency ω_T is also calculated at the transition between linear and zigzag crystal configurations for the theoretical case where $\omega_r = 0$.

Here, the radial trap frequency, ω_T, is determined from the linear to zigzag configuration transition voltages and comparison to computer simulation. We input the axial oscillation frequency, where the transition was observed, which is fixed by the trap bias and the radial frequency is varied in the program until the linear to zigzag transition is found. Figure 5.5 shows the radial trap frequencies at the zigzag transition and the predicted frequencies if the crystal was stationary in the frame rotating at $\omega_c/2$. However, the data is more consistent with the crystals consisting of different numbers of ions rotating at angular frequency $\omega_r/(\omega_c/2) = 0.66 \pm 0.05$.

We can also compare photos of a fixed number of ions, at various trap biases, to computer simulations. Figure 5.6 shows a continuum of images for 15 ions from a linear string to a flat two dimensional rotating pentagon-decagon structure. The images are titled with axial trapping frequency in units of $\omega_z/(\sqrt{2}\omega_c/2)$. For a single ion, all the stable axial trap frequencies, in these dimensionless units, are within the range zero to one. They are compared to the closest matching simulations with a variable radial trap frequency, ω_T.

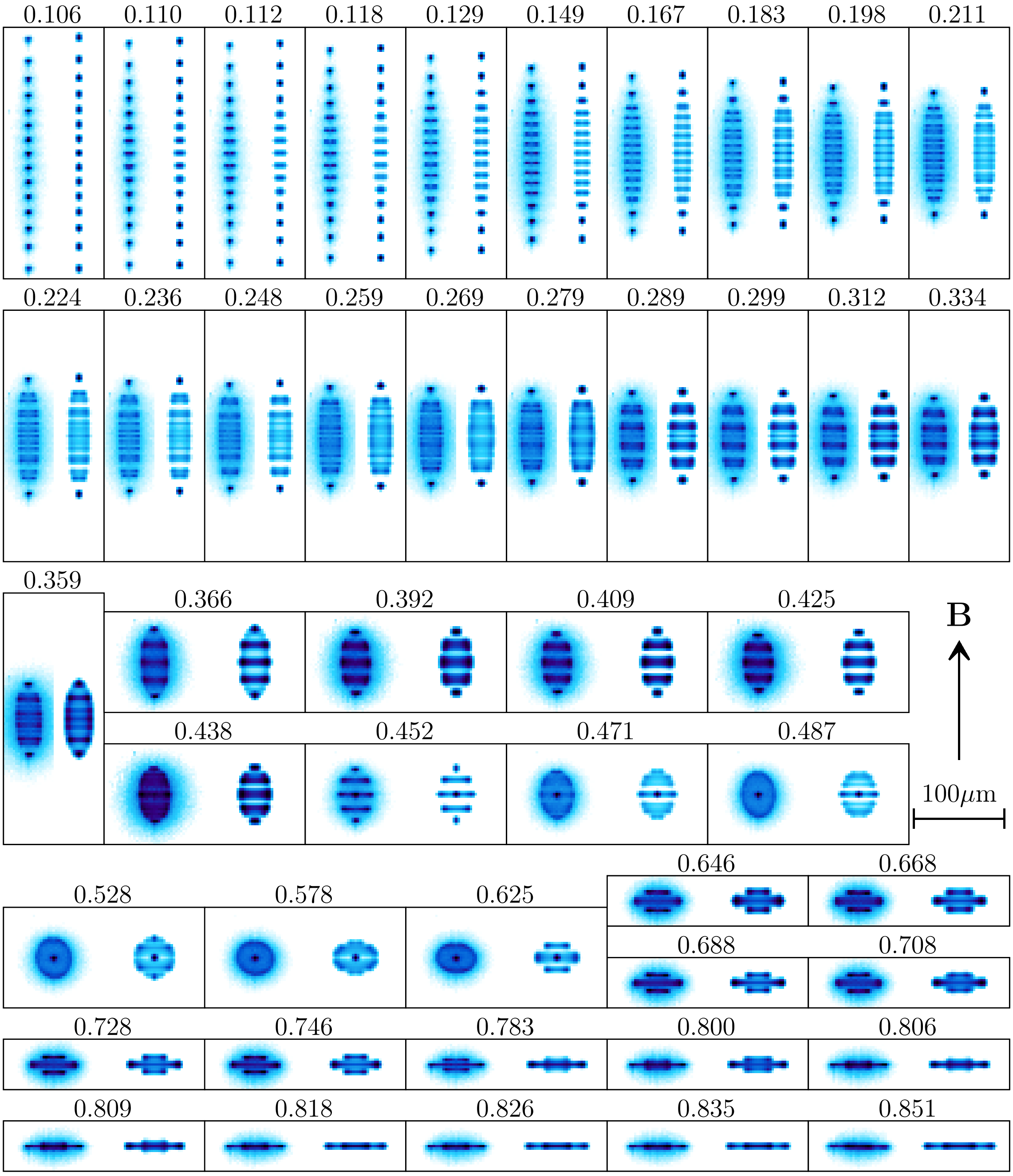

Figure 5.6: Left: photographs of 15 ion Coulomb crystals. Right: the closest matching computer simulations. The images are titled with axial trapping frequency in units of $\omega_z/(\sqrt{2}\omega_c/2)$. In all the images, the magnetic field is in the vertical direction and the horizontal and vertical scales are equal and given by the bar on the right hand side. The maximum intensity in all the photographs is normalised to 1 and come from an accumulation 40 exposures each with a 1 s shutter time. The magnification in all the images is 3.0 ± 0.1. The colour scale is the same as in figure 5.3.

To find the closest matching simulation to the photos in figure 5.6, the radial trap frequency was manually optimised. The axial frequency and the deduced radial trapping frequency, ω_T, are plotted against each other in figure 5.7 for the images shown in figure 5.6. By fitting these data to

$$\left(\frac{2}{\omega_c}\right)^2\left[\omega_T^2+\frac{\omega_z^2}{2}\right]=1-\left(\frac{\omega_r}{\omega_c/2}\right)^2, \tag{5.9}$$

we should be able to find ω_r, the rotation frequency in the frame rotating at $\omega_c/2$. Equation 5.9 can be derived by substituting equation 5.5 into equation 2.11. This is the same equation as a circle in suitably scaled coordinates.

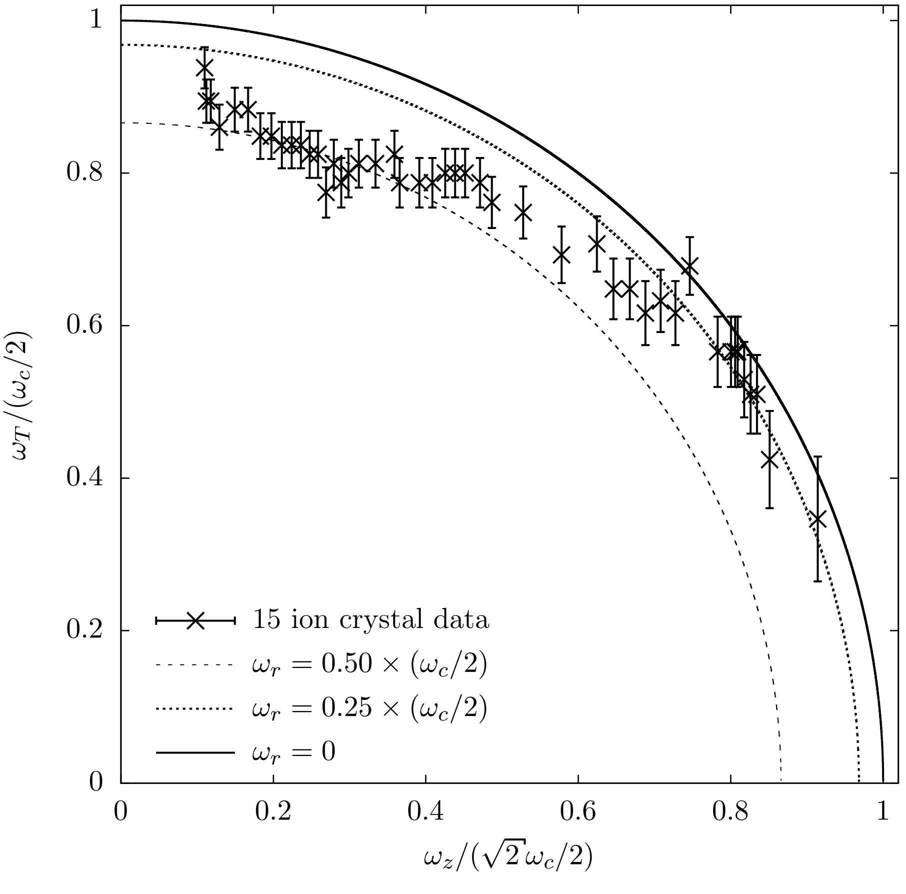

Figure 5.7: For each of the images in figure 5.6 the axial trapping frequency is plotted against the radial trapping frequency used to produce the simulated images. This is essentially the stability diagram for a Penning trap. Lines of constant rotation frequency, ω_r, are plotted for comparison. The error bars are derived from how accurately the radial trap frequency can be determined by comparison to computer simulations.

Figure 5.7 shows that the rotation frequency of the crystals, ω_r, appears to decrease towards higher axial trap frequencies from around $0.5 \times \omega_c/2$ to $0.25 \times \omega_c/2$. However, is it much harder to deduce rotation frequencies when the crystal is in one of the two extreme configurations. The radial trap frequency has no effect on a linear chain and the axial frequency has very little effect on an oblate ellipsoid (pancake) shape crystal. The configuration of the crystals changes much less in the range $0.5 < \omega_r/(\omega_c/2) < 1$ than the range $0 < \omega_r/(\omega_c/2) < 0.5$. This can be seen graphically in figure 5.7. The area of the sector enclosed by the lines $\omega_r/(\omega_c/2) = 0.5$ and $\omega_r/(\omega_c/2) = 0$ is much less than the area from the origin to the line where $\omega_r/(\omega_c/2) = 0.5$.

5.6 Larger Crystals

The strong coupling between ions in a Coulomb crystal and the broad laser beam profile in our experiment allows us to crystallise larger numbers of ions than previously discussed in this chapter. As the numbers of ions increases more intermediate configurations become possible. However, what appeared as configuration transitions for small numbers of ions, are no longer so clear. For example, a three ion zigzag shape crystal transforms to a triangle rotating in the radial plane when $\omega_z = \omega_T$. However, for large numbers of ions the first shape after a zigzag is a spiral of varying aspect ratio, followed by a shell configuration, without any kind of layered structure, until the regime where $\omega_z \gg \omega_T$ is reached.

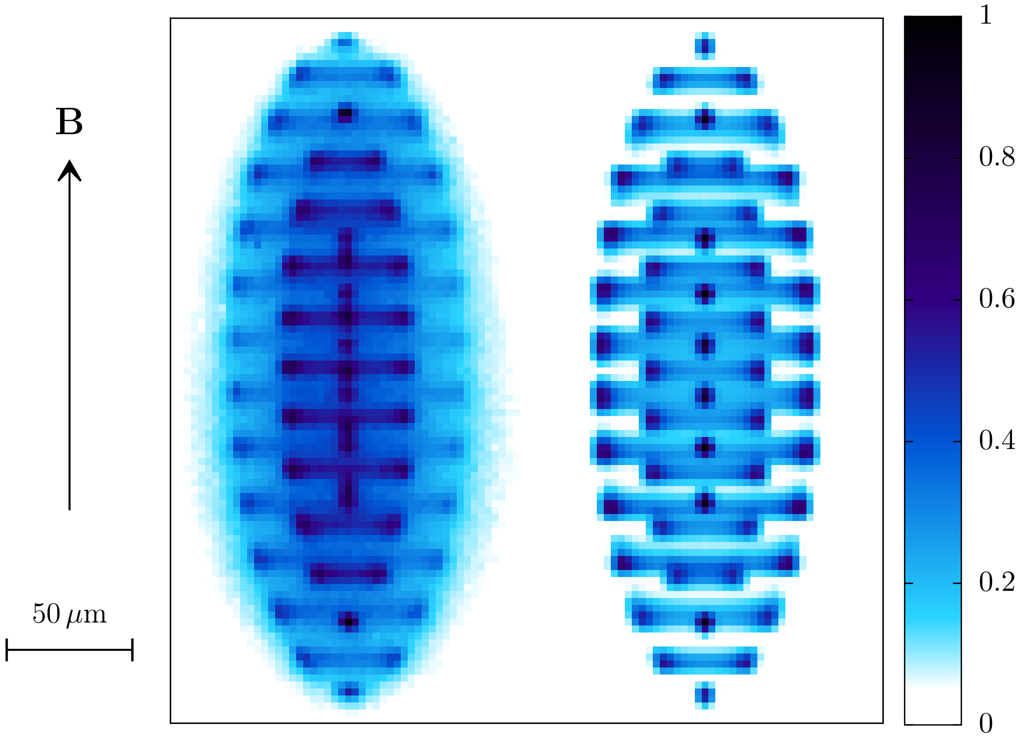

Figure 5.8: A photo of a large Coulomb crystal and a simulation of a similar shaped crystal. The simulated image is for 174 ions where $\omega_z^2/(2\omega_T^2) = 0.146$.

Figure 5.8 shows a photograph of a larger crystal in our trap as a demonstration that we can crystallise and clearly image larger numbers of ions. It is not possible, with just a single side-on photograph, to determine the exact number of ions in a three dimensional Coulomb crystal of this size. The simulations suggest that the crystal in the photograph contains 174 ± 4 ions in a trap potential where $\omega_z^2/2\omega_T^2 = 0.146 \pm 0.010$. If the number of ions and ratio of trap frequencies is varied within the errors provided, the simulated crystal maintains the correct gross structure (number of planes of ions, number of central ions, etc.) and the correct aspect ratio. By altering either of these parameters further, it is possible to observe a clear deviation from the crystal in the photo. This is roughly the limit for the numbers of ions that can be simulated by my simple Matlab code. It is unfavourable to increase the number of ions further as the number of calculations required scales with the square of the number of particles. Much more sophisticated molecular dynamics codes exist if larger crystals are being investigated. For example, a computer program called Protomol can compute the interaction between 100000 ions, including ions of different species [77].

It is difficult to align more than 50 ions along the axis of the trap because it would require the ratio of the axial and radial trap frequencies, $\omega_z^2/(2\omega_T^2)$, to approach zero. In this case, the crystal would become susceptible to melting during collisions with background gas molecules and noise on the electrodes which may couple to vibrational modes of the crystal.

5.6.1 Effect of quantum J-state mixing in Coulomb crystals

In the frame where the crystal is stationary the radial cooling beam rotates around at $\omega_c/2 - \omega_r$. However, the axial cooling beam has a definite angle of incidence relative to the trap axis (it is parallel). Therefore, when the ions are fluorescing there is a net force imparted on the crystal proportional to the number of photons scattered from the axial cooling beam. If some ions decay to a non-fluorescing *dark* state and no longer interact with the axial laser cooling beam, they are not affected by the light pressure. This is clearly a state dependent force. We can engineer a situation like this by blocking the repumping laser which stimulates the $\mathrm{D}_{5/2} \leftrightarrow \mathrm{P}_{3/2}$ transition. Now, any ions that are shelved in the $\mathrm{D}_{5/2}$ level, via quantum J-state mixing, see section 4.1.1, remain dark for approximately 1 s before decaying to the ground state and returning to the cooling cycle. The axial cooling beam pushes the fluorescing ions in the same direction as the laser light. This can be directly observed by taking a time averaged photo of a Coulomb crystal with the 854 nm laser beam blocked.

Figure 5.9 shows a photo of a large Coulomb crystal with and without 854 nm laser light to repump the $\mathrm{D}_{5/2}$ state. The bright ions are pushed by the axial laser beam. The crystalline

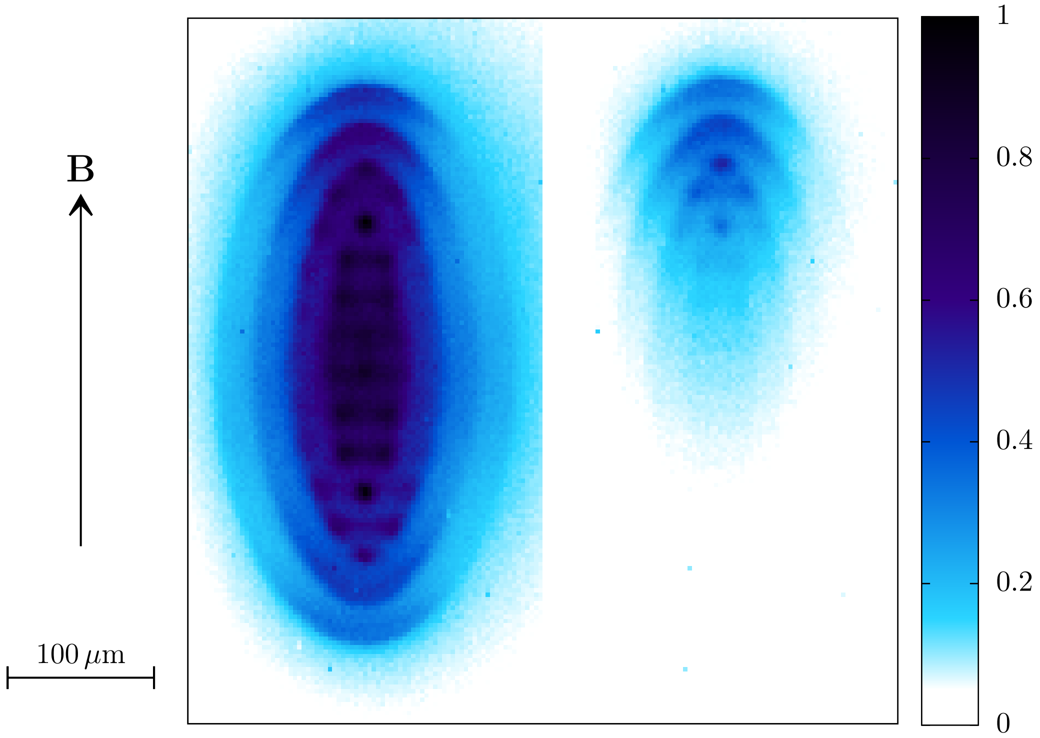

Figure 5.9: The effect of quantum J-state mixing is clearly shown on this Coulomb crystal. The photo on the left shows a Coulomb crystal when the $D_{5/2}$ state is repumped and the photo on the right is taken when the repumping laser is blocked. The photos are accumulations of 60 × 0.5 s exposures, long enough for the ions to spontaneously decay back to the ground state around 30 times on average.

structure is still clearly visible suggesting that the dark ions are sympathetically cooled to the solid phase.

Far above saturation we expect the ion to have a $\gamma/2$ fluorescence rate, for a two level system. By including the whole level system including two $S_{1/2}$, two $P_{1/2}$ and four $D_{3/2}$ states we should only expect a $\gamma/4$ fluorescence rate. Including another factor of 1/2 because the laser cooling frequency is detuned below the atomic resonance we should expect $\gamma/8 \approx 1.7 \times 10^7$ photons s^{-1} to be emitted. Using the theory in reference [78] we should expect 7.1×10^5 photons before decaying to the $D_{5/2}$ state on average. Therefore the ratio of fluorescence when the 854 nm laser is blocked and unblocked is given by

$$\frac{7.1/170}{1.2 + 7.1/170} = 0.034, \tag{5.10}$$

where 1.2 s is the lifetime of the $D_{5/2}$ state. The ratio of the fluorescence in the two photos in figure 5.9 when corrected for background laser scatter is 0.23. One possible explanation for the discrepancy is that the $D_{5/2}$ level is repumped by amplified stimulated emission in the 866 nm laser. However this seems unlikely because the dichroic mirror combining the two repumping lasers has 36 dB attenuation (measured) for 854 nm light in the 866 nm laser beam. An alternative view might be that the photograph on the left hand side of figure 5.9 is not fluorescing at the rate predicted above. This could be because axial beam does not saturate ions throughout the whole crystal, only the central 100 μm. The radial beam may not interact with the outer ions either due to the Doppler shift. The ions in the outer shell are approximately $r = 100\,\mu$m from the centre of rotation in the radial plane. Assuming the crystal rotates at $\omega = 2\pi \times 100\,$kHz in the lab frame, this should shift the laser cooling frequencies by $\pm\omega r f_0/c \approx 160\,$MHz. The shift for the repumping lasers is approximately 72 MHz. This could reduce the fluorescence rate at the left and right of the image and be the main reason why the outer most shell of ions is not clearly visible apart from at the top and bottom of the crystal.

Chapter 6

Motional Sideband Spectroscopy

The motion of a Doppler laser cooled ion in a Penning trap can be well approximated by an harmonic oscillator. It can be shown that the quantum energy levels in such a confining potential are equally spaced. Motional sidebands can be observed when the trap frequency is greater than the linewidth of a probe optical or RF atomic transition. The energy level structure in $^{40}\mathrm{Ca}^+$ ions has an electric quadrupole allowed transition between the $\mathrm{S}_{1/2}$ and the metastable $\mathrm{D}_{5/2}$ levels with a natural linewidth of approximately 1 Hz [40]. In this chapter I will show that we have observed both axial and radial motional sidebands using this 729 nm narrow linewidth transition in a single calcium ion in a Penning trap.

Motional sidebands on atomic transitions have been observed in several systems. They were first detected, via microwave spectroscopy, in a cloud of He^+ ions stored in a quadrupole RF trap [79]. The first observation of optical sidebands was performed using a single Hg^+ ion at NIST [80]. Since then, optical sidebands have been observed in neutral atoms stored in an optical lattice [81] and a micromechanical oscillator [82]. For reference, the temperature of the centre of mass mode and several higher order modes in a 2 dimensional Coulomb crystal in a Penning trap has been measured by tuning lasers to induce an optical dipole force resonant with a motional mode [70]. For many experimental groups, the observation of motional sidebands quickly leads to resolved sideband cooling. Again, this was first demonstrated at NIST with a single Hg^+ ion [16].

A theoretical framework for the interaction between laser light and the external states is described in section 3.2. By fitting the shelving probability of the sidebands to equation 3.55 we can estimate the temperature or, more generally, the population distribution of the trapped ion. In the Lamb-Dicke regime, the average motional state can be calculated by the approximation $\bar{n} = P_{-1}/(P_{+1} - P_{-1})$, where P_{-1} and P_{+1} are the shelving probabilities of the first lower and upper sidebands, assuming these transitions are not saturated.

Resolved sideband cooling has allowed significant progress in atomic frequency references and quantum computing using trapped ions. Sideband cooling often increases the occupation of the ground state of motion to greater than 99 % probability. Doppler shifts are then reduced so that they are no longer the dominant sources of error in atomic frequency standards [83].

Many quantum computing algorithms or quantum simulation protocols require that the motional state of the particles is initially prepared with a well defined distribution. For example to perform high contrast Rabi oscillations a trapped particle must be prepared in a Fock or number state. Many other well defined coherent superposition states have been created, but always starting from a ground state cooled ion, for some examples see reference [84].

This chapter will first describe the experimental procedure used to perform spectroscopy on the $\mathrm{S}_{1/2} \leftrightarrow \mathrm{D}_{5/2}$ transition. It will also illuminate some of the challenges to determining the internal state of the ion due to quantum J-state mixing. Finally, the preliminary spectra of the axial and radial motions of a single $^{40}\mathrm{Ca}^{+}$ ion in a Penning trap are displayed. The quality of the data limits the accuracy of the measurement of the average motional occupation number, $\bar{n}$ to no better than a factor of 2 or 3.

6.1 Pulse sequence

The control hardware and software repeatedly pulses different lasers on and off to a well defined sequence to build up a spectrum of the transition. The spectrum includes vibrational sidebands around the carrier so the frequency range that must be scanned is many times that of the transition linewidth.

The pulse sequence used to measure a spectrum is shown in figure 6.1. Each pulse performs a certain task.

- **Mains wait:** Takes over when the previous pulse sequence has finished and carries on Doppler cooling until the mains voltage increases above ground. This is to ensure that the pulse sequence is phase locked to the mains cycle.
- **Doppler Cooling:** Standard laser cooling with both 397 nm Doppler cooling lasers and the two repumping lasers. The detuning and power of the lasers in this pulse determines the ion temperature for the spectroscopy run.
- **State preparation:** Optical pumping into one of the $\mathrm{S}_{1/2}$ magnetic sub-levels. Achieved by simply turning off one of the 397 nm lasers.

- **729 nm pulse:** Creates a superposition of the $S_{1/2}$ ground state and the metastable $D_{5/2}$ state.
- **Detection:** All the standard Doppler cooling lasers, except for the 854 nm laser, are turned on again to stimulate atomic fluorescence and determine whether the ion has been shelved or remains in the ground state.

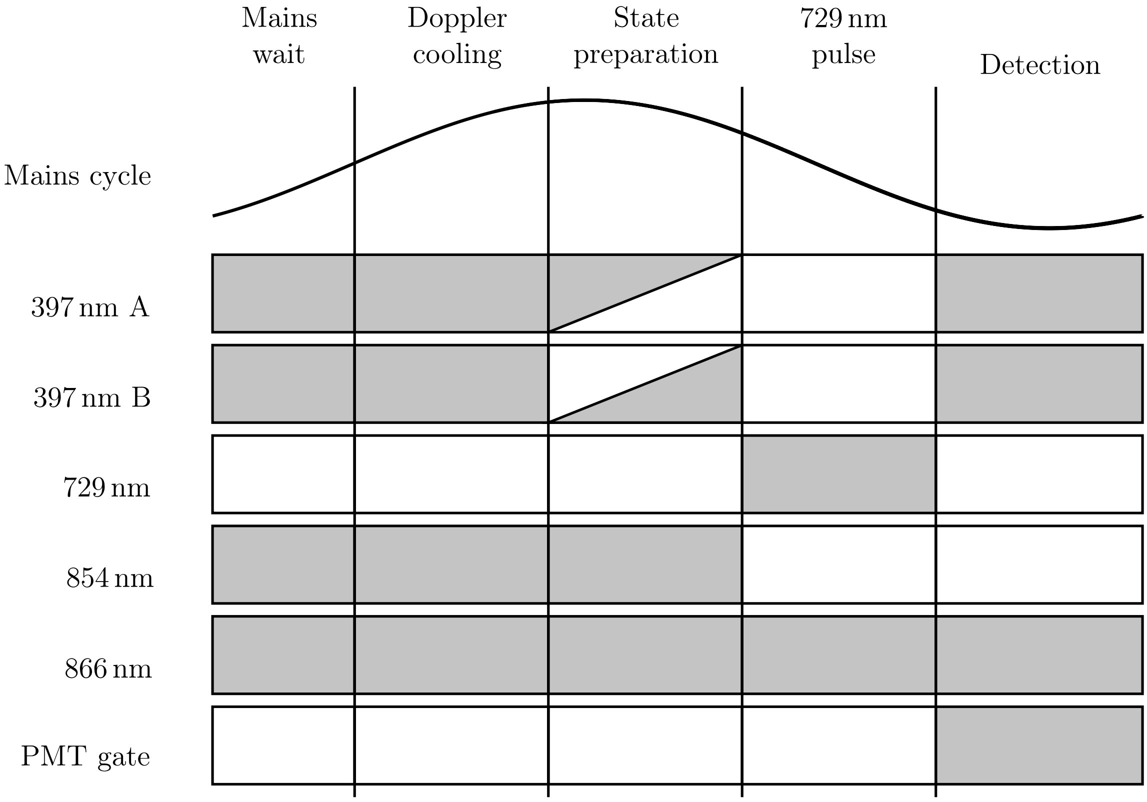

Figure 6.1: Pulse sequence used in spectroscopy of the $S_{1/2} \leftrightarrow D_{5/2}$ transition. State preparation is achieved by optical pumping into one of the magnetic field split ground states. This is achieved by simply turning off one of the Doppler cooling lasers, either 397 nm A or 397 nm B, depending on which magnetic sub-level is required. The boxes are not drawn to scale. See text for details.

6.1.1 Mains triggering

All the electronic equipment in the lab, with the exception of the DC current source and photodiode for locking the narrow linewidth 729 nm laser and the superconducting magnet, are powered from the mains supply. This induces noise on lots of equipment in phase with each other and creates ambient AC magnetic field fluctuations. In order to remove this modulation from our results we phase lock the laser pulse cycle to the mains. First, we step down mains voltage and then compare the signal to ground on a simple voltage comparator. The resulting signal is a square wave which can be used as a digital input to the FPGA. For more details on the mains trigger hardware, see section 4.9.3.

6.1.2 Doppler Cooling

In this section only technical aspects related to Doppler cooling during the spectroscopy experiment will be presented. For more theoretical information see section 3.4.1.

The Doppler cooling part of the pulse sequence ensures that the ion is at the same temperature each time it is interrogated by the 729 nm laser. The broad bandwidth of Doppler cooling ensures that any heating from the environment is quickly removed.

A single ion is robustly confined in our trap with a total depth of roughly 50 eV. This is the maximum energy, summed over all the motional modes, that an ion can have and still remain trapped. However, to increase the orbit of an ion beyond the width of our laser beams (around $100\,\mu$m) only requires roughly 5 meV. Occasionally, there are collisions with background gas molecules (background gas pressure is of the order of 10^{-8} Pa) which imparts this much energy to the ion. When a collision like this takes place, the ion no longer interacts strongly with the laser light. We believe background gas may also sporadically be ionised by the violet Doppler cooling laser beams. The Coulomb interaction with these ions disrupts the experiment. Also rare, but possible, are chemical reactions between hydrogen molecules and the trapped calcium ions [85]. Normally, the ion is returned to the original fluorescence rate in a fraction of a second. However, ions are stable in very large orbits and can potentially take several minutes to return to the centre of the trap.

We count the number of photons received during the Doppler cooling part of the pulse sequence to diagnose any problems with the experiment. If we notice the ion has become dark for a prolonged period, we can pause the experiment and attempt to remedy the situation. However, if the perturbation was too short for us to observe visually, the data is discarded during post processing. The data from a pulse sequence is only included if the number of photons we have detected during the cooling phase is above a set threshold.

6.1.3 State preparation

Optical pumping can be achieved simply by turning off one of the 397 nm Doppler cooling lasers, since the large Zeeman splitting allows the individual transitions to be easily addressed in the frequency domain. In a RF trap, where two transitions are split by less than their natural linewidth, the correct circularly polarised light must be used for state initialisation. This is one advantage of a Penning trap compared to an RF trap; state preparation can be done with potentially higher fidelity.

6.1.4 729 nm pulse

After the Doppler cooling and state preparation parts of the pulse sequence, the ion should have a thermal population distribution. The excitation from the 729 nm laser places the ion in a superposition of the $\mathrm{S}_{1/2}$ and $\mathrm{D}_{5/2}$ levels. To model the resulting excited state population, all vibrational levels must be taken into account, see section 3.2 for more details. The 729 nm laser is narrow enough to resolve vibrational sidebands. However, the remaining observed $\mathrm{S}_{1/2} \leftrightarrow \mathrm{D}_{5/2}$ transition linewidth is dominated by the short term laser linewidth. The laser pulses in the experiment are turned on and off in a top hat fashion. If desired, the laser linewidth can be artificially increased by reducing the laser pulse time.

The 729 nm laser frequency is scanned to build up a spectrum. The laser frequency is varied using a double passed AOM and high resolution signal generator. The 729 nm light to the trap is turned on and off using the same AOM, see figure 4.20 for more details.

6.1.5 State detection

We analyse the photomultiplier counts recorded by the FPGA during the detection phase of the pulse sequence to determine the internal state of the ion. The fluorescence from the whole spectrum is collated and the data are plotted as a histogram with respect to the number of photons detected. An example of the data we collect is shown in figure 6.2: it clearly has a bimodal structure. When the ion is shelved in the $\mathrm{D}_{5/2}$ state only a few photons are counted in the detection period, corresponding to the lower peak. The lower peak has a non-zero mean value because both scattered light from the laser beams and thermionic emission from the PMT photocathode are also counted. The higher peak, when more photons are counted, relates to the superposition of the two atomic energy levels collapsing to the $\mathrm{S}_{1/2}$ state after interacting with the Doppler cooling lasers.

By setting a threshold between these two distributions, the internal state of the ion can be determined with high probability. A complication arises with calcium ions in a Penning trap, due to quantum J-state mixing, see section 4.1.1 for more details. If initially during the detection period we observe fluorescence, on average after 54 ms (if the transition is saturated), in our magnetic field, the ion will shelve in the $\mathrm{D}_{5/2}$ state. This is similar to any random decay process, with an exponential dependence on time. Hence, the highest decay rate occurs when we initially turn on the detection lasers. If the shelving event happens before the control system has counted enough photons to recognise that the ion was initially bright, we record a false shelving event. In effect, this reduces the fidelity of state detection.

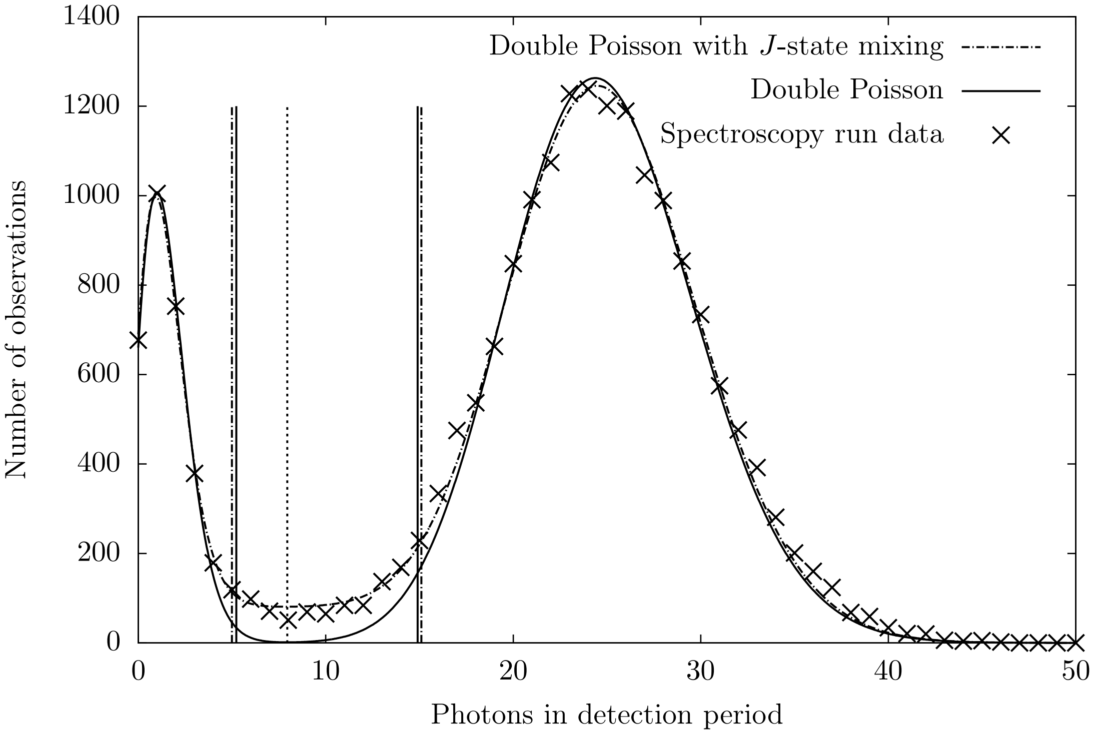

Figure 6.2: Histogram of photon counts in a 5 ms detection period. The number of photons counted in a particular bin are quantised and shown by ×. The functions that are fit to this data assume a double Poissonian distribution with and without a plateau between the two peaks to simulate quantum J-state mixing. The vertical dotted line is set at the minimum of the double Poisson fit. The solid and dashed-dot vertical lines are at 3 standard deviations from the mean of the lower peak and 2 standard deviations from the mean of the higher peak for the different fit models. The mean values for the lower and upper peaks are approximately 1.5 and 25 respectively for a detection time of 5 ms. See text for details.

Figure 6.2 shows a histogram of the data collected during one particular spectroscopy run. In the absence of quantum J-state mixing the data should follow a double Poisson distribution of the form

$$\frac{AB^k e^{-B}}{k!} + \frac{CD^k e^{-D}}{k!}, \tag{6.1}$$

where A and C are the amplitudes and B and D are the mean values for the lower and upper peaks respectively. In the double Poisson fit on figure 6.2, these distributions are clearly separated. When this is the case then a threshold placed where the vertical dotted line is located would work well to discriminate between fluorescing and non-fluorescing events. However, the data does not follow this fit in the region between the two peaks. If we assume that the quantum J-state mixing decay period is at least 5–10 times longer than the detection period, we can approximate the exponential decay with a straight line. In this regime, the photon count histogram should include an approximately flat distribution of events between the mean values B & D. To take account of this effect, the data was fitted to the equation

$$\frac{AB^k e^{-B}}{k!} + \frac{CD^k e^{-D}}{k!} + \frac{E}{2}\left[\operatorname{erf}\left(\frac{k-B}{\sqrt{2B}}\right) - \operatorname{erf}\left(\frac{k-D}{\sqrt{2D}}\right)\right], \tag{6.2}$$

where E is the amplitude of the plateau between the two peaks. This fit follows the data more closely closer over the entire range of the histogram. An error function is used because it has the same shape as is required here and not for any fundamental reason.

In order to remove some of the quantum J-state mixing events from mistakenly being counted as shelving events, the threshold is set as close to B as possible. On figure 6.2 the two vertical lines, relating to the two different fit models (equations 6.1 & 6.2), close to the lower peak are set at 3 standard deviations above B. At this point, a large fraction of the false shelving events are removed while still counting the majority of real shelving events.

We also count the number of photons received in the cooling period before the 729 nm pulse. A second threshold is set to make sure that the ion is cold and localised, e.g. has not just collided with a background gas molecule. This threshold is set at two standard deviations below D.

The two models have very different behaviour in the region between the two peaks. However, they have very similar mean values B and D. Hence, the difference between the thresholds shown by the solid and dashed-dot lines in figure 6.2 is often inconsequential.

There are several more sophisticated techniques to determine the difference between an ion that is fluorescing, shelved or undergoes quantum J-state mixing during detection. One method studied in detail in reference [86], named maximum likelihood detection, which may increase the fidelity of this readout stage, and would be required at higher magnetic fields where quantum J-state mixing will have a larger affect. Alternatively, the average number of photons scattered during the detection process could be increased before shelving to the $\mathrm{D}_{5/2}$ state by selectively repumping the magnetic field split $\mathrm{D}_{5/2,-3/2\ldots 3/2}$ levels. However, this limits the transitions which can be stimulated during the 729 nm pulse to $\mathrm{S}_{1/2,1/2} \leftrightarrow \mathrm{D}_{5/2,5/2}$ and $\mathrm{S}_{1/2,-1/2} \leftrightarrow \mathrm{D}_{5/2,-5/2}$. The emission patterns of these transitions show that it would no longer be possible to stimulate axial motional sidebands with these particular $|\Delta m_j| = 2$ transitions when confined by our current optical access. In the end, there is only so much information that can be extracted from so few photons. To increase the detection fidelity further the only option would be to increase the light gathering efficiency. This is difficult with most Penning traps due to limited optical access. For example in our set up, the fluorescence must be channelled along a 14.2 ± 0.5 mm gap, between the vacuum chamber and magnet bore, for a minimum of 30 cm before it can be imaged. Perhaps, progress could be made by using a trap where transparent electrodes coated with indium-tin-oxide are also shaped as light collecting optics [87]. This would be particularly applicable to a Penning trap where only static fields are required. Alternatively, the collection efficiency could be increased by forgoing bulk optics altogether and using just optical fibres close to the ions [88].

6.2 Magnetic field components of the 729 nm transition

The large magnetic field used for confinement splits the $\mathrm{S}_{1/2} \leftrightarrow \mathrm{D}_{5/2}$ transitions by many gigahertz. To stimulate these different transitions, the laser must be unlocked from the cavity and its wavelength altered.

The $\Delta m_j = 0$ transitions cannot be stimulated because they require light incident at approximately 45° to the magnetic field, where we have no optical access. The $|\Delta m_j| = 1$ transitions can be stimulated with different strengths both parallel and perpendicular to the magnetic field and $|\Delta m_j| = 2$ transitions can only be stimulated perpendicular to the magnetic field. See section 3.1.2 for details.

In a 1.85 T magnetic field the separation of the transitions is far greater than the tuning range of our AOM. In order to lock the 729 nm laser for use with a given transition we first have to find the atomic resonance, this is done by manually varying the laser frequency while still using the pulse sequence outlined in section 6.1. Next we attempt to identify a TEM mode of the ULE cavity which has a similar frequency. The laser is locked to this mode and AOM frequency is set compensate for any discrepancy between the cavity and atomic resonances.

To tune between the atomic transitions once the different frequencies are known the laser is first unlocked from the cavity and the the ECDL piezo is altered to the correct wavelength according to the wavemeter. The wavemeter can drift by a maximum of a few hundred megahertz but is always accurate enough to determine to which free spectral range of the cavity the laser needs to be locked. The laser is then locked to the cavity mode previously recorded. Note that the linewidth of the cavity is narrow enough to resolve the difference between perpendicular modes which are split by roughly 100 kHz. Finally the AOM frequency is set. The first positive diffracted order from the modulator is used, increasing the frequency of the light by twice the input RF frequency in our double pass setup.

Table 6.1 lists all the transitions that we have observed and the AOM offset frequency relative to the cavity mode. There is no absolute frequency measurement because we did not have access to a narrow linewidth absolute frequency reference.

Transition $S_{1/2} \leftrightarrow D_{5/2}$	Wavemeter reading /THz	Transverse Cavity Mode	AOM frequency shift /MHz
$-1/2 \leftrightarrow -5/2$	410.9892	0, 2	430
$-1/2 \leftrightarrow -5/2$	410.9892	0, 11	550
$-1/2 \leftrightarrow -5/2$	410.9892	0, 21	520
$-1/2 \leftrightarrow -3/2$	411.0205	0, 18	532
$-1/2 \leftrightarrow 1/2$	411.0829	0, 4	510
$1/2 \leftrightarrow -3/2$	410.9685	0, 6	520
$1/2 \leftrightarrow -1/2$	410.9995	0, 2	510
$1/2 \leftrightarrow 3/2$	411.0619	0, 13	510

Table 6.1: Table showing which $S_{1/2} \leftrightarrow D_{5/2}$ transitions have been stimulated in our Penning trap. The AOM frequency shift column is twice the frequency applied to the AOM from the signal generator.

	Magnetic field dependence GHz T^{-1}	
Transition	Minimum	Maximum
π	5.595	5.595
σ	11.205	22.395
δ	28.005	39.195

Table 6.2: Magnetic field dependence of the different 729 nm transitions. Pi transitions are the least sensitive to magnetic field fluctuations.

Stimulating π transitions would minimise sensitivity to magnetic field fluctuations. That would require light incident at 45° relative to the quantisation axis (see figure 3.2(c)). Unfortunately, the current setup does not have optical access from this direction. Table ?? lists the magnetic field dependence of the different 729 nm transitions.

6.3 Cavity Drift

Cavity drift limits the accuracy of the spectra presented in this chapter to tens of kHz over an hour or so. Ultra-low-expansion glass has a very small thermal expansion coefficient over a wide range of temperatures but can be minimised at only one specific temperature. We can calculate the fractional change in length of the cavity that would correspond to a 1 kHz shift in laser frequency,

$$\frac{\Delta L}{L} = \frac{10^3 \times \lambda}{c} \cong 2.4 \times 10^{-12}, \tag{6.3}$$

which is equivalent to 2.4×10^{-13} m for our 10 cm long cavity or approximately $1/200^{\text{th}}$ of a Bohr radius!

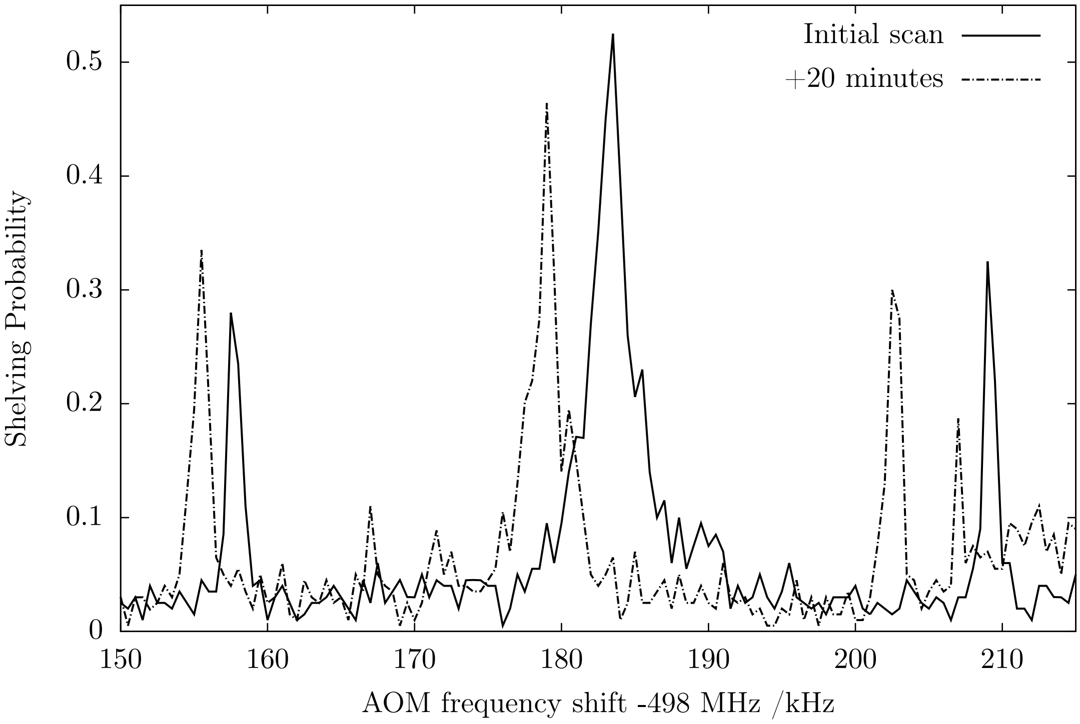

Figure 6.3: Two scans over an axial sideband with a magnetron sideband either side taken twenty minutes after each other. Data recorded by Joe Goodwin.

The effect of the temperature drift was empirically measured by repeatedly scanning over a single axial sideband with sub-sidebands at the magnetron frequency. The laser frequency was incremented in 500 Hz steps and the 729 nm pulse length was set to 6 ms. The data in figure 6.3 was taken when the temperature of the ULE cavity high-finesse cavity used to stabilise the 729 nm spectroscopy laser was set to around 26°C. See section 6.4 for more detail on how spectra of the axial motion were obtained. Figure 6.3 shows that twenty minutes after the initial scan, the central peak had drifted 4.2 ± 0.5 kHz. We can see that the cavity is drifting at different rates in the two scans because the magnetron sidebands are separated by different amounts even though the trap bias was held constant. Cavity drift can be significant even during a single experimental sequence; each scan in figure 6.3 would take around 12 minutes to complete.

To determine the temperature dependence of the cavity length we stimulated the $S_{1/2,1/2} \leftrightarrow D_{5/2,-1/2}$ transition from the axial direction with the reference cavity locked to several different temperatures. Figure 6.4 shows that the centre frequency of the transition shifts $0.43\,\mathrm{MHz\,K^{-2}}$ relative to the turning point predicted by the data at 21.1 °C. If further measurements continue to follow this trend the AOM frequency shift required will be 488 ± 0.5 MHz. The in loop measurement of the cavity temperature suggested a maximum

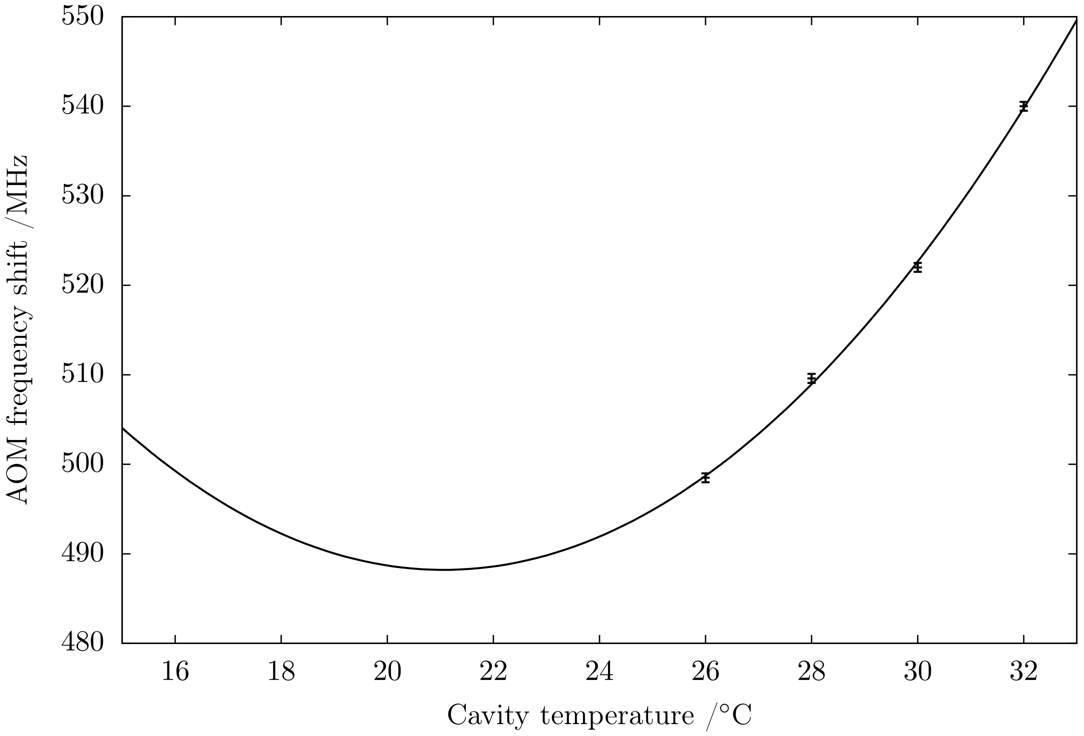

Figure 6.4: The $S_{1/2,1/2} \leftrightarrow D_{5/2,-1/2}$ transition frequency relative to the 0,2 transverse cavity mode as the temperature is changed in 2 °C steps from 26.0°C to 32.0 °C. The data is fit to a quadratic curve.

variation of approximately 0.5 mK. We can put a measured value on the cavity temperature variation. If the cavity resonance was to drift a maximum of 10 kHz at 26°C, we find the temperature variation of $10/(430 \times 5) = 5\,\mathrm{mK}$.

Unfortunately we could not the lock the reference cavity to a temperature lower than 26 °C because only a heater was used for the feedback mechanism. Work is currently under way to lock the cavity temperature using a continuously cooled thermo-electric peltier element which should allow a spectrum to be recorded with significantly less drift.

6.4 Axial Spectrum

The spectroscopy and repumping laser beams are overlapped on the optical table. These beams are then coupled into a polarisation-maintaining fibre and sent to the experiment breadboard. The light propagates through the trap approximately parallel to the trap axis. In this configuration, only σ transitions can be stimulated. The laser was tuned close to the $S_{1/2,1/2} \leftrightarrow D_{5/2,-1/2}$ transition and scanned in steps of 5 kHz. The laser pulse sequence was repeated 200 times at each frequency. The shelving probability was calculated from the fraction of these interrogations where the number of photons that were recorded was less than a set threshold. The pulse sequence used to obtain the spectrum in figure 6.5 is shown in table 6.3. The spectrum obtained in figure 6.5 took around 3 hours to complete.

Laser state	Pulse time /ms
Mains phase wait	N/A
Doppler cooling	5
State preparation σ^- - off, σ^+ - on	0.4
729 nm pulse	9
Detection	5

Table 6.3: Pulse sequence used to produce sideband spectrum in figure 6.5. The total pulse time is less than the mains cycle so that sequence is repeated at 50 Hz.

The spectrum in figure 6.5 shows sidebands around the carrier. Many sidebands are present making it difficult to identify one in particular as the carrier. The sidebands are separated by the axial trap frequency. Some of the central peaks are surrounded by sub-sidebands separated by the magnetron frequency. The transition is clearly saturated because there are many sidebands which reach around 0.5 shelving probability. This is the shelving probability we expect for an ion in thermal distribution which is well saturated, see section 3.2 for more details. However, the sidebands in the saturated region of the spectrum do not show equal shelving probabilities. There are several possible explanations for this:

1. **Shot noise:** After the 729 nm laser pulse, the internal state of the ion is a coherent superposition of both $\mathrm{S}_{1/2,1/2}$ and $\mathrm{D}_{5/2,-1/2}$ levels. When the transition is saturated we can assume that the amplitudes of these two states are roughly equal. We detect the state of the ion with Doppler cooling light, producing a digital signal subject to Poisson statistics. Hence, we would expect a standard deviation of 0.05 in the shelving probability for 100 repetitions.

2. **Quantum *J*-state mixing:** During the state detection period, quantum J-state mixing leads to the ion shelving in the $\mathrm{D}_{5/2}$ state. Occasionally this appears as an additional shelving event increasing the shelving probability. This effect should also be present if the 729 nm laser is blocked. We found that this added an additional 0.01–0.05 to the shelving probability. This is equivalent to a DC offset on the data and is independent of the 729 nm laser frequency.

3. **Under-sampling:** The sideband linewidth is dominated by the laser linewidth. If the short term laser linewidth is less than the frequency step, the sidebands would not be sampled accurately. This is clearly true because usually there are only 2 or 3 frequency steps in resonance with any particular sideband.

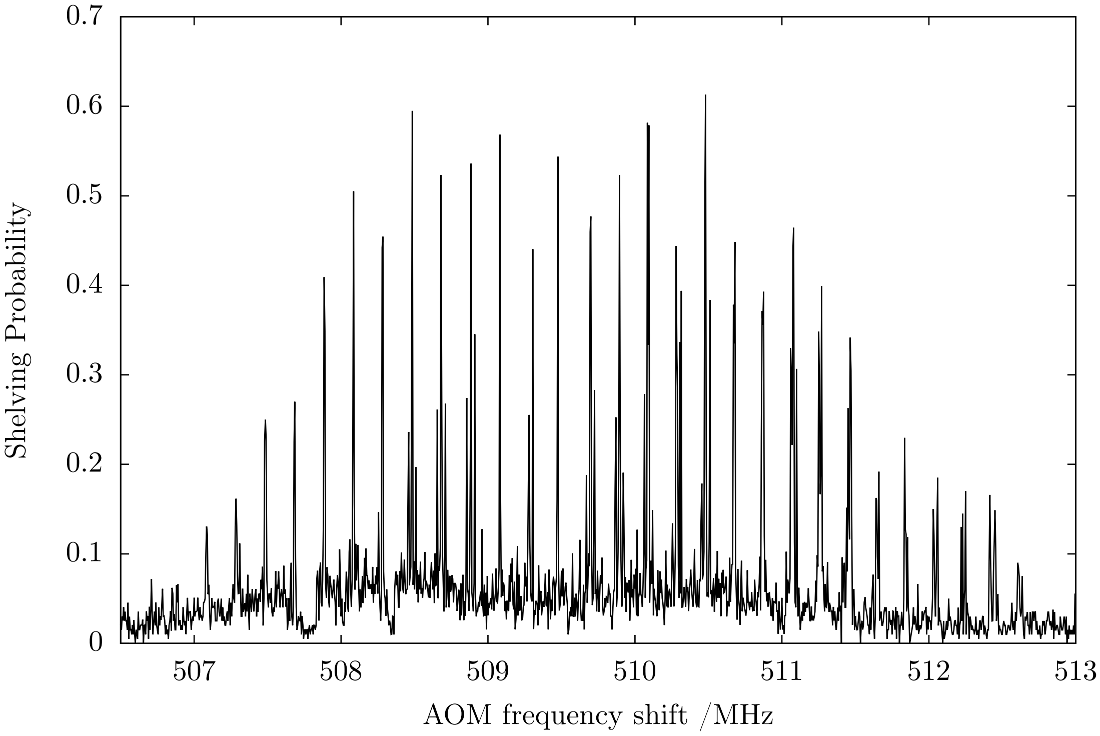

Figure 6.5: Axial spectrum of the $S_{1/2,1/2} \leftrightarrow D_{5/2,-1/2}$ transition. The peaks are separated by the axial trap frequency; some central sidebands are flanked by peaks separated by the magnetron frequency. See text for details.

4. **Cavity Drift:** During the time required to complete the pulse sequences for a particular point on the spectrum, the length of the reference cavity can drift. This shifts the laser frequency, altering the shelving probability even though the frequency of the sine wave sent to the AOM has not been changed. If the cavity drifts at a similar rate to the frequency scan in the experiment, the sidebands are broadened. The double peaked features towards the higher frequency end of the spectrum are attributed to this affect.

Combining these effects, the shelving probability could reach approximately 0.6 but no higher which is in good agreement with the observed spectrum.

After Doppler cooling, the ion should be in a thermal state with occupation probability $P(n) = \bar{n}^n/(1+\bar{n})^{n+1}$. The Doppler cooling limit for the axial motion in our trap is $\bar{n} = 26$, at optimised laser frequencies and intensities, assuming that $\gamma/2\pi = 21\,\text{MHz}$ and $\omega_z/2\pi = 200\,\text{kHz}$. In this case, and at higher temperatures, the sideband peaks should follow a Gaussian profile due to Doppler broadening. However, in figure 6.5 the 729 nm laser pulse saturates the transition and now there are at least two free parameters that need to be fit to the spectrum: the temperature of the ion and the degree of saturation.

This assumes that the ion temperature in each of the interrogations was similar. Drift in the Doppler cooling laser frequencies while the 729 nm laser was scanned across the range of the spectrum means that this is almost certainly not true.

The error on the height of the peaks in figure 6.5 could easily be 0.05 for the reasons outlined above. So instead of trying to fit the data to what we should expect theoretically, figure 6.6 shows three cases with different ion temperatures and saturation parameters. From figure 6.6 the best estimate that can be drawn from the data for the occupation number is $\bar{n} = 100^{+100}_{-50}$. The predicted spectra shown in figure 6.6 shows that for $50 < \bar{n} < 200$ the data and the simulations agree moderately well. However, when the mean occupation number of the ion in the simulation is increased to $\bar{n} = 500$, there is significant deviation from the observed data. In order to keep the predicted spectrum with $\bar{n} = 500$ roughly as narrow as the data, the interaction time must be reduced and the shelving probability does not agree with the data.

The spectrum in figure 6.5 is clearly not symmetric, and does not follow the overall shape of the predicted sidebands in figure 6.6, especially in the AOM frequency shift range from 511.5 MHz to 512.5 MHz. This could correspond to a change in the Doppler cooling temperature over the time that the spectrum took to measure (approximately 3 hrs). The temperature of the ion before the 729 nm pulse is only set by the Doppler cooling laser intensities and detunings. The transfer cavity lock described in section 4.3.4 keeps the two Doppler cooling lasers locked to 5–10 MHz. However, drift of this magnitude is large enough to affect the laser detuning from the atomic transition and varies ion temperature.

There are 24 sidebands in figure 6.5 between the peaks at 507.085 MHz and 511.835 MHz. By calculating the average spacing between these peaks we measure an axial frequency of $\omega_z/2\pi = 198 \pm 10\,\mathrm{kHz}$. The spectrum was recorded at a trap bias of 52.2 V. Section 2.1.1 shows that $\omega_z/2\pi = \kappa\sqrt{V}$, where κ is a constant of proportionality and V is the trap bias. This data implies $\kappa = 27.4 \pm 1.5\,\mathrm{kHz\,V^{-1/2}}$. This value agrees with the results in section 5.1, where it was measured that $\kappa = 26.36 \pm 0.03\,\mathrm{kHz\,V^{-1/2}}$, within the range of the error bars. The sideband spectrum in figure 6.5 also shows that the laser beam is aligned along a direction with components of both the axial and magnetron motions. We can see this clearly in figure 6.7 where sub-sidebands which are separated from the main peaks by the magnetron frequency are shown. Using equation 2.8, and assuming a 1.85 T magnetic field, we expect that the magnetron frequency will be 26.3 kHz. Measuring the frequency difference between the sub-sidebands on 5 of the clearest peaks gives a splitting of $26.5 \pm 2.0\,\mathrm{kHz}$ which shows good agreement with the calculation.

Since the magnetron motion is in the radial plane, it is not immediately obvious that magnetron sidebands should be seen in the axial spectrum. There are at least two reasons why magnetron sidebands are visible in the axial spectrum in figure 6.5:

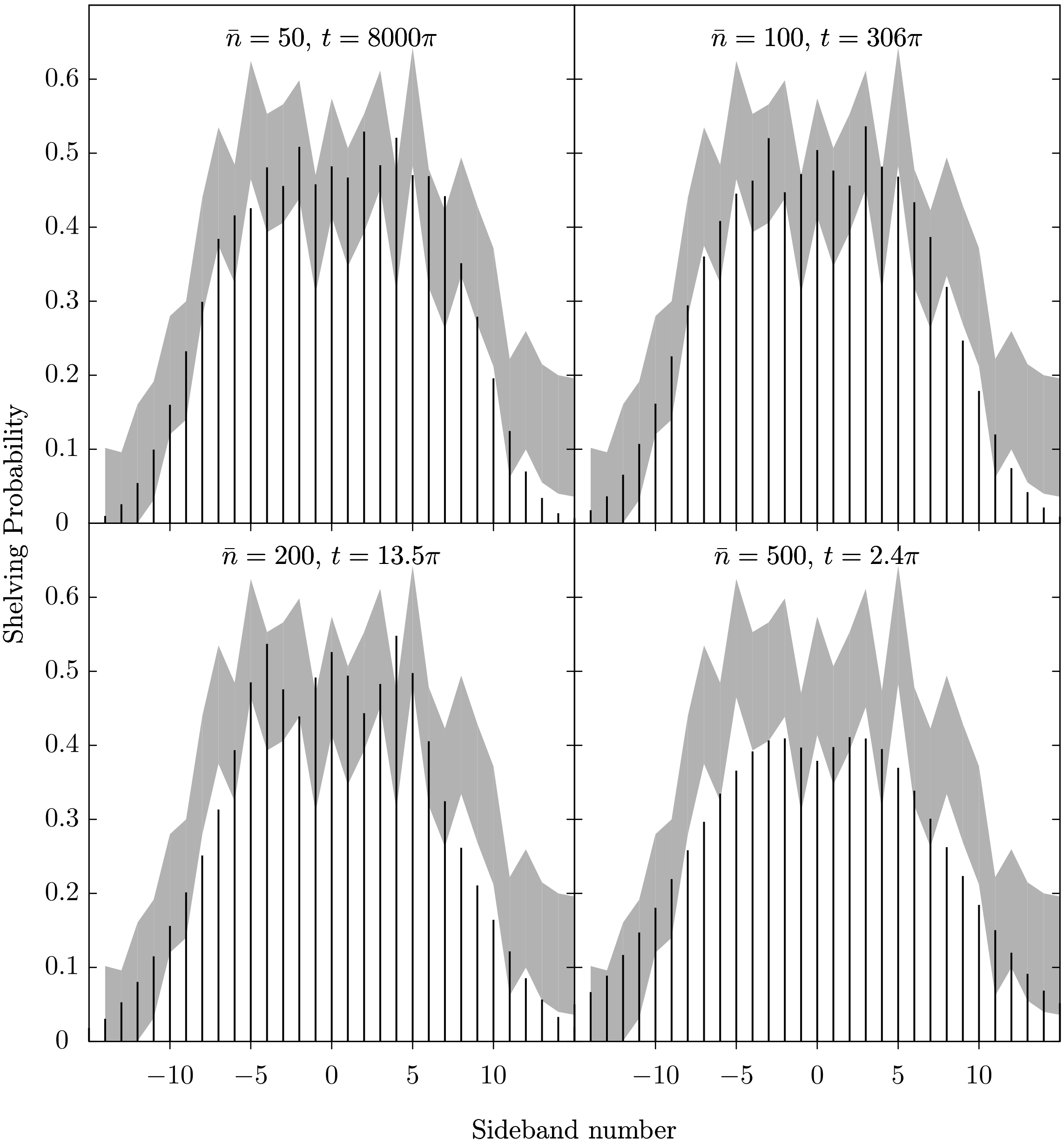

Figure 6.6: The Axial spectrum is fitted to different ion temperatures and saturation parameters given in the title of each plot. The solid lines are predicted shelving probabilities from equation 3.55. The filled curves are the data from peaks in figure 6.5 with the points simply joined and a ±0.05 error margin. A 0.05 offset is also subtracted from the data to take into account the additional shelving due to quantum J-state mixing.

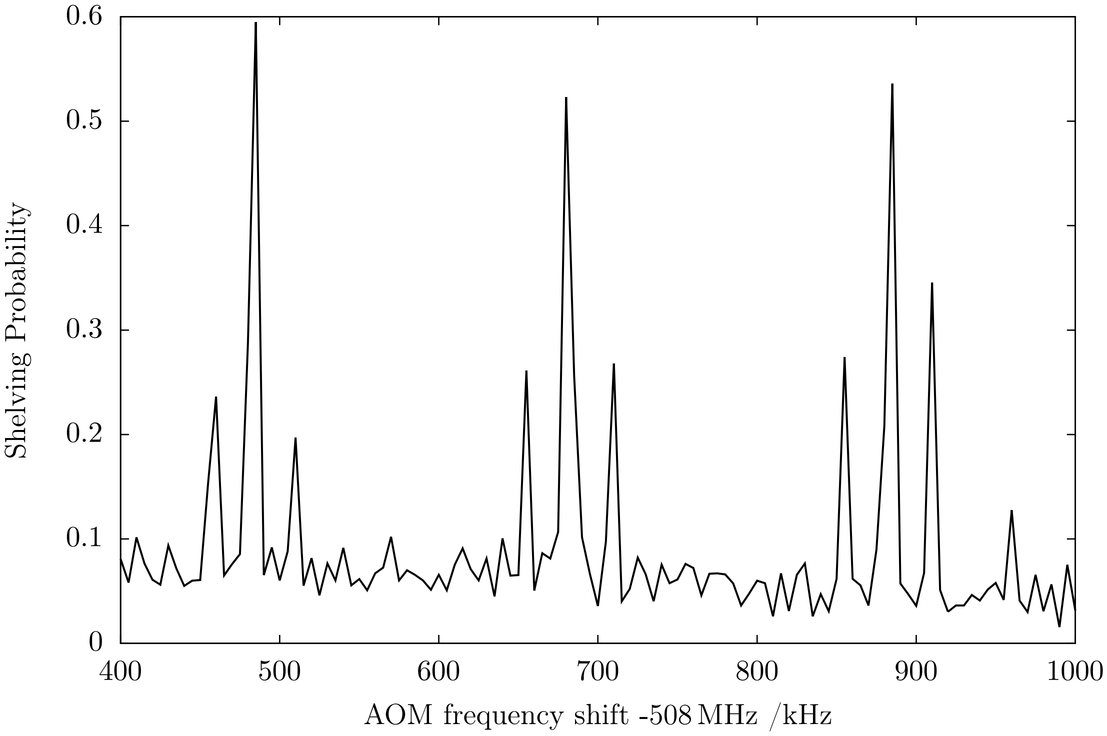

Figure 6.7: Section of the axial spectrum showing magnetron sidebands around axial sidebands.

- The magnetic field and trap axis are not aligned properly. Now the $\mathbf{E} \times \mathbf{B}$ force, which manifests as the magnetron motion, is no longer solely in the radial plane. This modifies the magnetron frequency from the simple derivation in chapter 2.
- The laser is not aligned along the trap axis. This is certainly true. There is a blemish at the centre of the exit viewport above the trap which requires the laser beams to be skewed relative to the trap axis to avoid excessive background laser scatter.

Most likely, both of these effects contribute to the results.

The magnetron sidebands appear in the spectrum with a shelving probability of up to 0.35. This is artificially higher than would be expected naively, due to saturation effects.

We can perform several diagnostics on the experimental setup using the ion as a probe. The laser was scanned over a frequency range known to contain a sideband both with and without locking to the mains. We assume that when we are not locked to the mains cycle, there are many unresolved 50 Hz sidebands present. The spectroscopy laser was scanned across a single sideband in 1 kHz steps. The 729 nm laser pulse length was 0.5 ms. Figure 6.8 shows a sideband as a single peak when the pulse sequence is locked to the mains cycle and a double peak when free running. It is clear from figure 6.8 that the probability for shelving the ion is both broadened over a larger frequency range, and reduced in amplitude, when the mains wait is not included in the pulse sequence. If we assume that the modulation in figure 6.8 is due to ambient magnetic field in the laboratory, it is possible to calculate the magnitude of the fluctuations. The Zeeman splitting for the $S_{1/2} \leftrightarrow D_{-1/2}$ transition is $22\,\mathrm{GHz\,T^{-1}}$. Hence, a 5 kHz modulation suggests magnetic field fluctuations on the order of $2 \times 10^{-7}\,\mathrm{T}$.

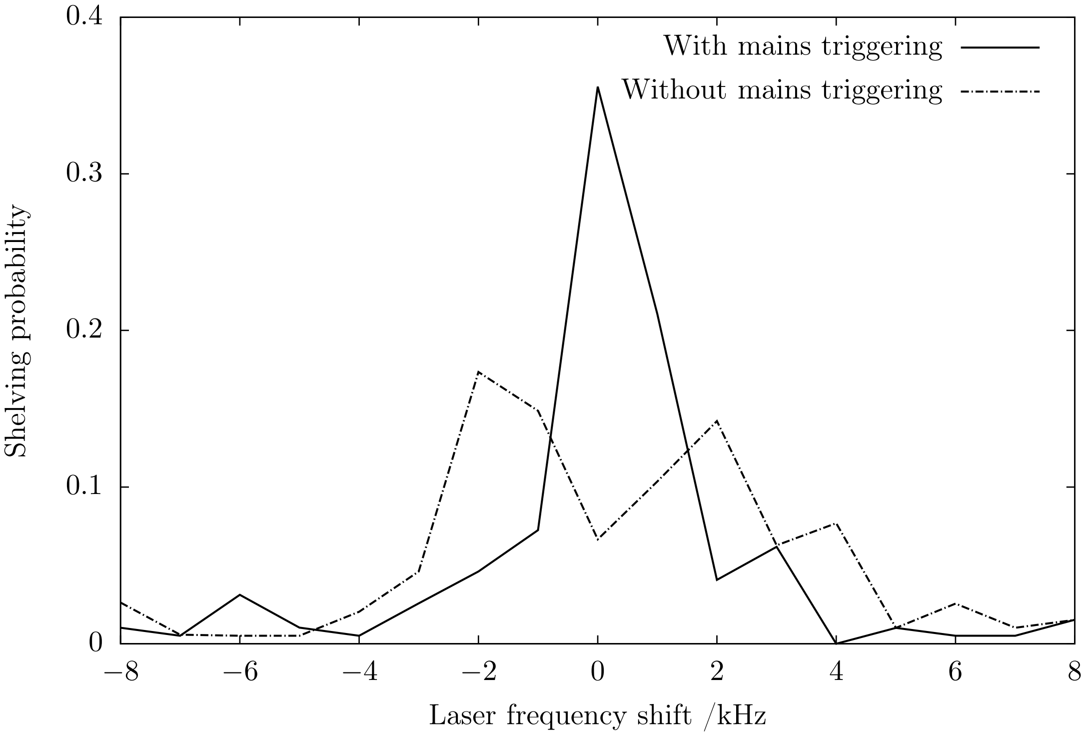

Figure 6.8: A scan over a single sideband with and without synchronising to the mains. The sidebands have been centred on top of each other to give a clear view of the difference. An offset due to the reference cavity drift has been removed in post-processing.

State preparation in our set-up is very fast. Due to the Clebsch-Gordon coefficients, decay preferentially occurs from the $P_{1/2}$ level via σ polarised light, see appendix A. Therefore, on average, between only 1 and 2 spontaneous decay events are required to optically pump to the correct state for the start of the experiment. To test the length of time this takes, we stimulated the quadrupole transition with and without the state preparation stage. In the case where there is no state preparation the shelving probability should be halved. The results in table 6.4 show that an optical pumping pulse of only 500 ns is long enough to prepare the correct state.

State preparation time /μs	Shelving probability
0	0.14 ± 0.02
0.5	0.21 ± 0.02
200	0.23 ± 0.02

Table 6.4: Shelving probability to the $D_{1/2}$ level as a function of state preparation time.

6.5 Radial spectrum

Thus far the quadrupole transition spectra presented have been obtained by excitation using a 729 nm laser beam aligned so that predominantly the axial sidebands are detected. In order to observe modified cyclotron and strong magnetron sidebands excitation along the radial plane is required. Switching between the two is very simple. The 729 nm laser light is now combined with radial repumper beam on the optical table and coupled into the same polarisation maintaining optical fibre. This beam is then overlapped with the radial cooling beam on the experimental breadboard.

It is clear from chapter 2.1 that motion in the radial plane in a Penning trap is more complicated than that in the axial direction. In the lab frame the magnetron and modified cyclotron motions are superimposed upon each other. However, they can still be thought of as two harmonic oscillators and we can still write them in the standard quantum mechanical form as shown in equation 2.24.

The modified cyclotron motion behaves in a similar way to axial motion where stimulating a sideband with lower energy than the carrier transition leads to a reduction in the magnitude of the orbit. This sideband disappears in the limiting case, $\bar{n} = 0$. For the magnetron motion, the opposite is true. Stimulating a motional sideband of the magnetron mode with higher energy than the carrier corresponds to a reduction in the magnitude of the orbit.

During the experiment to measure a radial spectrum, the trap bias was set to 30.00 ± 0.02 V. For a magnetic field of 1.85 T the oscillation frequencies for a $^{40}\mathrm{Ca}^+$ ion should be, $\omega_z/2\pi =$ 144.4 kHz, $\omega_+/2\pi = 690.0$ kHz & $\omega_-/2\pi = 15.1$ kHz. The relationship between the axial motional frequency and the trap bias measured in section 5.1 is used to calculate these values. To record the spectrum we stimulated the $S_{1/2,1/2} \leftrightarrow D_{5/2,-1/2}$ transition, the same as in figure 6.5. However, the cavity temperature was lower to reduce the cavity drift. This is the reason why there is an absolute frequency difference of approximately 8 MHz between the axial and radial spectra.

The pulse sequence in table 6.5 was repeated 100 times at each frequency to record the results shown in figure 6.9. The laser frequency was incremented in 400 Hz steps to make

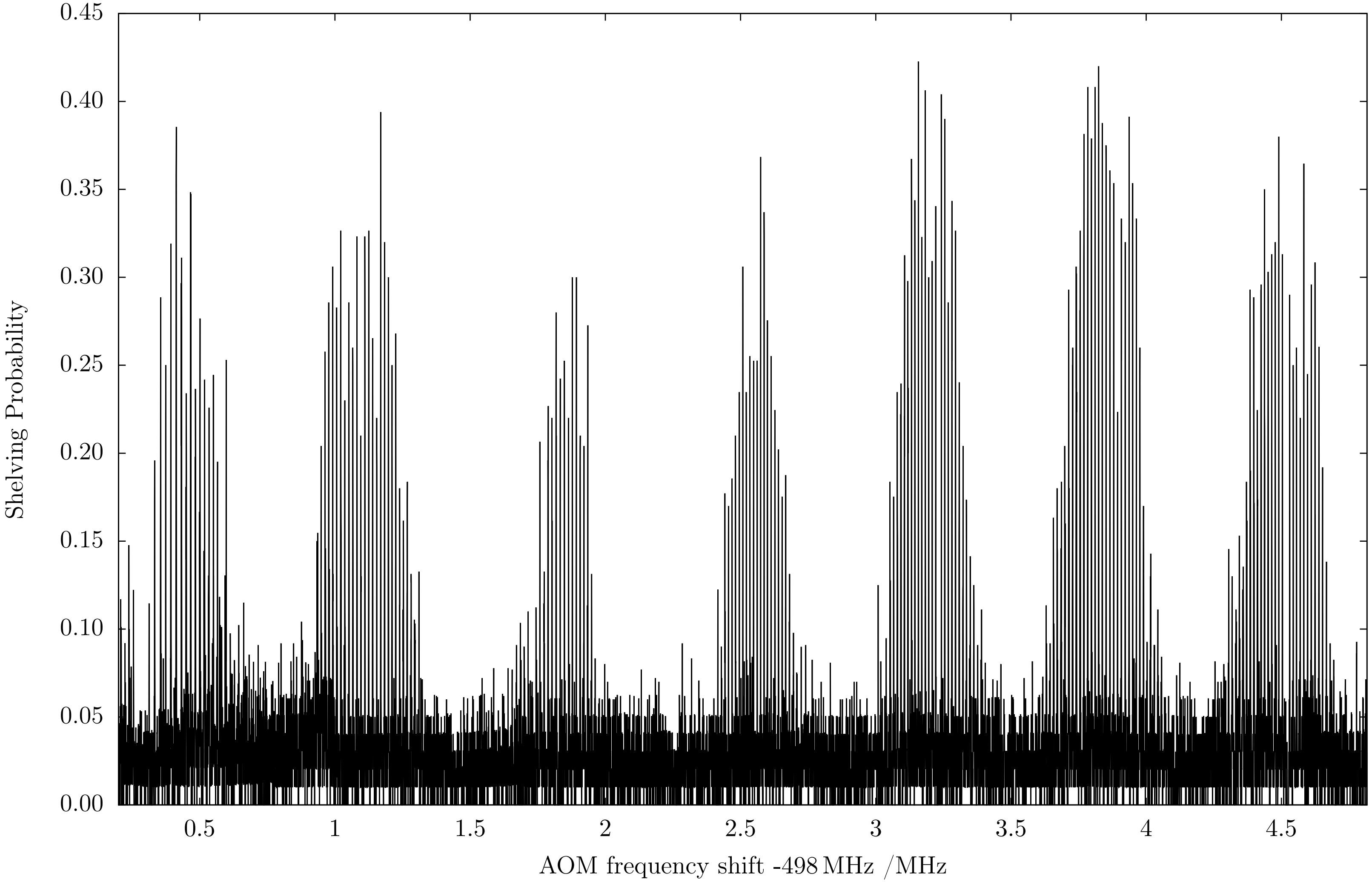

Figure 6.9: Vibrational spectrum of the radial modes using the $S_{1/2,1/2} \leftrightarrow D_{5/2,-1/2}$ electric quadrupole transition. Each cluster of closely spaced lines (magnetron sidebands) belong to a single modified cyclotron sideband. Due to time constraints only a portion of the entire spectrum was recorded showing 7 modified cyclotron sidebands. See text and table 6.5 for details.

Laser state	Pulse time /ms
Mains phase wait	N/A
Doppler cooling	7
State preparation σ^- - off, σ^+ - on	0.4
729 nm pulse	5
Detection	7

Table 6.5: Pulse sequence in this table was repeated 100 times at each frequency step to produce radial sideband spectrum in figure 6.9.

sure that sidebands usually consisted of more than a single point in the spectrum. The 729 nm laser pulse length was 5 ms, which is equivalent to a 400 Hz time-bandwidth limited laser linewidth. For a better measurement of the shelving probability, there should be at least 3 or 4 frequency steps over this range. However, the laser linewidth is much less than the modified cyclotron frequency so it was necessary to tune the AOM to many different frequencies to resolve the entire spectrum displayed in figure 6.9.

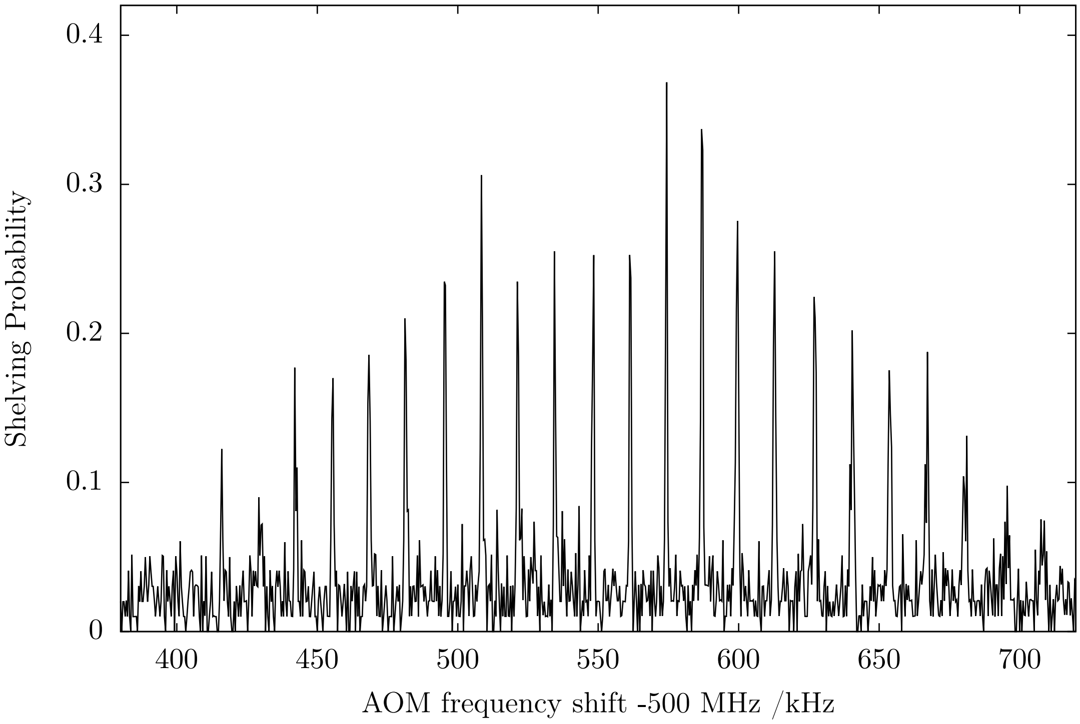

Figure 6.10: Magnetron sidebands around a single modified cyclotron sideband.

The spectrum in figure 6.9 took approximately 9 hours, between 9 pm and 6 am, to complete. This led to drift in several parameters. Most important to cooling the radial motion in a Penning trap are the Doppler cooling laser frequencies and beam positions [15, 89]. Ideally these parameters would remain fixed so that the 729 nm laser could interrogate an ion with the same temperature each time the pulse sequence is repeated. However, this was not the case and it was clear during the experiment that the running average fluorescence rate varied by around one third. Some possible explanations for this drift include:

- Temperature change in the lab and thermal drift on the optical mounts for the laser beams going into the trap.
- Laser frequency drift on the Doppler cooling lasers of 5–10 MHz as mentioned for the axial spectrum.
- Other factors such as a change in the amplitude of mains voltage as the load in the physics department at Imperial College changed throughout the day.

Figure 6.9 shows 7 modified cyclotron sidebands each with up to 30 magnetron sidebands around them. Figure 6.10 shows a zoomed in version of one of the modified cyclotron sidebands. Here, even by eye, it is clear that magnetron sidebands are very close to equally spaced. The magnetron frequency of $\omega_-/2\pi = 14.2 \pm 1.0\,\text{kHz}$ is measured from the average sideband spacing in figure 6.9. This value is in good agreement with the predicted frequency, 15.1 kHz. Magnetron sidebands may appear to have different frequency splitting at different points in the spectrum due to cavity drift, hence why there is a relatively large error associated with this measurement. Many more motional sidebands are present in figure 6.9 than in figure 6.5. In the ions frame of reference the laser is modulated far more and therefore has a lower spectral purity. Hence, we now record an unsaturated spectrum where none of the sidebands observed have an excitation probability greater than one half.

It is interesting to note that the cluster of magnetron sidebands around each modified cyclotron sideband are well separated. This also shows that the energy spread of the magnetron mode is small compared to the axial and modified cyclotron modes. From first inspection, the magnetron mode appears to have an equivalent temperature in the tens to hundreds of micro-Kelvin range. It must be noted that this is only a probe of the kinetic energy of the system. Further analysis similar to that in section 3.2 is required to explain this behaviour; with the caveat that now two motional modes need to be considered simultaneously.

By measuring the spacing between modified cyclotron sidebands and adding this to the magnetron frequency, the true cyclotron frequency can be measured. The magnetic field can then be calculated directly from equation 2.9. The measured frequency difference between the first and sixth modified cyclotron sideband is $3.39 \pm 0.05\,\text{MHz}$, which implies $\omega_+/2\pi = 679 \pm 25\,\text{kHz}$. Using these data, and the measured magnetron frequency, we can calculate the magnetic field in the trap. The motional frequencies suggest $\mathbf{B} = 1.82 \pm 0.03\,\mathrm{T}$, this is in good agreement with the Doppler cooling laser frequencies and the magnetic field components of the $\mathrm{S}_{1/2} \leftrightarrow \mathrm{D}_{5/2}$ transitions, which both suggest a magnetic field of $1.84 \pm 0.01\,\mathrm{T}$. The majority of the error comes from poor sampling of sidebands and cavity drift over the spectrum time period.

Chapter 7

Discussion

In this thesis I have shown that, in principle, many of the experiments performed in RF traps can also be done in a Penning trap. Vibrational sidebands of all the motional modes can be clearly resolved via spectroscopy of a narrow linewidth electric quadrupole transition. This is despite the large ratio between the magnetron and modified cyclotron frequencies.

We can resolve motional sidebands which are only a separated by a few kilohertz. The obvious next step would be to reduce the intensity of the narrow linewidth laser to avoid saturation and measure a spectrum to determine the Doppler cooling temperature of an ion. Resolved sideband cooling the axial and cyclotron modes for a single ion should be relatively simple after this point. The transition can be broadened to enhance the cooling rate by coupling the $D_{5/2}$ and $P_{3/2}$ levels. The minimum temperature that can be reached now depends on at least two factors:

1. Off resonant sideband exciation i.e. stimulating the carrier when sideband cooling.
2. The ratio of the Lamb-Dicke factor for absorption and spontaneous decay when the narrow linewidth transition is artificially broadened.

For example, the minimum obtainable occupation number in a trap with a 200 kHz (30 kHz) motional frequency and a 20 kHz cooling bandwidth is approximately 0.01 (0.4). While resolved sideband cooling the magnetron mode is obviously possible, the low motional frequency may suggest that Doppler cooling via the 729 nm transition is preferable [90]. Perhaps a more efficient method of cooling the magnetron mode would be to couple it to the axial mode [91] or the modified cyclotron mode [92], although care would have to be taken not to add noise to the electrodes and heat the ions. Ground state cooling or at least near ground state cooling in a Penning trap has never been achieved before.

When there is more than one ion in the trap the radial motional frequencies can vary, even if the trap bias is kept constant, and hence the sideband spacing would not be fixed. To measure sidebands from more than one ion will require significant alteration to the apparatus. In particular, by separating the ring electrode into 6 or 8 segments to impose an asymmetric radial potential on any trapped particles. This would fix the Coulomb crystal rotation frequency to a variable RF drive.

We can also cool many ions into a Coulomb crystal. Then, by careful control of the trap potentials, the shape of the crystal can be manipulated. The two extreme shapes: linear chains and two dimensional discs are clearly observed. By comparison to computer simulations we have learnt much about these structures.

Previously, the longest linear ion chain that had been imaged in a Penning trap only consisted of two particles [9]. This number has been increased in this work to 29, producing a string which measures around 0.5 mm in length. It is obvious now, as suspected in reference [78], that the absence of laser cooling parallel to the magnetic field was the limiting factor in that experiment. It is likely that the ion chain could be extended by 2–5 times this length with the current trap configuration. The new limit would depend on the overlap between the radial laser cooling beam and the ions at the extrema of the chain. This could be improved by simply moving the focal position of the beam laterally away from the centre of the trap.

Coulomb crystals that extend into both two and three dimensions can be formed without any micromotion. This is one of the key benefits to using a Penning trap. I have shown a series of side-on images for a crystal made of 15 ions. By comparison to simple computer simulations, it is possible to deduce the rotation frequency. It may also be possible to find the rotation frequency via correlation of the photon arrival times at the detector [93]. However, this would be difficult to detect because the radial extent of the crystals is small and they are rotationally symmetric. Hence, we expect the modulation of fluorescence to be extremely weak.

Ground state cooling has only ever been performed on a single ion or a one dimensional string of ions previously. If the radial trap frequency was stabilised using the rotating wall technique we could use the narrow linewidth laser to do the first ground state cooling of the centre of mass mode of a two or three dimensional crystal. From this state, there are many possible experiments that have been proposed which require coupling many quantum particles together, for example see reference [94] and the references therein.

In our trap, we can also form larger crystals. Figure 5.8 shows an image of around 174 ions. This is the interesting intermediate regime where the shape can be determined from neither simple symmetry arguments nor Bravais lattice structures where edge effects do not have to be taken into account.

Although this thesis has concentrated on single ions and small to intermediate sized Coulomb crystals it is clear that, one of the key benefits to using a Penning trap is their stability over large volumes in the absence of micromotion. The trap volume is only set by the homogeneity of the magnetic field and size of the electrodes; no large RF voltages are required. The group headed by John Bollinger at NIST has long taken advantage of this and recently performed quantum simulation experiments with hundreds of ions [6], far more that currently being considered with RF traps.

One improvement which could easily be made to the current apparatus, would be to increase the confining magnetic field. The magnet that we use can potentially provide a field of around 2.4–2.5 T. If this change was implemented the cyclotron frequency would increase from 705 kHz to roughly 930 kHz. This would lead to lower initial Doppler cooling occupation numbers for the axial and cyclotron modes. However, this gain pales in comparison to the increase in the motional frequency that could be obtained by using a lower mass atomic species such as beryllium which would oscillate at 4.5 times higher frequency in the same magnitude magnetic field. The laser cooling frequencies for beryllium are different from those used to cool calcium and would have previously required the use of dye lasers. However, laser technology has improved significantly in the recent years and reference [88] reports a 750 mW all solid state laser system that produces narrowband 313 nm light for cooling beryllium ions.

One slightly more involved but very useful improvement would be to implement an optical system which could image the radial plane. Combining this with a high speed imager, such as a position sensitive photomultiplier, a great deal more information about the motion of a crystal could be obtained. Then, if motional spectroscopy was performed on a two dimensional disc of many ions in parallel, data about which particles had been excited could be obtained rather than just the fraction of ions that had been excited. This information could be used to determine the laser beam profile or in the longer term to create mesoscopic Schrödinger cat states [95].

Appendix A

Clebsch-Gordon Coefficients

Using the the notation $|1\rangle = |jm\rangle$, $|2\rangle = |j'm'\rangle$. With the standard form for the coefficients as in [25].

$$\begin{aligned} \langle j_1 j_2 m_1 m_2 | j_1 j_2 j m\rangle &= \langle j' k m' q | j' k j m\rangle \\ &= (-1)^{j_1+j_2-j} \langle j_2 j_1 m_1 m_2 | j_2 j_1 j m\rangle \end{aligned} \tag{A.1}$$

where k is the order of the transition, $k = 1$ for dipole transitions and $k = 2$ for quadrupole transitions and q denotes the change in magnetic quantum number as denoted in table 3.1.

Transition	m	m'	CG coefficient	$\frac{1}{\sqrt{2j+1}}$
$S_{\frac{1}{2}} \rightarrow P_{\frac{1}{2}}$ 397nm	$-\frac{1}{2}$	$-\frac{1}{2}$	$-\sqrt{\frac{1}{3}}$	$\sqrt{\frac{1}{2}}$
	$-\frac{1}{2}$	$\frac{1}{2}$	$\sqrt{\frac{2}{3}}$	
	$\frac{1}{2}$	$-\frac{1}{2}$	$\sqrt{\frac{2}{3}}$	
	$\frac{1}{2}$	$\frac{1}{2}$	$-\sqrt{\frac{1}{3}}$	
$S_{\frac{1}{2}} \rightarrow P_{\frac{3}{2}}$ 393nm	$-\frac{1}{2}$	$-\frac{3}{2}$	$\sqrt{\frac{1}{2}}$	$\sqrt{\frac{1}{2}}$
	$-\frac{1}{2}$	$-\frac{1}{2}$	$-\sqrt{\frac{1}{3}}$	
	$-\frac{1}{2}$	$\frac{1}{2}$	$\sqrt{\frac{1}{6}}$	

Transition	m	m'	CG coefficient	$\frac{1}{\sqrt{2j+1}}$
	$\frac{1}{2}$	$-\frac{1}{2}$	$\sqrt{\frac{1}{6}}$	
	$\frac{1}{2}$	$\frac{1}{2}$	$-\sqrt{\frac{1}{3}}$	
	$\frac{1}{2}$	$\frac{3}{2}$	$\sqrt{\frac{1}{2}}$	
$P_{\frac{3}{2}} \rightarrow S_{\frac{1}{2}}$ 393nm	$-\frac{3}{2}$	$-\frac{1}{2}$	1	$\frac{1}{2}$
	$-\frac{1}{2}$	$-\frac{1}{2}$	$\sqrt{\frac{2}{3}}$	
	$-\frac{1}{2}$	$\frac{1}{2}$	$\sqrt{\frac{1}{3}}$	
	$\frac{1}{2}$	$-\frac{1}{2}$	$\sqrt{\frac{1}{3}}$	
	$\frac{1}{2}$	$\frac{1}{2}$	$\sqrt{\frac{2}{3}}$	
	$\frac{1}{2}$	$\frac{3}{2}$	1	
$P_{\frac{1}{2}} \rightarrow D_{\frac{3}{2}}$ 866nm	$-\frac{1}{2}$	$-\frac{3}{2}$	$\sqrt{\frac{1}{2}}$	$\sqrt{\frac{1}{2}}$
	$-\frac{1}{2}$	$-\frac{1}{2}$	$-\sqrt{\frac{1}{3}}$	
	$-\frac{1}{2}$	$\frac{1}{2}$	$\sqrt{\frac{1}{6}}$	
	$\frac{1}{2}$	$-\frac{1}{2}$	$\sqrt{\frac{1}{6}}$	
	$\frac{1}{2}$	$\frac{1}{2}$	$-\sqrt{\frac{1}{3}}$	
	$\frac{1}{2}$	$\frac{3}{2}$	$\sqrt{\frac{1}{2}}$	
$D_{\frac{3}{2}} \rightarrow P_{\frac{1}{2}}$ 866nm	$-\frac{3}{2}$	$-\frac{1}{2}$	1	$\frac{1}{2}$
	$-\frac{1}{2}$	$-\frac{1}{2}$	$\sqrt{\frac{2}{3}}$	
	$-\frac{1}{2}$	$\frac{1}{2}$	$\sqrt{\frac{1}{3}}$	
	$\frac{1}{2}$	$-\frac{1}{2}$	$\sqrt{\frac{1}{3}}$	
	$\frac{1}{2}$	$\frac{1}{2}$	$\sqrt{\frac{2}{3}}$	
	$\frac{1}{2}$	$\frac{3}{2}$	1	

Transition	m	m'	CG coefficient	$\frac{1}{\sqrt{2j+1}}$
$\mathrm{D}_{\frac{3}{2}} \rightarrow \mathrm{P}_{\frac{3}{2}}$ 850nm	$-\frac{3}{2}$	$-\frac{3}{2}$	$-\sqrt{\frac{3}{5}}$	$\frac{1}{2}$
	$-\frac{3}{2}$	$-\frac{1}{2}$	$\sqrt{\frac{2}{5}}$	
	$-\frac{1}{2}$	$-\frac{3}{2}$	$-\sqrt{\frac{2}{5}}$	
	$-\frac{1}{2}$	$-\frac{1}{2}$	$-\sqrt{\frac{1}{15}}$	
	$-\frac{1}{2}$	$\frac{1}{2}$	$\sqrt{\frac{8}{15}}$	
	$\frac{1}{2}$	$-\frac{1}{2}$	$-\sqrt{\frac{8}{15}}$	
	$\frac{1}{2}$	$\frac{1}{2}$	$\sqrt{\frac{1}{15}}$	
	$\frac{1}{2}$	$\frac{3}{2}$	$\sqrt{\frac{2}{5}}$	
	$\frac{3}{2}$	$\frac{1}{2}$	$-\sqrt{\frac{2}{5}}$	
	$\frac{3}{2}$	$\frac{3}{2}$	$\sqrt{\frac{3}{5}}$	
$\mathrm{D}_{\frac{5}{2}} \rightarrow \mathrm{P}_{\frac{3}{2}}$ 854nm	$-\frac{5}{2}$	$-\frac{3}{2}$	1	$\sqrt{\frac{1}{6}}$
	$-\frac{3}{2}$	$-\frac{3}{2}$	$\sqrt{\frac{2}{5}}$	
	$-\frac{3}{2}$	$-\frac{1}{2}$	$\sqrt{\frac{3}{5}}$	
	$-\frac{1}{2}$	$-\frac{3}{2}$	$\sqrt{\frac{1}{10}}$	
	$-\frac{1}{2}$	$-\frac{1}{2}$	$\sqrt{\frac{3}{5}}$	
	$-\frac{1}{2}$	$\frac{1}{2}$	$\sqrt{\frac{3}{10}}$	
	$\frac{1}{2}$	$-\frac{1}{2}$	$\sqrt{\frac{3}{10}}$	
	$\frac{1}{2}$	$\frac{1}{2}$	$\sqrt{\frac{3}{5}}$	
	$\frac{1}{2}$	$\frac{3}{2}$	$\sqrt{\frac{1}{10}}$	
	$\frac{3}{2}$	$\frac{1}{2}$	$\sqrt{\frac{3}{5}}$	
	$\frac{3}{2}$	$\frac{3}{2}$	$\sqrt{\frac{2}{5}}$	
	$\frac{5}{2}$	$\frac{3}{2}$	1	

Transition	m	m'	CG coefficient	$\frac{1}{\sqrt{2j+1}}$
$\mathrm{P}_{\frac{3}{2}} \rightarrow \mathrm{D}_{\frac{5}{2}}$ 854nm	$-\frac{3}{2}$	$-\frac{5}{2}$	$\sqrt{\frac{2}{3}}$	$\sqrt{\frac{1}{6}}$
	$-\frac{3}{2}$	$-\frac{3}{2}$	$-\sqrt{\frac{4}{15}}$	
	$-\frac{3}{2}$	$-\frac{1}{2}$	$\sqrt{\frac{1}{15}}$	
	$-\frac{1}{2}$	$-\frac{3}{2}$	$\sqrt{\frac{2}{5}}$	
	$-\frac{1}{2}$	$-\frac{1}{2}$	$-\sqrt{\frac{2}{5}}$	
	$-\frac{1}{2}$	$\frac{1}{2}$	$\sqrt{\frac{1}{5}}$	
	$\frac{1}{2}$	$-\frac{1}{2}$	$\sqrt{\frac{1}{5}}$	
	$\frac{1}{2}$	$\frac{1}{2}$	$-\sqrt{\frac{2}{5}}$	
	$\frac{1}{2}$	$\frac{3}{2}$	$\sqrt{\frac{2}{5}}$	
	$\frac{3}{2}$	$\frac{1}{2}$	$\sqrt{\frac{1}{15}}$	
	$\frac{3}{2}$	$\frac{3}{2}$	$-\sqrt{\frac{4}{15}}$	
	$\frac{3}{2}$	$\frac{5}{2}$	$\sqrt{\frac{2}{3}}$	
$\mathrm{S}_{\frac{1}{2}} \rightarrow \mathrm{D}_{\frac{5}{2}}$ 729nm	$-\frac{1}{2}$	$-\frac{5}{2}$	$\sqrt{\frac{1}{3}}$	$\sqrt{\frac{1}{2}}$
	$-\frac{1}{2}$	$-\frac{3}{2}$	$-\sqrt{\frac{4}{5}}$	
	$-\frac{1}{2}$	$-\frac{1}{2}$	$\sqrt{\frac{1}{5}}$	
	$-\frac{1}{2}$	$\frac{1}{2}$	$-\sqrt{\frac{2}{15}}$	
	$-\frac{1}{2}$	$\frac{3}{2}$	$\sqrt{\frac{1}{15}}$	
	$\frac{1}{2}$	$-\frac{3}{2}$	$\sqrt{\frac{1}{15}}$	
	$\frac{1}{2}$	$-\frac{1}{2}$	$-\sqrt{\frac{2}{15}}$	
	$\frac{1}{2}$	$\frac{1}{2}$	$\sqrt{\frac{1}{5}}$	
	$\frac{1}{2}$	$\frac{3}{2}$	$-\sqrt{\frac{4}{15}}$	
	$\frac{1}{2}$	$\frac{5}{2}$	$\sqrt{\frac{1}{3}}$	

Appendix **B**

Polarisation Coefficients

As the polarisation of the light used to stimulate transitions between internal states is altered the Rabi frequency between the two levels varies. This chapter quantifies the change that occurs at different polarisations. The co-ordinates are defined in figure 3.1. Below I list the functions $|f^{(q)}(\alpha,\beta,\gamma)|$, $-1 \leq q \leq 1$ for dipole transitions and $|g^{(q)}(\alpha,\beta,\gamma)|$, $-2 \leq q \leq 2$ for quadrupole transitions (see also section 3.1.3). The problem with displaying these functions is that they contain 3 independent variables. To show the most useful cases I have taken specific values of α and used a 2D contour plot to show the probability of exciting to the upper level, i.e. Rabi frequency squared, $\left|f^{(q)}(\beta,\gamma)\right|^2$ and $\left|g^{(q)}(\beta,\gamma)\right|^2$ as a function of β and γ.

For σ and δ transitions only plots for positive changes in magnetic quantum number are shown, i.e. $q = -1, -2$. For negative changes in magnetic quantum number these graphs can be reflected along the line $\gamma = 180°$.

These square plots are meant to describe the surface of sphere so they show some slightly peculiar behaviour which is noted below.

- When $\beta = 0$ or $\beta = 90$ the polarisation vector points to the poles of the Poincaré sphere where γ has no impact on the polarisation of the field.
- As the laser beam propagates along the z-axis, there is no way for the polarisation to be parallel to the quantisation axis and all linear polarisations are equivalent.
- Common polarisations that show a maximum are explained below:
    - $\begin{pmatrix}\beta\\\gamma\end{pmatrix} = \begin{pmatrix}0°\\\text{all}\end{pmatrix} = $ linear polarisation $\parallel \boldsymbol{B}$

- ○ $\begin{pmatrix}\beta\\\gamma\end{pmatrix} = \begin{pmatrix}90^\circ\\\text{all}\end{pmatrix} = \text{ linear polarisation } \perp \boldsymbol{B}$
- ○ $\begin{pmatrix}\beta\\\gamma\end{pmatrix} = \begin{pmatrix}45^\circ\\90^\circ\end{pmatrix} = \text{ righthand circular polarisation along } \boldsymbol{k}$
- ○ $\begin{pmatrix}\beta\\\gamma\end{pmatrix} = \begin{pmatrix}45^\circ\\270^\circ\end{pmatrix} = \text{ lefthand circular polarisation along } \boldsymbol{k}$

B.1 Dipole transitions

B.1.1 $q = 0$

$$\left|c_i^{(0)}\boldsymbol{\epsilon}_i\right| = \left[\sin(\alpha)\cos(\beta)\right]^{\frac{1}{2}} \tag{B.1}$$

The π transitions have no dependence γ so the function can be shown on one plot, figure B.1.

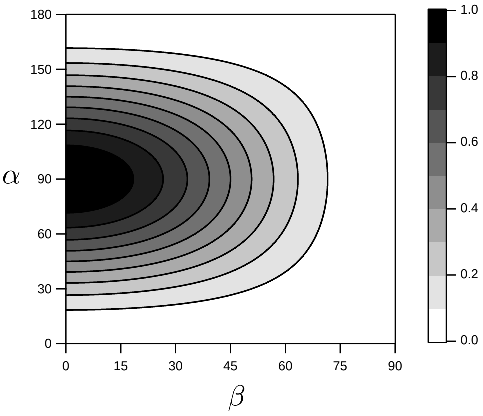

Figure B.1: Plot showing the probability of stimulating a π transition. Angle between the laser beam and quantisation axis, α, on the y-axis and angle between laser polarisation and quantisation axis, β, on the x-axis.

Here it is clear that there is only a reduction in 10% in the probability of stimulating a transition for up to ±15° differences in both laser angle α and polarisation angle β from the optimal.

B.1.2 $q = -1$

$$\left|c_i^{(-1)}\boldsymbol{\epsilon}_i\right| = \frac{1}{\sqrt{2}}\left[\cos^2(\alpha)\cos^2(\beta) + \sin^2(\beta) - \cos(\alpha)\sin(\beta)\sin(\gamma)\right]^{\frac{1}{2}} \tag{B.2}$$

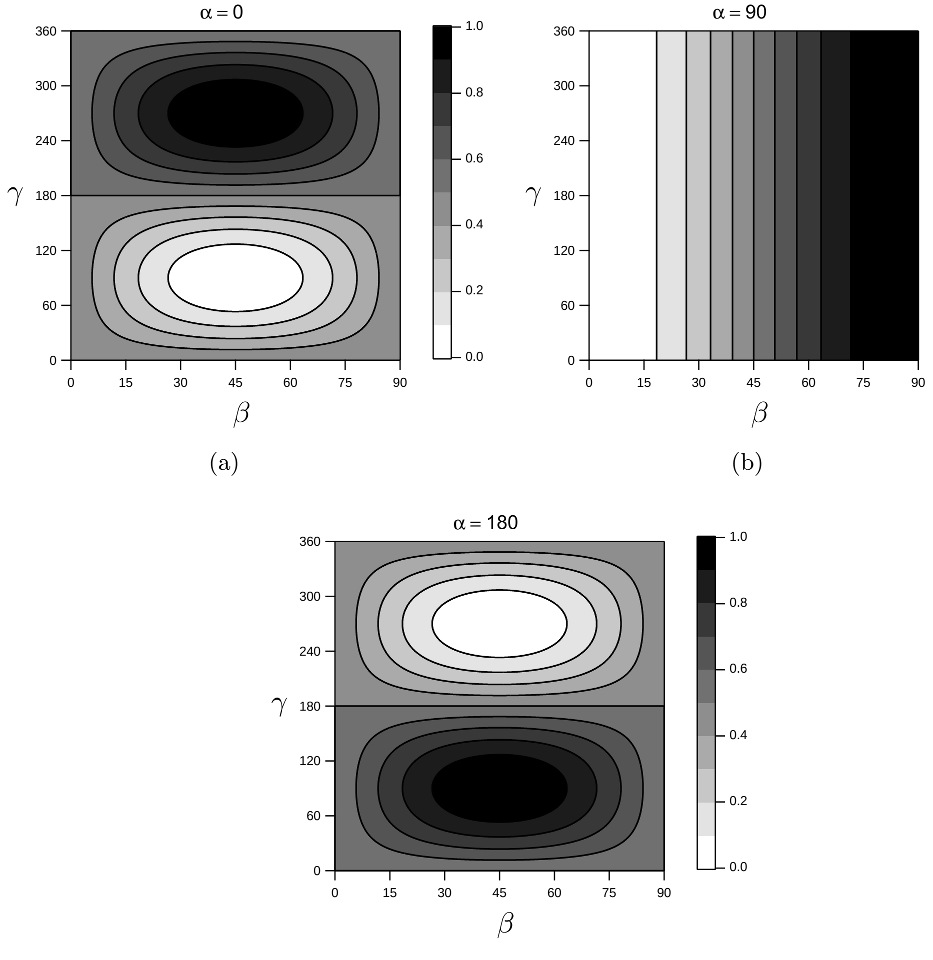

(a) (b)

(c)

Figure B.2: Contour plots showing the probability of stimulating an electric dipole σ^+ transition to a different state. Angle between polarisation and quantisation axis, β, on the x-axis and ellipticity, γ, on the y-axis. The titles of the individual plots give the angle between the laser beam and quantisation axis.

Figure B.2 shows that it is possible to be twice as efficient at stimulating a transition by co-propagating or counter-propagating the laser beam with the quantisation axis, compared to when the laser beam is incident perpendicular to the magnetic field ($\boldsymbol{k} \perp \mathbf{B}$). There is a wide range of polarisations around circular which are good at stimulating the transition for co- and counter-propagating beams. When linear polarisation is used perpendicular to the magnetic field γ can only vary by ±15° to maintain high efficiency at stimulating the transition.

B.1.3 $q = 1$

$$\left|c_i^{(1)}\boldsymbol{\epsilon}_i\right| = \frac{1}{\sqrt{2}}\left[\cos^2(\alpha)\cos^2(\beta) + \sin^2(\beta) + \cos(\alpha)\sin(\beta)\sin(\gamma)\right]^{\frac{1}{2}} \tag{B.3}$$

B.2 Quadrupole transitions

B.2.1 $q = 0$

$$\left|c_i^{(-1)}\boldsymbol{\epsilon}_i\boldsymbol{n}_j\right| = \frac{1}{2}\left[\sin^2(2\alpha)\cos^2(\beta)\right]^{\frac{1}{2}} \tag{B.4}$$

The quadrupole π transition requires linear polarisation parallel to the magnetic field no matter what angle the light is incident. This is in common with the dipole π transitions. Figure B.3 shows that the only way of stimulating quadrupole π transitions is by propagating the laser beam at roughly 45° to the quantisation axis. The tolerance on the laser for quadrupole π transitions is much narrower rather than dipole π transitions, only a range of ±5° still gives high Rabi frequencies.

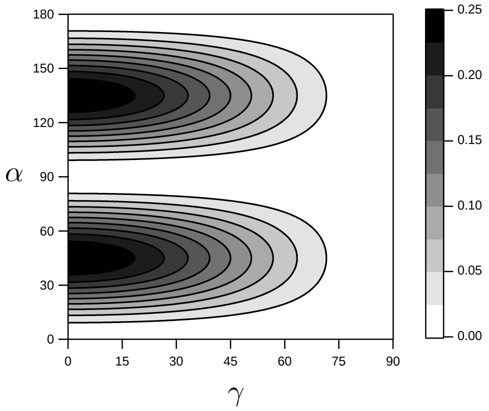

Figure B.3: Plot showing the probability of stimulating a π transition. Angle between the laser beam and quantisation axis, α, on the y-axis and angle between laser polarisation and quantisation axis, β, on the x-axis.

B.2.2 $q = -1$

$$\left|c_i^{(-1)}\boldsymbol{\epsilon}_i\boldsymbol{n}_j\right| = \frac{1}{\sqrt{6}}\Big[\cos^2(\beta)\cos^2(2\alpha) + \sin^2(\beta)\cos^2(\alpha) - \sin(\gamma)\sin(\beta)\cos(2\alpha)\cos(\alpha)\Big]^{\frac{1}{2}} \tag{B.5}$$

The polarisation required to stimulate quadrupole σ transitions changes rapidly with laser angle so it is more important that this is set correctly.

Figure B.4 shows that along the axis circular polarisation is required. When $\alpha = 45°$ the

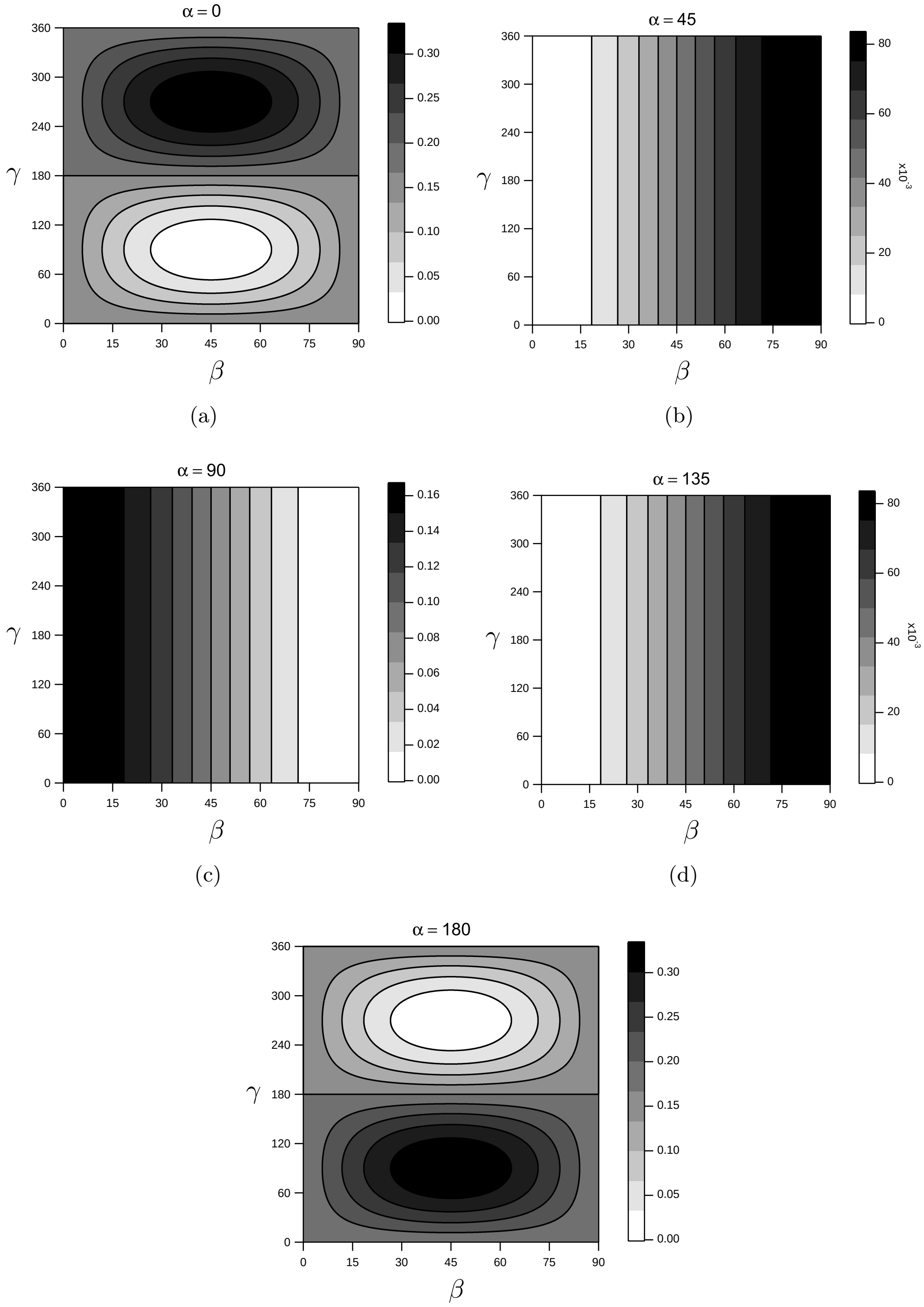

(a)

(b)

(c)

(d)

(e)

Figure B.4: Contour plots showing the probability of stimulating an electric quadrupole σ^+ transition to a different state. The angle between polarisation and quantisation axis, β, is displayed on the x-axis and ellipticity, γ, on the y-axis. The titles of the individual plots give the angle between the laser angle and quantisation axis.

polarisation required is linear perpendicular to z-axis and rotates through circular to linear polarisation parallel to the magnetic field when $\alpha = 90°$.

B.2.3 $q = 1$

$$\begin{aligned}\left|c_i^{(-1)}\boldsymbol{\epsilon}_i\boldsymbol{n}_j\right| =& \frac{1}{\sqrt{6}}\Big[\cos^2(\beta)\cos^2(2\alpha) + \sin^2(\beta)\cos^2(\alpha) \\ &+ \sin(\gamma)\sin(\beta)\cos(2\alpha)\cos(\alpha)\Big]^{\frac{1}{2}}\end{aligned} \tag{B.6}$$

B.2.4 $q = -2$

$$\begin{aligned}\left|c_i^{(-2)}\boldsymbol{\epsilon}_i\boldsymbol{n}_j\right| =& \frac{1}{\sqrt{6}}\sin(\alpha)\Big[\cos^2(\alpha)\cos^2(\beta) + \sin^2(\beta) \\ &+ \cos(\alpha)\sin(2\beta)\sin(\gamma)\Big]^{\frac{1}{2}}\end{aligned} \tag{B.7}$$

The δ transitions have no equivalent among the dipole transitions since they induce a change in magnetic quantum number by 2.

Figure B.5 shows the Rabi frequency that can be stimulated is maximum when the light is incident perpendicular to the magnetic field although changing α by 45° has only a small effect on the maximum Rabi frequency.

B.2.5 $q = 2$

$$\begin{aligned}\left|c_i^{(2)}\boldsymbol{\epsilon}_i\boldsymbol{n}_j\right| =& \frac{1}{\sqrt{6}}\sin(\alpha)\Big[\cos^2(\alpha)\cos^2(\beta) + \sin^2(\beta) \\ &- \cos(\alpha)\sin(2\beta)\sin(\gamma)\Big]^{\frac{1}{2}}\end{aligned} \tag{B.8}$$

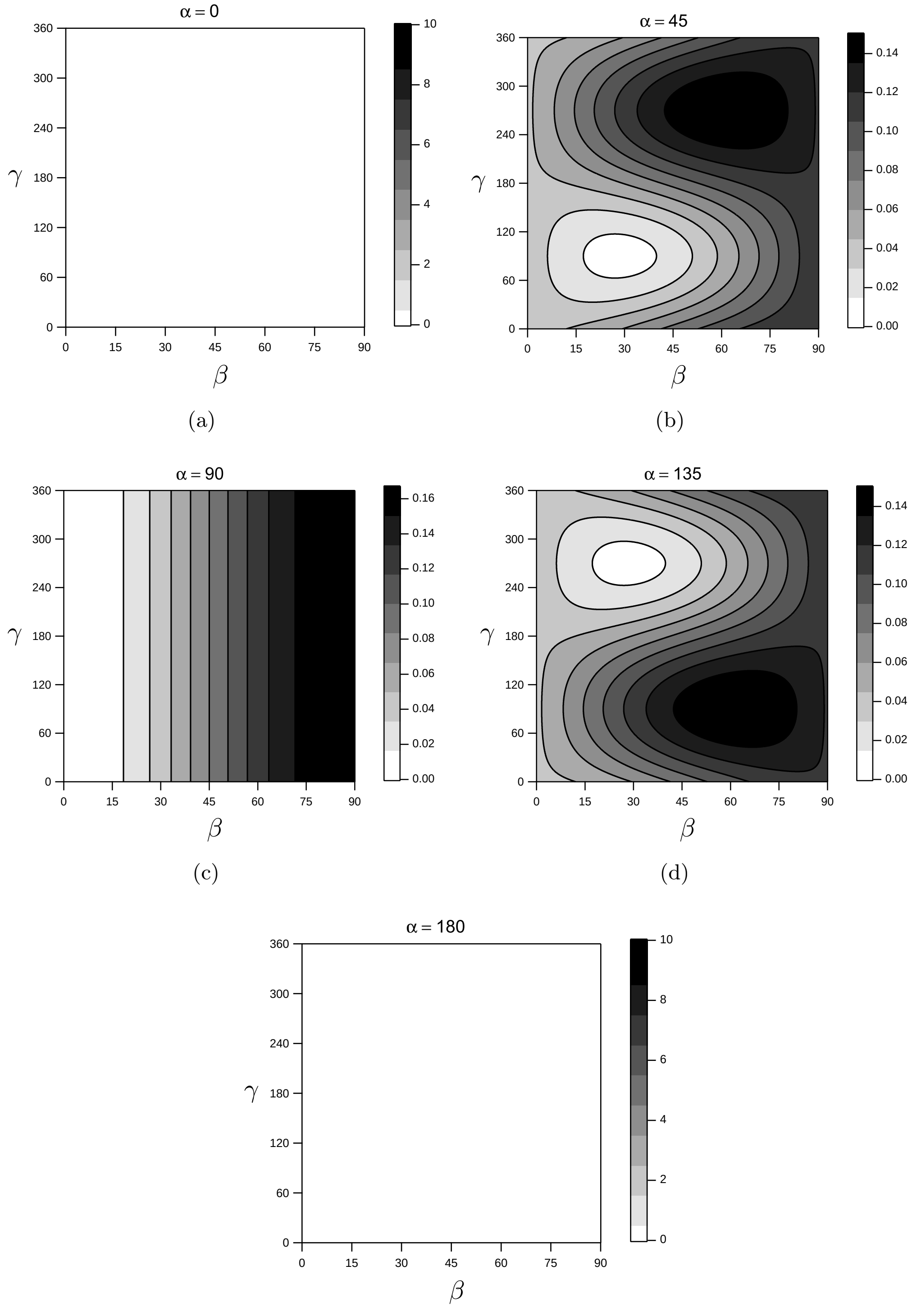

(a)

(b)

(c)

(d)

(e)

Figure B.5: Contour plots showing the probability of stimulating a δ^+ transition. The angle between polarisation and quantisation axis, β, is displayed on the x-axis and ellipticity, γ, on the y-axis. The titles of the individual plots give the angle between the laser angle and quantisation axis. It is not possible to stimulate delta transitions by using a laser beam parallel to the quantisation axis, hence the first and last plots all show zero.

Bibliography

[1] J. I. Cirac and P. Zoller, "Quantum Computations with Cold Trapped Ions," *Phys. Rev. Lett.*, vol. 74, pp. 4091–4094, May 1995.

[2] T. Monz, P. Schindler, J. T. Barreiro, M. Chwalla, D. Nigg, W. A. Coish, M. Harlander, W. Hänsel, M. Hennrich, and R. Blatt, "14-Qubit Entanglement: Creation and Coherence," *Phys. Rev. Lett.*, vol. 106, p. 130506, Mar 2011.

[3] T. Monz, K. Kim, W. Hänsel, M. Riebe, A. S. Villar, P. Schindler, M. Chwalla, M. Hennrich, and R. Blatt, "Realization of the Quantum Toffoli Gate with Trapped Ions," *Phys. Rev. Lett.*, vol. 102, p. 040501, Jan 2009.

[4] D. DiVincenzo *et al.*, "The physical implementation of quantum computation," *arXiv preprint quant-ph/0002077*, 2000.

[5] R. Feynman, "Simulating physics with computers," *International Journal of Theoretical Physics*, vol. 21, pp. 467–488, 1982.

[6] J. W. Britton, B. C. Sawyer, A. C. Keith, C.-C. J. Wang, J. K. Freedricks, H. Uys, M. J. Biercuk, and J. J. Bollinger, "Engineered two-dimensional Ising interactions in a trapped-ion quantum simulator with hundreds of spins," *Nature*, vol. 484, pp. 489–492, April 2012.

[7] B. P. Lanyon, C. Hempel, D. Nigg, M. Müller, R. Gerritsma, F. Zähringer, P. Schindler, J. T. Barreiro, M. Rambach, G. Kirchmair, M. Hennrich, P. Zoller, R. Blatt, and C. F. Roos, "Universal Digital Quantum Simulation with Trapped Ions," *Science*, vol. 334, no. 6052, pp. 57–61, 2011.

[8] W. M. Itano, J. J. Bollinger, J. N. Tan, B. Jelenković, X.-P. Huang, and D. J. Wineland, "Bragg Diffraction from Crystallized Ion Plasmas," *Science*, vol. 279, no. 5351, pp. 686–689, 1998.

[9] D. R. Crick, H. Ohadi, I. Bhatti, R. C. Thompson, and D. M. Segal, "Two-ion Coulomb crystals of $^{40}\mathrm{Ca}^{+}$ in a Penning trap," *Opt. Express*, vol. 16, pp. 2351–2362, Feb 2008.

[10] W. Paul, "Electromagnetic traps for charged and neutral particles," *Rev. Mod. Phys.*, vol. 62, pp. 531–540, Jul 1990.

[11] P. K. Ghosh, *Ion Traps.* Oxford University Press, 1995.

[12] C. Gignoux and B. Silvestre-Brac, *Solved Problems in Lagrangian and Hamiltonian Mechanics.* Springer, 2009.

[13] J. Goldman and G. Gabrielse, "Optimized planar Penning traps for quantum-information studies," *Phys. Rev. A*, vol. 81, p. 052335, May 2010.

[14] L. S. Brown and G. Gabrielse, "Geonium theory: Physics of a single electron or ion in a Penning trap," *Rev. Mod. Phys.*, vol. 58, pp. 233–311, Jan 1986.

[15] W. M. Itano and D. J. Wineland, "Laser cooling of ions stored in harmonic and Penning traps," *Phys. Rev. A*, vol. 25, pp. 35–54, Jan 1982.

[16] F. Diedrich, J. C. Bergquist, W. M. Itano, and D. J. Wineland, "Laser Cooling to the Zero-Point Energy of Motion," *Phys. Rev. Lett.*, vol. 62, pp. 403–406, Jan 1989.

[17] C. Monroe, D. M. Meekhof, B. E. King, S. R. Jefferts, W. M. Itano, D. J. Wineland, and P. Gould, "Resolved-Sideband Raman Cooling of a Bound Atom to the 3D Zero-Point Energy," *Phys. Rev. Lett.*, vol. 75, pp. 4011–4014, Nov 1995.

[18] F. Schmidt-Kaler, H. Häffner, M. Riebe, S. Gulde, G. P. T. Lancaster, T. Deuschle, C. Becher, C. F. Roos, J. Eschner, and R. Blatt, "Realization of the Cirac-Zoller controlled-NOT quantum gate," *Nature*, vol. 422, pp. 408–411, March 2003.

[19] C. Ospelkaus, U. Warring, Y. Colombe, K. Brown, J. Amini, D. Leibfried, and D. Wineland, "Microwave quantum logic gates for trapped ions," *Nature*, vol. 476, pp. 181–184, 2011.

[20] M. Johanning, A. Braun, N. Timoney, V. Elman, W. Neuhauser, and C. Wunderlich, "Individual Addressing of Trapped Ions and Coupling of Motional and Spin States Using rf Radiation," *Phys. Rev. Lett.*, vol. 102, p. 073004, Feb 2009.

[21] M. Weissbluth, *Atoms and Molecules.* Academic Press, 1978.

[22] R. Loudon, *The Quantum Theory of Light.* Oxford Science Publications, Oxford University Press, third ed., 2000.

[23] G. K. Woodgate, *Elementary Atomic Structure.* Oxford Science Publications, Oxford University Press, second ed., 1986.

[24] D. James, "Quantum dynamics of cold trapped ions with application to quantum computation," *Applied Physics B: Lasers and Optics*, vol. 66, pp. 181–190, 1998.

[25] M. Weissbluth, *Atoms and Molecules*, p. 31. Academic Press Inc, student edition ed., 1981.

[26] J. D. Jackson, *Classical Electrodynamics.* Wiley, 1998.

[27] E. Condon and S. G.H., *The Theory of Atomic Spectra*, pp. 91–95. Cambridge University Press, 1970.

[28] C. Roos, T. Zeiger, H. Rohde, H. C. Nägerl, J. Eschner, D. Leibfried, F. Schmidt-Kaler, and R. Blatt, "Quantum State Engineering on an Optical Transition and Decoherence in a Paul Trap," *Phys. Rev. Lett.*, vol. 83, pp. 4713–4716, Dec 1999.

[29] D. Wineland, C. Monroe, W. Itano, B. King, D. Leibfried, D. Meekhof, C. Myatt, and C. Wood, "Experimental Primer on the Trapped Ion Quantum Computer," *Fortschritte der Physik*, vol. 46, no. 4-5, pp. 363–390, 1998.

[30] C. J. Foot, *Atomic Physics.* oxford master series in atomic, optical and laser physics, Oxford University Press, 2005.

[31] D. J. Wineland, R. E. Drullinger, and F. L. Walls, "Radiation-Pressure Cooling of Bound Resonant Absorbers," *Phys. Rev. Lett.*, vol. 40, pp. 1639–1642, Jun 1978.

[32] W. Neuhauser, M. Hohenstatt, P. Toschek, and H. Dehmelt, "Optical-Sideband Cooling of Visible Atom Cloud Confined in Parabolic Well," *Phys. Rev. Lett.*, vol. 41, pp. 233–236, Jul 1978.

[33] T. Hänsch and A. Schawlow, "Cooling of gases by laser radiation," *Optics Communications*, vol. 13, no. 1, pp. 68 – 69, 1975.

[34] C. F. Roos, D. Leibfried, A. Mundt, F. Schmidt-Kaler, J. Eschner, and R. Blatt, "Experimental Demonstration of Ground State Laser Cooling with Electromagnetically Induced Transparency," *Phys. Rev. Lett.*, vol. 85, pp. 5547–5550, Dec 2000.

[35] D. J. Wineland, W. M. Itano, J. C. Bergquist, and R. G. Hulet, "Laser-cooling limits and single-ion spectroscopy," *Phys. Rev. A*, vol. 36, pp. 2220–2232, Sep 1987.

[36] G. Morigi, J. I. Cirac, M. Lewenstein, and P. Zoller, "Ground-state laser cooling beyond the Lamb-Dicke limit," *EPL (Europhysics Letters)*, vol. 39, no. 1, p. 13, 1997.

[37] G. Poulsen, Y. Miroshnychenko, and M. Drewsen, "Ground state sideband cooling of an ion in a room temperature trap with a sub-Hertz heating rate," *ArXiv e-prints*, 2012.

[38] D. Leibfried, R. Blatt, C. Monroe, and D. Wineland, "Quantum dynamics of single trapped ions," *Rev. Mod. Phys.*, vol. 75, pp. 281–324, Mar 2003.

[39] I. Marzoli, J. I. Cirac, R. Blatt, and P. Zoller, "Laser cooling of trapped three-level ions: Designing two-level systems for sideband cooling," *Phys. Rev. A*, vol. 49, pp. 2771–2779, Apr 1994.

[40] P. A. Barton, C. J. S. Donald, D. M. Lucas, D. A. Stevens, A. M. Steane, and D. N. Stacey, "Measurement of the lifetime of the $3d^2D_{5/2}$ state in $^{40}\text{Ca}^+$," *Phys. Rev. A*, vol. 62, p. 032503, Aug 2000.

[41] S. Donnellan, *Towards Sideband Cooling of a Single $^{40}Ca^+$ Ion in a Penning Trap.* PhD thesis, Imperial College London, 2011.

[42] D. R. Crick, S. Donnellan, D. M. Segal, and R. C. Thompson, "Magnetically induced electron shelving in a trapped Ca^+ ion," *Phys. Rev. A*, vol. 81, p. 052503, May 2010.

[43] R. W. Fox, C. W. Oates, and L. W. Hollberg, "Stabilizing diode lasers to high-finesse cavities," in *Cavity-Enhanced Spectroscopies* (R. D. van Zee and J. P. Looney, eds.), vol. 40 of *Experimental Methods in the Physical Sciences*, pp. 1 – 46, Academic Press, 2003.

[44] E. D. Black, "An introduction to Pound–Drever–Hall laser frequency stabilization," *American Journal of Physics*, vol. 69, no. 1, pp. 79–87, 2001.

[45] E. Philips, *Controlled Dynamics of Laser-Cooled Ions in a Penning Trap.* PhD thesis, University of London, 2004.

[46] J. Goodwin, "Development of a Fast Scanning Cavity for Laser Frequency Stabilisation and Locking," Master's thesis, Imperial College London, 2010.

[47] S. Bharadia, *Towards Laser Spectroscopy of Highly Charged Ions: Dynamics of $^{40}Ca^+$ Ions in a Penning Trap.* PhD thesis, Imperial College London, 2011.

[48] S. Bharadia, M. Vogel, D. Segal, and R. Thompson, "Dynamics of laser-cooled Ca^+ ions in a Penning trap with a rotating wall," *Applied Physics B: Lasers and Optics*, vol. 107, pp. 1105–1115, 2012. 10.1007/s00340-012-4871-6.

[49] S. Patel, "FPGA Controlled Pulse Spectroscopy of $^{40}\text{Ca}^+$ Ions," Master's thesis, Imperial College London, 2012.

[50] S. Zeeman, "FPGA-based Laser control for spectroscopy measurements in Ion Traps," Master's thesis, Imperial College London, 2012.

[51] J. J. Bollinger and D. J. Wineland, "Strongly Coupled Nonneutral Ion Plasma," *Phys. Rev. Lett.*, vol. 53, pp. 348–351, Jul 1984.

[52] M. D. Jones and D. M. Ceperley, "Crystallization of the One-Component Plasma at Finite Temperature," *Phys. Rev. Lett.*, vol. 76, pp. 4572–4575, Jun 1996.

[53] G. S. Stringfellow, H. E. DeWitt, and W. L. Slattery, "Equation of state of the one-component plasma derived from precision Monte Carlo calculations," *Phys. Rev. A*, vol. 41, pp. 1105–1111, Jan 1990.

[54] R. T. Farouki and S. Hamaguchi, "Thermal energy of the crystalline one-component plasma from dynamical simulations," *Phys. Rev. E*, vol. 47, pp. 4330–4336, Jun 1993.

[55] D. H. E. Dubin, "First-order anharmonic correction to the free energy of a Coulomb crystal in periodic boundary conditions," *Phys. Rev. A*, vol. 42, pp. 4972–4982, Oct 1990.

[56] W. L. Slattery, G. D. Doolen, and H. E. DeWitt, "n dependence in the classical one-component plasma Monte Carlo calculations," *Phys. Rev. A*, vol. 26, pp. 2255–2258, Oct 1982.

[57] J. J. Bollinger, D. J. Heinzen, F. L. Moore, W. M. Itano, D. J. Wineland, and D. H. E. Dubin, "Electrostatic modes of ion-trap plasmas," *Phys. Rev. A*, vol. 48, pp. 525–545, Jul 1993.

[58] L. R. Brewer, J. D. Prestage, J. J. Bollinger, W. M. Itano, D. J. Larson, and D. J. Wineland, "Static properties of a non-neutral ^{9}be$^+$-ion plasma," *Phys. Rev. A*, vol. 38, pp. 859–873, Jul 1988.

[59] D. J. Heinzen, J. J. Bollinger, F. L. Moore, W. M. Itano, and D. J. Wineland, "Rotational equilibria and low-order modes of a non-neutral ion plasma," *Phys. Rev. Lett.*, vol. 66, pp. 2080–2083, Apr 1991.

[60] X.-P. Huang, J. J. Bollinger, T. B. Mitchell, and W. M. Itano, "Phase-Locked Rotation of Crystallized Non-neutral Plasmas by Rotating Electric Fields," *Phys. Rev. Lett.*, vol. 80, pp. 73–76, Jan 1998.

[61] T. Hasegawa, M. J. Jensen, and J. J. Bollinger, "Stability of a Penning trap with a quadrupole rotating electric field," *Phys. Rev. A*, vol. 71, p. 023406, Feb 2005.

[62] J. N. Tan, J. J. Bollinger, B. Jelenkovic, and D. J. Wineland, "Long-Range Order in Laser-Cooled, Atomic-Ion Wigner Crystals Observed by Bragg Scattering," *Phys. Rev. Lett.*, vol. 75, pp. 4198–4201, Dec 1995.

[63] J. H. Chu and L. I, "Direct observation of Coulomb crystals and liquids in strongly coupled rf dusty plasmas," *Phys. Rev. Lett.*, vol. 72, pp. 4009–4012, Jun 1994.

[64] H. Thomas, G. E. Morfill, V. Demmel, J. Goree, B. Feuerbacher, and D. Möhlmann, "Plasma Crystal: Coulomb Crystallization in a Dusty Plasma," *Phys. Rev. Lett.*, vol. 73, pp. 652–655, Aug 1994.

[65] P. K. Shukla, "A survey of dusty plasma physics," *Physics of Plasmas*, vol. 8, no. 5, pp. 1791–1803, 2001.

[66] G. R. Guthöhrlein, M. Keller, K. Hayasaka, W. Lange, and H. Walther, "A single ion as a nanascopic probe of an optical field," *Nature*, vol. 414, pp. 49–51, November 2001.

[67] A. Dantan, M. Albert, J. P. Marler, P. F. Herskind, and M. Drewsen, "Large ion Coulomb crystals: A near-ideal medium for coupling optical cavity modes to matter," *Phys. Rev. A*, vol. 80, p. 041802, October 2009.

[68] P. F. Herskind, A. Dantan, J. P. Marler, M. Albert, and M. Drewsen, "Realization of collective strong coupling with ion Coulomb crystals in an optical cavity," *Nature Physics*, vol. 5, pp. 494–498, June 2009.

[69] V. Giovannetti, S. Lloyd, and L. Maccone, "Quantum-Enhanced Measurements: Beating the Standard Quantum Limit," *Science*, vol. 306, no. 5700, pp. 1330–1336, 2004.

[70] B. C. Sawyer, J. W. Britton, A. C. Keith, C.-C. J. Wang, J. K. Freericks, H. Uys, M. J. Biercuk, and J. J. Bollinger, "Spectroscopy and Thermometry of Drumhead Modes in a Mesoscopic Trapped-Ion Crystal Using Entanglement," *Phys. Rev. Lett.*, vol. 108, p. 213003, May 2012.

[71] S. L. Gilbert, J. J. Bollinger, and D. J. Wineland, "Shell-Structure Phase of Magnetically Confined Strongly Coupled Plasmas," *Phys. Rev. Lett.*, vol. 60, pp. 2022–2025, May 1988.

[72] D. J. Wineland, J. C. Bergquist, W. M. Itano, J. J. Bollinger, and C. H. Manney, "Atomic-Ion Coulomb Clusters in an Ion Trap," *Phys. Rev. Lett.*, vol. 59, pp. 2935–2938, Dec 1987.

[73] R. Thompson and D. Wilson, "The motion of small numbers of ions in a Penning trap," *Zeitschrift für Physik D Atoms, Molecules and Clusters*, vol. 42, pp. 271–277, 1997.

[74] S. Fishman, G. De Chiara, T. Calarco, and G. Morigi, “Structural phase transitions in low-dimensional ion crystals,” *Phys. Rev. B*, vol. 77, p. 064111, Feb 2008.

[75] D. G. Enzer, M. M. Schauer, J. J. Gomez, M. S. Gulley, M. H. Holzscheiter, P. G. Kwiat, S. K. Lamoreaux, C. G. Peterson, V. D. Sandberg, D. Tupa, A. G. White, R. J. Hughes, and D. F. V. James, “Observation of Power-Law Scaling for Phase Transitions in Linear Trapped Ion Crystals,” *Phys. Rev. Lett.*, vol. 85, pp. 2466–2469, Sep 2000.

[76] R. Thompson. Personal Communication.

[77] “Protomol.” http://protomol.sourceforge.net/.

[78] D. Crick, *Manipulation of Laser Cooled Ca^+ Ions in Penning Traps.* PhD thesis, Imperial College, University of London, July 2009.

[79] H. S. Lakkaraju and H. A. Schuessler, “Motional side-band resonances in the microwave spectrum of stored ions,” *Journal of Applied Physics*, vol. 53, no. 6, pp. 3967–3974, 1982.

[80] J. C. Bergquist, W. M. Itano, and D. J. Wineland, “Recoilless optical absorption and doppler sidebands of a single trapped ion,” *Phys. Rev. A*, vol. 36, pp. 428–430, Jul 1987.

[81] S. E. Hamann, D. L. Haycock, G. Klose, P. H. Pax, I. H. Deutsch, and P. S. Jessen, “Resolved-Sideband Raman Cooling to the Ground State of an Optical Lattice,” *Phys. Rev. Lett.*, vol. 80, pp. 4149–4152, May 1998.

[82] A. Schliesser, R. Rivière, G. Anetsberger, O. Arcizet, and T. J. Kippenberg, “Resolved-sideband cooling of a micromechanical oscillator,” *Nature Physics*, vol. 4, pp. 415–419, April 2008.

[83] T. Rosenband, D. B. Hume, P. O. Schmidt, C. W. Chou, A. Brusch, L. Lorini, W. H. Oskay, R. E. Drullinger, T. M. Fortier, J. E. Stalnaker, S. A. Diddams, W. C. Swann, N. R. Newbury, W. M. Itano, D. J. Wineland, and J. C. Bergquist, “Frequency Ratio of Al^+ and Hg^+ Single-Ion Optical Clocks; Metrology at the 17th Decimal Place,” *Science*, vol. 319, no. 5871, pp. 1808–1812, 2008.

[84] D. M. Meekhof, C. Monroe, B. E. King, W. M. Itano, and D. J. Wineland, “Generation of Nonclassical Motional States of a Trapped Atom,” *Phys. Rev. Lett.*, vol. 76, pp. 1796–1799, Mar 1996.

[85] N. Kimura, K. Okada, T. Takayanagi, M. Wada, S. Ohtani, and H. A. Schuessler, “Sympathetic crystallization of CaH^+ produced by a laser-induced reaction,” *Phys. Rev. A*, vol. 83, p. 033422, Mar 2011.

[86] A. Burrell, *High Fidelity Readout of Trapped Ion Qubits.* PhD thesis, Oxford University, 2010.

[87] A. M. Eltony, S. X. Wang, G. M. Akselrod, P. F. Herskind, and I. L. Chuang, "Transparent ion trap with integrated photodetector," *ArXiv e-prints*, December 2012.

[88] A. Wilson, C. Ospelkaus, A. VanDevender, J. Mlynek, K. Brown, D. Leibfried, and D. Wineland, "A 750-mw, continuous-wave, solid-state laser source at 313 nm for cooling and manipulating trapped ^{9}be$^+$ ions," *Applied Physics B*, vol. 105, pp. 741–748, 2011.

[89] R. C. Thompson and J. Papadimitriou, "Simple model for the laser cooling of an ion in a Penning trap," *Journal of Physics B: Atomic, Molecular and Optical Physics*, vol. 33, no. 17, p. 3393, 2000.

[90] R. J. Hendricks, J. L. Sørensen, C. Champenois, M. Knoop, and M. Drewsen, "Doppler cooling of calcium ions using a dipole-forbidden transition," *Phys. Rev. A*, vol. 77, p. 021401, Feb 2008.

[91] E. A. Cornell, R. M. Weisskoff, K. R. Boyce, and D. E. Pritchard, "Mode coupling in a Penning trap: π pulses and a classical avoided crossing," *Phys. Rev. A*, vol. 41, pp. 312–315, Jan 1990.

[92] H. F. Powell, D. M. Segal, and R. C. Thompson, "Axialization of Laser Cooled Magnesium Ions in a Penning Trap," *Phys. Rev. Lett.*, vol. 89, p. 093003, Aug 2002.

[93] K. Dholakia, G. Horvath, D. Segal, and R. Thompson, "Photon Correlation Measurement of Ion Oscillation Frequencies in a Combined Trap," *Journal of Modern Optics*, vol. 39, no. 11, pp. 2179–2185, 1992.

[94] R. Blatt and D. Wineland, "Entangled states of trapped atomic ions," *Nature*, vol. 453, pp. 1008–1015, June 2008.

[95] C. A. Sackett, D. Kielpinski, B. E. King, C. Langer, V. Meyer, C. J. Myatt, M. Rowe, Q. A. Turchette, W. M. Itano, D. J. Wineland, and C. Monroe, "Experimental entanglement of four particles," *Nature*, vol. 404, pp. 256–259.